DEVELOPMENT AND APPLICATION OF AN INTEGRATED AERODYNAMIC AND THERMODYNAMIC TESTING SYSTEM FOR CARS

by

Abdalla Abdel-Rahman

A thesis submitted in Partial Fulfillment of the Requirements for the Degree of

Master of Applied Science
in
The Faculty of Engineering and Applied Science
Mechanical Engineering

University of Ontario Institute of Technology

June 2015

Abstract and Keywords

In this thesis an integrated aerodynamic and thermodynamic testing system was developed. It consists of an incremental force measuring system (FMS) that was designed and constructed. In addition, a testing protocol was developed to integrate aerodynamic and thermodynamic testing in the climatic wind tunnel at UOIT. The FMS was calibrated and used to improve the aerodynamics of four race cars. Furthermore, a thermodynamic test consisting of temperature measurements, and a flow visualization study using tufts were conducted. The aerodynamic study showed that a set of aerodynamic devices can significantly alter the drag force and downforce on cars. However, a little angularity of a device, such as the side front canards, to the flow direction, can significantly alter its function. The flow visualization test showed that the local flow direction strongly depends on the local geometry. The temperature study revealed that the underbody cooling was jeopardized by a rear underbody diffuser.

Keywords: aerodynamic, thermodynamic, temperature, automotive, car, vehicle, aero-thermal, integrated, wind tunnel, testing, experimental, upperbody, underbody, crosswind, yaw, diffuser, wing, air dam, front splitter, front extension, gurney flap, front canards, angle of attack, drag, downforce, side force, lateral force.

Acknowledgements

My family's support, understanding, and love was critical for this study's completion. I am also very fortunate to have friends that are nothing less than family. Nadim Arafa's intelligence in graph presentation served me purposefully in this thesis which I am deeply thankful for. I will not forget Emad Abdelrahman and Omar Zeitoun's enthusiasm and encouragement which gratefully motivated me to pursue my Master's degree.

I am forever indebted to my advisor and mentor Dr. Martin Agelin-Chaab for his endless guidance and support. His wisdom has provided me with insight that I will forever reflect upon.

The contribution by Mantis Racing (industry partner) and their contact persons (Ernie Jakubowski and Brion Charters) in this study is graciously acknowledged. The assistance and professionalism of ACE's executives and engineers, particularly John Komar, Gary Elfstrom, Randy Burnet, Warren Karlson, Anthony Van De Wetering, Kevin Carlucci, Andrew Norman, Gord Koehne, Victor Mazzuocco, Stephen Dawson and Mark Ironside was extremely appreciated and conducive in successfully executing this study. This study could not have been completed without the hard work and dedication of the summer research students, Jonas Fernandes, Iuri Frias Vieira, and Safayaat Ul Alam, whom I wish all the best and success in their future endeavors.

Nomenclature

A	Projected frontal area (m^2)
β	Slip angle (degrees)
C_D	Drag coefficient (dimensionless)
C_P	Pressure coefficient (dimensionless)
D_o	Outer diameter (m)
F_x	Drag force (N)
F_y	Lateral/side force (N)
F_z	Downforce (N)
h	Elevation (m)
p	Dynamic pressure (Pa)
ΔP_o	Total pressure at 0˚ yaw – total pressure (Pa)
p_T	Total pressure (Pa)
R^2	Coefficient of determination (dimensionless)
ρ	Density (kg/m^3)
u	Axial velocity through pipe (m/s)
V	Fluid velocity (m/s)
v	Velocity of free stream (m/s)
γ	Specific weight (N/m^3)

Abbreviations

ACE	Automotive Centre of Excellence
AWT	Aerodynamic Wind Tunnel
CFD	Computational Fluid Dynamics
CO_2	Carbon Dioxide
CWT	Climatic Wind Tunnel
DAQ	Data AcQuisition system
DC	Direct Current
DSLR	Digital Single-Lens Reflect
FMS	Force Measurement System
FSAE	Formula Society of Automotive Engineers
GF	Gurney Flap
GTS	Grand Touring Sport
HAWT	Hyundai's Aero-acoustic Wind Tunnel
NI	National Instruments
NIST	National Institute of Standards and Technology
PSP	Pressure Sensitive Paints
RH	Relative Humidity
SAE	Society of Automotive Engineers
UOIT	University of Ontario Institute of Technology
VG	Vortex Generator
WT	Wind Tunnel

Table of Contents

List of Tables

List of Figures

Chapter 1 : Introduction

1.1: Background

Whenever an object, such as a road vehicle, moves through air it experiences aerodynamic forces and moments. The three main aerodynamic forces are drag, lift, and side forces, and the three main aerodynamic moments are yawing, pitching and rolling moments as shown in Figure 1.1. In aerodynamics, forces are the main area of study as moments are produced by force differentials (Tropea et al., 2007).

The drag force resists the motion and causes a car to exert more power to achieve its desired performance (Barnard, 2009). The side or lateral force, which is usually the result of a turn or a crosswind, acts along the lateral axis (y-axis) of the car as shown in Figure 1.1. The lift force acts along the vertical axis (z-axis) of the car and tends to lift the car thus reducing the traction between the tires and the road. This may cause the tires of the car to slip resulting in a lack of stability and control. Therefore in cars, unlike in aerospace applications, positive lift is undesirable. It is negative lift or downforce that is preferred. Figure 1.2 depicts the relationship between the downforce (F_z), the lateral force (F_y), and the slip angle (β). The lateral force results when a car turns; the tighter the turn the greater the lateral force exerted. Figure 1.2 shows

that when downforce increases (from A to B), the slip angle caused by the tire, is reduced resulting in a more stable and tighter turn.

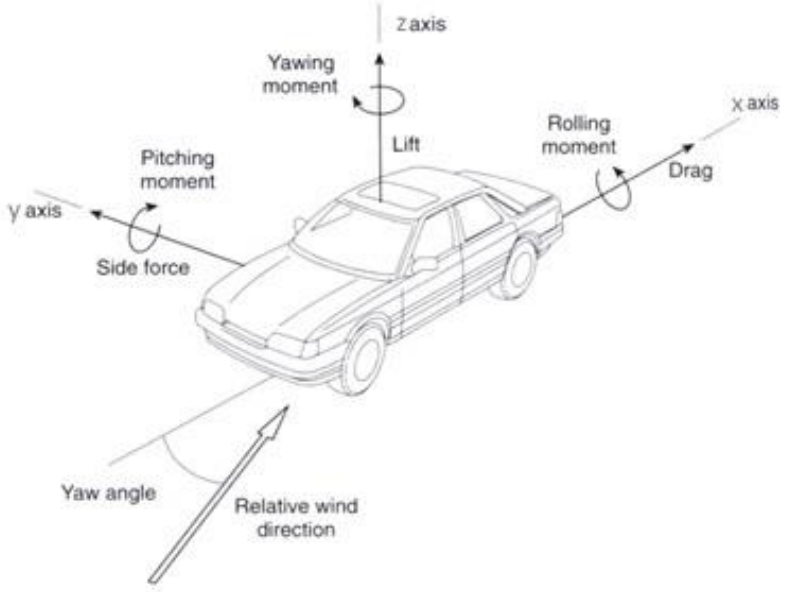

Figure 1.1: A schematic showing the aerodynamic forces and moments on a car (Barnard, 2009)

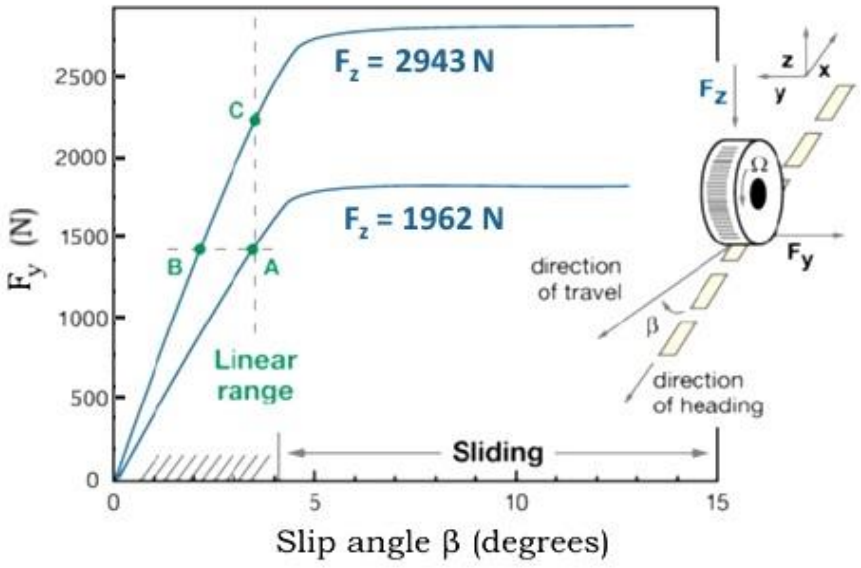

Figure 1.2: The effect of downforce (F_z) on the slip angle of a tire (Joseph Katz, 2006)

Improving a car aerodynamically implies modifying the aerodynamic forces to achieve various objectives such as improve cornering speed, stability, manoeuverability, and fuel efficiency. However the mutual relationships between the desirable and undesirable aerodynamic forces make this a challenging process. For example, downforce is a desirable force that also produces downforce-induced drag. Thus, a dimensionless parameter is used to quantify the drag of a car in air, called the drag coefficient (C_D). This coefficient relates the drag force to the fluid's parameters shown in the drag force equation below.

$$C_D = \frac{F_x}{\frac{1}{2}\rho v^2 A} \tag{1.1}$$

Where F_x is the drag force, ρ and v are the density and velocity of the air respectively, and A is the projected frontal area of the car. Consequently, a low drag coefficient indicates low aerodynamic drag.

Aerodynamic improvement is usually done by the use of aerodynamic devices on existing cars. Improvement can also be done in a wind tunnel or on a race track, however the latter is not efficient. Wind tunnels (WTs) are facilities which blow air through a test section and are used to simulate the motion of an object in air. In car aerodynamic testing, cars are properly positioned in a WT and secured, and air is blown around them at simulated road speeds. A beneficial feature WTs

strive to possess is a turntable floor to simulate crosswind, this allows any car to be studied at different yaw angles.

There are two general classes of car testing wind tunnels; aerodynamic wind tunnels (AWT) and climatic wind tunnels (CWT). The AWTs analyse the car's aerodynamic performance quantitatively and qualitatively to facilitate aerodynamic improvement. The CWTs, on the other hand, are used to evaluate the thermodynamic performance of a car in a variety of different climatic conditions under dynamic load (provided by a dynamometer). Successful thermodynamic performance is the ability for the car's engine and cooling system to perform satisfactorily in various climatic conditions. The challenge is to improve the car's aerodynamic performance without jeopardizing its thermodynamic performance. Traditionally, aero-thermo-dynamic improvement testing requires both an AWT and a CWT testing. So far there is no wind tunnel that can perform aerodynamic and thermodynamic testing on the same tunnel floor, to the best of the author's knowledge.

1.2: Motivation

As stated earlier, aerodynamic and thermodynamic performance improvement of cars are traditionally conducted separately in AWTs and CWTs. This is expensive and time consuming. There is therefore a growing need for integrated aerodynamic and thermodynamic

performance testing on cars. However, it is challenging to maximize aerodynamic performance without jeopardizing thermodynamic performance in the absence of an appropriate testing facility. This is particularly critical at conditions of aerodynamic yaw such as high speed cornering and crosswinds. Such appropriate testing facilities are uncommon.

Nonetheless, University of Ontario, Institute of Technology's (UOIT) CWT has a unique potential for such test capabilities, specifically to comprehensively study the influence of yaw on different aerodynamic and thermodynamic conditions. This is because of two important features of the CWT: a unique chassis dynamometer located in a turntable that can provide yaw and aerodynamic wind tunnel top-tier flow quality. In fact, UOIT's CWT is the world's only full-range CWT that incorporates a dynamometer in a large turntable for yaw testing. However, the facility neither has a balance system for measuring aerodynamic forces nor a test protocol for a combined aerodynamic and thermodynamic testing. This is desperately needed because there are industry partners in the racing business that are interested and have ready customers for the combined aerodynamic and thermodynamic testing capabilities. Consequently, this research was initiated by an industry partner, Mantis Racing, with financial support from the Natural Sciences and Engineering Research Council of Canada.

1.3: Objectives

There are three main objectives for this project. The first is to design and assemble a force measuring system (FMS) which is a floor-type balance system. The FMS should measure the incremental aerodynamic forces on cars. The second objective is to develop a testing protocol for the integrated aerodynamic and thermodynamic testing in the UOIT's CWT.

The third objective is to calibrate the FMS and use it to conduct aero-thermal tests. These tests consist of an aerodynamic improvement, flow visualization and thermodynamic testing. In addition, the effect of a number of aerodynamic devices on the aerodynamic forces will be measured and analyzed.

1.4: Thesis Structure

The thesis is organized into five chapters. The rest of the thesis is arranged as follows. In Chapter 2, the literature review of previous studies on flow visualization, temperature measurements, and the improvement of forces are reviewed. Chapter 3 details the design, fabrication and set up of the FMS, test facilities, calibration, integrated testing protocol, and measurement procedures. Chapter 4 reports the results and discussion of the experimental results. In addition, the thermodynamic evaluation of a car is also studied in Chapter 4. Finally,

the summary and conclusions of the thesis and recommendations for future work are presented in Chapter 5.

Chapter 2 : Literature Review

In this chapter wind tunnels are introduced and a literature survey on wind tunnel experiments on car aerodynamics and thermodynamics is conducted. Flow visualization and temperature measurements are also reviewed. In addition a review of aerodynamic force measurements and improvement procedures using floor balances are presented.

2.1: Wind Tunnels

In the field of automotive aerodynamics, wind tunnel testing is an effective method (Barnard, 2009; Hucho, 1993). This is because wind tunnel testing provide experimental reliable results where analytical techniques are so complex and computational fluid dynamics (CFD) methods are either approximated results or computationally prohibitive. Wind tunnels simulate road conditions with the help of a fan, a nozzle, a diffuser, and a test section. As mentioned previously wind tunnels can be broadly categorized into CWTs and AWTs. For the study of cars, CWTs can be used to assess a car's thermodynamic performance in different environmental conditions, while AWTs can be used to study a car's aerodynamic performance. However, combining both tests into one facility will save both time and money for customers. Hyundai's Aero-acoustic Wind Tunnel (HAWT) has been the closest to reach this objective but with a number of limitations (Kim et al., 2001). Although

HAWT permits aero-thermo-testing, the tests are not conducted on the same turntable floor which might produce unreliable results, changing the location of a car in a wind tunnel will change the airflow homogeneity, the operating pressure, and temperature of the car. In addition, the speed and temperature ranges of the HAWT do not allow for a comprehensive performance study on cars.

Integrating aerodynamic testing into a thermodynamic testing facility (CWT), requires a review of AWT. The most significant problem with AWTs is the boundary layer produced on the surface of a stationary wind tunnel floor. This boundary layer can cause a discrepancy in the force readings as it is not consistent with actual road conditions. A boundary layer does not exist in road driving situations as the air and the road are stationary while the car is the moving object, however on a stationary floor AWT, the air is moving while the car and the road is stationary. Therefore a number of approaches are used to better simulate road conditions. One approach is to equip the wind tunnel floor with boundary layer removal systems as shown in Figure 2.1.

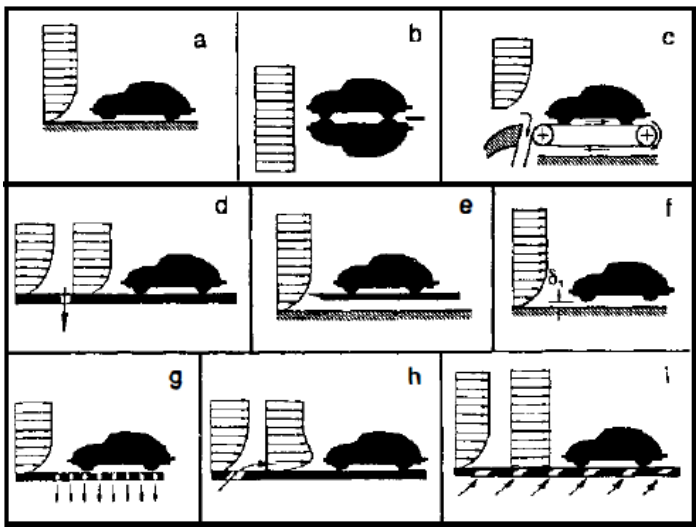

Figure 2.1: Various boundary layer removal mechanisms a) velocity profile without boundary layer removal mechanism b) symmetric model method c) moving floor with scoop system method d) frontal suction method e) elevated floor method f) elevated model method g) distributed suction method h) frontal tangential blowing method and i) distributed tangential blowing method (Hucho, 1993)

The above figure shows a number of different boundary layer removal systems, Figure 2.1a shows a typical velocity profile on a stationary floor AWT, while the remaining images show velocity profiles with boundary removal mechanisms in AWTs. A commonly used removal mechanism is the moving floor mechanism (Figure 2.1c), the moving floor mechanism is composed of a belt that rolls at the same speed as the air flow simulating road conditions. A scoop system is usually installed upstream of the belt to remove a reasonable air layer before flowing over the belt in attempt to diminish the boundary layer thickness. A frontal suction system (Figure 2.1d) sucks upwind

boundary air which helps in boundary layer removal. A distributed suction floor (Figure 2.1g) is a technique that draws in air through perforated holes in the floor, this helps to prevent or possibly eliminate the boundary layer. The tangential blowing technique (Figure 2.1h) blows air at a tangent to the floor which excites the boundary layer therefore diminishing boundary layer effects. The most effective method out of all the mechanisms is the moving floor method (Figure 2.1c) as it most imitates road conditions.

For car manufacturers it is important to have an effective boundary layer removal mechanism in their WT in order to obtain accurate absolute aerodynamic specifications. This is because they need the data for advertisement. However for the racing industry, incremental force measurements are enough for aerodynamic improvement so the emphasis is not on absolute values (Duell et al., 2010). When incremental force measurements are the main objective, repeatability of the measuring system becomes more desirable than accuracy.

2.2: Flow Visualization

Flow visualization is a technique used to visualize fluid flows since fluid particles are invisible. This technique is used to aid aerodynamic improvement of a car by determining flow separation points. Delaying flow separation will reduce the car's overall drag. Commonly used

techniques for flow visualization are chemical coating, smoke, and tufts with tufts being the most common technique (Rathakrishnan, 2007).

2.2.1: Tufts Technique

Tufts are the oldest tool used in visualizing the flow of a fluid on a surface, however their informative feedback is limited with respect to their laborious preparation (Hucho, 1998). The continued use of tufts for flow visualization is in light of their simplicity and cost effectiveness. Tufts are small lengths of yarn that can be attached to the body of the car during wind tunnel tests. The tufts are able to mimic the airflow pattern on the surface of the car.

The design of the front wing, rear wing, and diffuser of a 2012 Chalmers Formula SAE (FSAE) car was evaluated during pre-competition using flow visualization tufts (Rehnberg et al., 2013). Although CFD software was used extensively in the design, on-track flow tufts were utilized as an experimental reference. The tufts were attached to the underside of the front and rear wings with cameras fixated on them, to investigate flow separation. The results show that in straight line acceleration the tufts were kept to the surface affirming an attached flow. In low speed cornering however the tufts were flailing which confirm poor wing performance at low speeds.

Van de Wijdeven et al. (2013) studied the trailing vortex core behind vortex generators (VGs). The purpose of this experiment was to

identify the effect of the VGs in ground effect on the performance of a racing car and to improve it by increasing the resultant downforce produced. Firstly, the flow visualization in the wake of the VGs had to be studied using a 5 mm tuft. The tuft, which was attached to a 1 mm thick probe, would rotate rapidly once in the vortex core where its position is recorded. It was noticed that once the vortex generating plate was too close to ground effect the inner vortex core loses its momentum and disappears. Van de Wijdeven et al. concluded that VGs in ground effect help to maintain a low pressure surface therefore improving a car's performance.

Tufts were used for visualizing the underbody flow of a car equipped with a heat source in different yaw situations in a wind tunnel (Khasow et al., 2015). The purpose of the experiment was to understand the link between underbody aerodynamics and thermodynamics in crosswinds. Epoxy glue and heavy duty reflective tape were used to attach 5 cm long and 3 mm wide tufts on the underbody of the car. It was realized that although there is a link between underbody aerodynamics and thermodynamics, the tufts were affected largely by underbody topology more than the car's yaw positions. Apart from exceptionally advanced methods (Von Funck, Weinkauf, Theisel, & Seidel, 2008), flow visualization has largely been composed of qualitative (exploratory) techniques. Quantitative (conclusive) measurement techniques on the other hand, produce numerical data that are

interpreted much easier than qualitative techniques. Quantitative fluid information includes temperature data.

2.3: Temperature Measurements

Thermocouples are the most commonly used tool of all the temperature measurement techniques, this is in response to their resilience, reliability, and affordability (Tavoularis, 2005). Thermocouples can be used to measure surface and air temperatures of various car components. This is done to assure that the operational temperatures do not exceed the designed component temperatures. Type K thermocouples are the most commonly used type and have an error ranging from ±0.75% to ±1.5%. The sources of error of thermocouple measurement are noise and leakage currents, poor junction connections, and thermal shunting. Noise and leakage currents are produced by line-related interference and can be prevented by inserting various filters. Poor junction connections are produced by overheating the wires which can degrade the accuracy. Thermal shunting is produced by the thermal energy absorption of the desired area of measurement by the thermocouple which can be avoided by using a thermocouple extension wire. Thermocouples work on the Seebeck effect. That is when a voltage difference is produced between two electrical conductors by a temperature difference between them. Consequently thermocouples are produced by joining the ends of two electric conductors by means of

soldering, welding, or pressing to produce a closed circuit. The conductor joining junction is placed in the desired region for measurement while the other, reference junction, is attached to an electronically temperature maintained heating block (Tavoularis, 2005). The reference junction is used as a reference to identify the temperature of the desired point of interest. A growing application for thermocouples is their utility in measuring temperature in aerodynamic-thermodynamic testing.

2.3.1: Aerodynamic-thermodynamic Studies

Khaled et al. (2009) assessed the thermal performance of a passenger car's underhood in different car inclinations using 80 surface and air thermocouples. The test was conducted in an automotive wind tunnel with adjustable front dynamometer rollers to simulate up-hill, flat and down-hill positions. Type T and K thermocouples were used to measure the underhood air temperature, component temperature and engine parameters. Results show that the car's underhood thermal performance is sensitive to the car's inclination. Results also showed that underhood thermal performance is affected by a declined (down-hill) configuration more than an inclined configuration. This is due to the hot air escape due to natural convection and the increased forced convection from under the underhood compartment.

Khaled et al. (2014) also investigated the effect of underhood air leakage on the underhood aero-thermal management. Temperature measurements were obtained with 100 surface and air thermocouples. Results obtained showed that air leaks out of the side, front and windshield junctions of the underhood which reduces engine compartment temperatures.

Huber et al. (2014) deduced a way of integrating new commercial cars' thermal model into their aerodynamic design process to reduce time to market. This was accomplished by comparing CFD simulations to experimental results. To experimentally simulate road conditions, a heated component was attached to the underbody of a car, K-type thermocouples were placed inside the component to measure its core temperature, and also within its vicinity to measure the surface temperature distribution.

Khasow et al. (2015) investigated the effect of car underbody thermodynamic and aerodynamic effects caused by yaw. A hot plate was attached on the underbody of the car to simulate a battery pack of typical electric and hybrid electric cars. Thermal data were obtained using K-type thermocouples. A total of 137 thermocouples were installed around the hot plate and on the underbody of the car. Thermocouples were placed in an array at a distance of 10 cm apart from the front to the rear axle. In sensitive locations (close to the hot plate) a finer array of

thermocouples at a distance 3 cm apart was used. All thermocouples were kept at a distance of approximately 5 mm from the surface of the underbody to assure the measurement of airflow boundary layer temperature. The final results show that although car yaw affects temperature distribution, underbody geometry has a more significant effect on heat distribution.

2.4: Aerodynamic Force Measurements

Typically, a force measuring system must be present to quantify the aerodynamic forces on the test car. The two main methods for measuring forces and moments are by either surface pressure measurements, or balance systems (Rathakrishnan, 2007) with the latter being the most preferable. Balance systems include wire suspension, strut, and floor type balance systems (Tropea et al., 2007a). Each of the balance system types uses load or pressure transducers to capture the different loads applied. Figure 2.2 shows a schematic of all three types of force measuring systems.

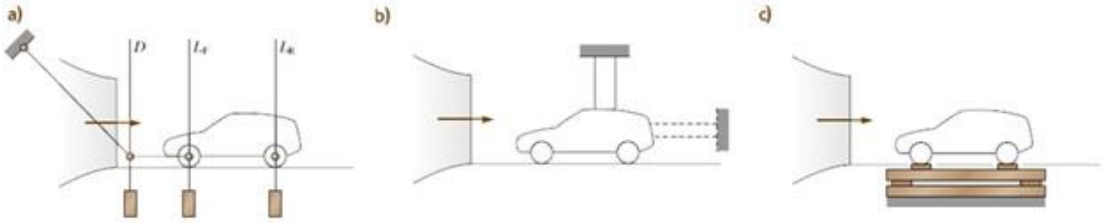

Figure 2.2: Three force measuring systems: a) string suspension b) strut system c) on a platform/floor balance (Tropea et al., 2007a)

2.4.1: Aerodynamic Forces on Floor Balances

Aerodynamic forces are measured by floor balances that are installed to flush with the wind tunnel floor. The car either rests on a single large platform or four separate small ones. The platforms are composed of force or pressure transducers, these transducers are usually calibrated to output measured values in Newtons (*N*) or pounds-force (*lbf*). Floor balance force measurement systems (FMS) can be used for either absolute or incremental force measurements. The error associated with the floor type FMS is pertinent to the load cells used. Most load cells advertise an error of <±0.5%, however when multiple load cells are used the error might significantly increase. Common sources of error for floor type FMS are; unfavourable operating environmental conditions, incorrect mounting of load cells, and unsuitable support platforms.

Carr (1982) noticed that a floor balance FMS wind tunnel contributed to a significant front axle lift coefficient of a car when compared to other wind tunnels with different balance systems. This was found to be due to the open grid plates used to rest the tires. The grid plates were replaced with 245 mm square-flat plates, the gap around each plate was later occupied with filler plates. After the modifications the front axle lift coefficient was comparable with those of the other wind tunnels, however the modification resulted in a reduction in the drag coefficient by 0.04 to 0.09. Koitrand (2013) observed from

CFD analysis that the front axle lift discrepancies might be experienced with floor balance systems, while Bucheim (1983) confirmed this experimentally using the same car in different wind tunnels.

In the aerodynamic development of an eco-marathon car, Lien (2010) utilized a large scale wind tunnel with a floor balance system. The floor balance system was one elevated, large platform mounted on a metal rig which was attached to a scale. Two wooden chocks were placed ahead and behind of the front and rear wheels respectively to keep the car in place. The aerodynamic forces in a turning configuration were also measured by rotating the platform system 15˚. The balance system is composed of six electronic load cells. Three were used to measure the vertical forces and the other three for the horizontal forces. When calibrating the load cells, weights were placed on the load cells individually and a voltage output was detected. Converting the voltage output (V) to Newtons (N) requires the deduction of a conversion constant (N/V). The calibration was later verified by applying a known load on the balance system and cross referencing with the result obtained. Due to wind tunnel breakdown the final extension to the car was not completed. Accuracy was not achieved by the balance system due to the balance system's ground elevation. Regardless, accuracy was not the main concern in this test instead it was repeatability as that is the objective of any enhancement process.

2.4.2: Aerodynamic Force Improvement

A Zakspeed formula 1 car was aerodynamically improved in a fixed ground wind tunnel (Gerhardt et al., 1986). It was found that by extending the front wings upwind of the front axle and decreasing the ground clearance results in the highest downforce. Also, extending the front wing at some distance produced a vortex interference that deflected oncoming air away from the front wheels which significantly reduced drag and increased downforce. However it was found that this configuration restricted undisturbed air from entering the radiator, therefore a front wing ground clearance height was a compromise to satisfy the radiator cooling. Diffuser opening angles were also investigated between 8˚ and 10˚ and an optimum 9.5˚ angle resulted in the highest downforce and least drag. Two rear wing positions were experimented, aft and ahead of the rear axle position. It was found that the latter configuration allowed for an increased cooling performance, but decreased the aerodynamic performance due to disturbed air at the leading edge of the wing, therefore an aft position was chosen. Also, various airfoil shapes were tested, and a thick airfoil profile resulted in the most favourable results.

An open-wheeled Indy 1/4 scale race car model was tested on a fixed ground wind tunnel (Katz et al., 2002). The objectives of the test were to quantify the distinct aerodynamic contributions of various aerodynamic device add-ons and visualize the underbody flow of the

model. The aerodynamic forces were measured using a six-component balance system that was attached to the model's wheels. The model was placed over an elevated ground plane to reduce the boundary layer thickness. The underbody flow was visualized by having a transparent plexiglass ground plane and wind tunnel floor. Overall results were comparable to data measured in larger wind tunnels using rolling ground. Aerodynamic results showed that the effect of aerodynamic devices are non-monotonic and depend on the already attached devices on the model. Consequentially, the rear diffuser was less effective when after the installation of the front and rear wing and the underbody vortex generators (VGs). Furthermore, the wings and the VGs produced the most downforce. The increase in the model car's angle of attack was noticed to increase downforce and reduce drag for higher ground clearance.

Significant computational time and over 240 wind tunnel hours were used to test and improve the 2006 Chevrolet Corvette C6 Z06 (Froling et al., 2005). The objective of the test was to improve high speed stability, increase cooling capability, and reduce the overall drag. Aerodynamic devices were used to enhance the car's aerodynamic performance. High speed stability was to be attained by reducing lift and creating a balanced lift force distribution. This was achieved by tuning the front splitter and the rear spoiler to obtain a normal force ratio of 0.48. The cooling capability was to be improved by allowing more air to

flow into the engine compartment and to the brakes. This was resolved by a unique front end opening and grille assembly, larger air extractors in the front fender sides, integrated front and rear brake cooling air ducts, and a lower flow stagnation point produced by the front splitter. Front wheel opening leading edge extensions and an air dam increased downforce and contributed to drag reduction.

Wang et al., (2008) investigated the effect of a gurney flap (GF) on wings. A GF which is a flap placed perpendicularly to the root chord line of the wing on the trailing edge. The attachment proved to increase the wing's lift performance but also increases drag, however the lift-to-drag ratio can be much favourable. The tests found that placing the flap at the trailing edge having a flap height slightly less than the local boundary layer thickness produces the best aerodynamic performance. Also for subsonic applications, GFs can be used to avoid flow separation downstream of it due to its trailing vortices.

2.5: Summary of Literature Review

This chapter reviewed wind tunnel testing, flow visualization using tufts, thermocouple usage in aero-thermal applications, and aerodynamic improvement tests. The review showed that the downside of using floor force measuring balances is that the low pressure produces lift on the front measuring plates. To avoid this, the plate balance was required to be flat and for the edges of the plate to be sealed off. Despite

this, in this study a flat plate was used that was not sealed off because, unlike in the literature, incremental results were required instead of absolute results. Furthermore, sophisticated boundary layer reduction techniques are not necessary because absolute results are not desirable for improvement-type tests. The effect of a number of aerodynamic devices were reviewed and noted to be applied to this study such as wings, front splitters, air dams, side skirts and gurney flaps. Front and rear wings were used to increase front and rear downforce respectively with a drag penalty. Front splitters boost front downforce and enhance engine compartment cooling by directing air to the front grill. Air dams constrict the air flow under the car which reduces the front pressure consequentially increasing front downforce. Side skirts prevent pressure equilibration therefore maintaining the underbody low pressure. Gurney flaps that are attached on the trailing edge of wings intensify the pressure differential above and below the wings, thus drastically increasing the downforce and drag. It was noted however that a gurney flap height slightly lower than the boundary layer thickness produces the best aerodynamic performance. The most valuable of these finding was the knowledge of reducing drag by installing a vortex-generating device upwind of the wheel well.

The literature review, however, overlooks a key element that is needed in the automotive industry which is integrated aerodynamic improvement and thermodynamic evaluation tests. These tests are

necessary to provide a comprehensive evaluation of a car's performance. This study covers the preparatory requirements for an integrated aero-thermal test by presenting the development of an integrated test facility and utilizing this capability to perform an integrated aero-thermal test.

Chapter 3 : Wind Tunnel Testing and Procedure

In this chapter the test facilities, force balances, testing protocol, and test plan for an aerodynamic-thermodynamic-wind tunnel testing is reviewed. In addition, the test cars and the attached tufts, thermocouples, and cameras used are introduced as well as their locations.

3.1: Test Facility

The tests were conducted in ACE at UOIT. ACE is a new world-class research facility. It features a CWT that is large enough to test full-size cars with wind speeds up to 250 km/hr, temperatures ranging from -40˚C to 60˚C, and humidity from 5%RH to 95%RH. It has a variable nozzle which ranges from 7 m^2 to 14.5 m^2 to accommodate a wide range of full size cars. It also is the world's only full-range CWT that incorporates a dynamometer in a large turntable for yaw testing. The turntable is 11.5 m in diameter. The test chamber's dimensions are 20.1 m in length, 13.5 m in width, and 7.5 m in height. In addition, the CWT is capable of simulating various environment conditions; rain, snow, sleet, and solar simulation using a sophisticated diurnal solar array system.

3.2: Integrated Aerodynamic and Thermodynamic Testing System

The integrated testing system being developed is one of a kind as it incorporates both aerodynamic and thermodynamic testing in the same wind tunnel. Because such a system does not exist, a differential FMS had to be designed and built to be integrated in ACE's CWT. The system was designed for easy installation and quick switching between aerodynamic and thermodynamic testing. The differential FMS consists of load cells, a data acquisition system, circuit boards, a power supply, and an interface.

3.2.1: Load Cells

The FMS was designed and built in-house. It was decided that a number of load cells was needed to build a robust system for measuring the forces on each tire of the test car. In that case the total forces are the algebraic sum of the forces on all the load cells at each tire. Two designs were considered: one that required four load cells at each tire while the other required three load cells. It was determined with rigorous calibrations that the nuances in results between the two designs were not significant enough to warrant the large extra cost associated with using four load cells per tire. Therefore, it was opted to use three load cells at each tire.

Three-axis type load cells, model TR3D-A-1K supplied by Michigan Scientific Corporation, were used for this test. The TR3D-A-1K model has a loading limit of 4448 N, the loading limit is the same for all the axes. The specifications of the TR3D-A-1K load cells from the manufacturer are shown in Table 3.1.

Figure 3.1: The box used to encase the load cells for aerodynamic testing

Figure 3.2: The TR3D-A-1K load cells used in the construction of the FMS box

Table 3.1: TR3D-A-1K load cell specifications (Michigan Scientific Corporation)

	TR3D-A-1K
Maximum load capacity (per channel)	4448 N
Full scale output	4.0 mV/V, nominal, all channels
Sensor	3 Four-arm strain gauge sensor
Non-linearity	≤0.5% of full scale output
Hysteresis	<0.05% of full scale output
Repeatability	<0.05% of full scale output
Zero Balance	Within ±10% of full scale output
Temperature Range, compensated	24˚C to 93˚C
Temperature effect on zero	<0.5% full scale
Temperature Range, usable	-40˚C to 149˚C
Excitation voltage, maximum	10V DC or AC rms
Insulation Resistance	Exceeds 5000 MΩ
Standard cable length	3 m shielded, open-ended leads

The load cells used were Wheatstone bridge strain-gauge load cells which possess four resistors connected to each other where one of which is an active sensing resistor. Therefore any change in load on the element can be translated to a change in voltage output from the strain element. In order to read this change a data acquisition system (DAQ) was used. The DAQ will be described in Section 3.2.2. The load cells were NIST traceable calibrated from the manufacturer.

The positions of the load cells on the FMS were chosen based on the dimensions of the test car. As there are only three load cells per plate there were a number of different possible arrangements and locations of the load cells inside the boxes. A number of tests were performed to determine the best location of the load cells and their distances apart. It was determined that an equilateral triangle (with one load cell on every corner of the triangle) produced the best results for the test car's tire patch. The load cell placement procedure is detailed in Appendix IV. Initial tests indicated that the signal output contained subtle levels of noise. A number of noise culprits were suggested of which was the load cells themselves. The electronic noise from the load cells were minimized by shielding the cell wires. This noticeably reduced the signal interference and yielded a cleaner output.

3.2.2: Data Acquisition System

The DAQ that was used for this system was supplied by National Instruments model number NI USB-6225 and is shown in Figure 3.3. When choosing a DAQ, a system with a large number of analog input channels was required because each load cell required two channels for each axis and as there are three axes, a total of 6 channels were required for each load cell. In addition there are a total of 6 load cells which sums up to 36 analog input channels. Fortunately the NI USB-6225 had 80 analog input channels. The DAQ was grounded to a

common source as the load cell shields. This cut down considerable noise from the output signal.

Figure 3.3: The data acquisition system (DAQ) that was used during the test

The excitation source that was used to power the DAQ is shown in Figure 3.4 which is a Duel-Tracking DC Power Supply model 6303D and was supplied by Topward. The 6303D power supply was particularly chosen for its low level noise output.

Figure 3.4: The voltage excitation source that was used to power the data acquisition system (DAQ)

A circuit board was also made to connect the DAQ to the load cells. A photograph of the circuit board is shown in Figure 3.5. The circuit board was made so as to accompany one FMS box therefore there were four circuit boards that were designed and ordered. The circuit boards connect the load cells to channels in the DAQ system. The circuit board also has a positive, a negative, and a ground port to be connected to the excitation source. In addition the circuit board has a 10k ohm resistor to allow for quick shunt scaling (section 3.2.3), as well as a 220 μF decoupling capacitor for shunting the electronic noise and stabilizing the voltage acquired from the excitation source.

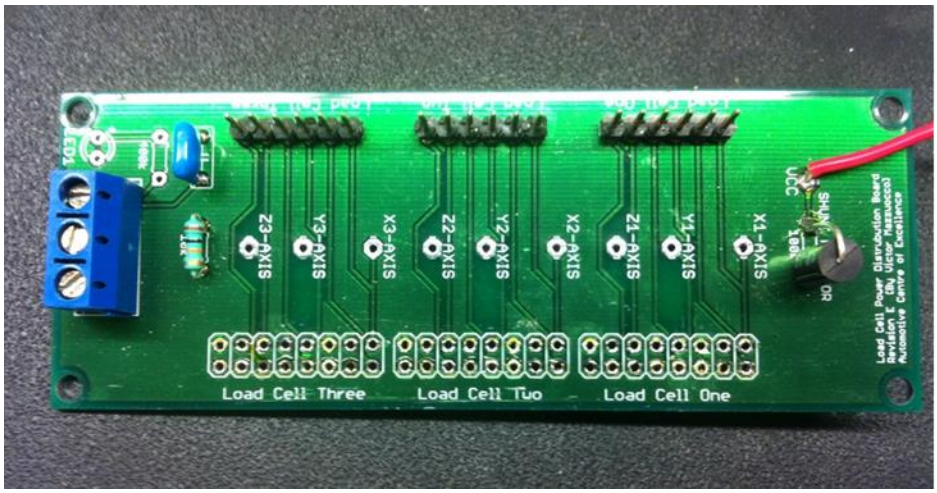

Figure 3.5: The circuit board that was used during the test for each FMS to connect the load cells with the DAQ

3.2.3: Data Acquisition Software and Scaling

The software used for the test was developed using Labview 2014. After designing a simple layout to read the data collected and displaying them in a readable method, scaling (software calibration) was next. Two scaling methods were used; load and shunt scaling methods. The load scaling method is simply applying known loads on the load cells individually and cross referencing them with the results displayed from the software. Figure 3.6 shows how the load scaling method was used for the *x, y* and *z* axes. The shunt scaling method was achieved by considering the shunt values provided by the manufacturer (Michigan Scientific Corp.). Shunt scaling was the primary scaling method because it simulates loads comparable to testing loads.

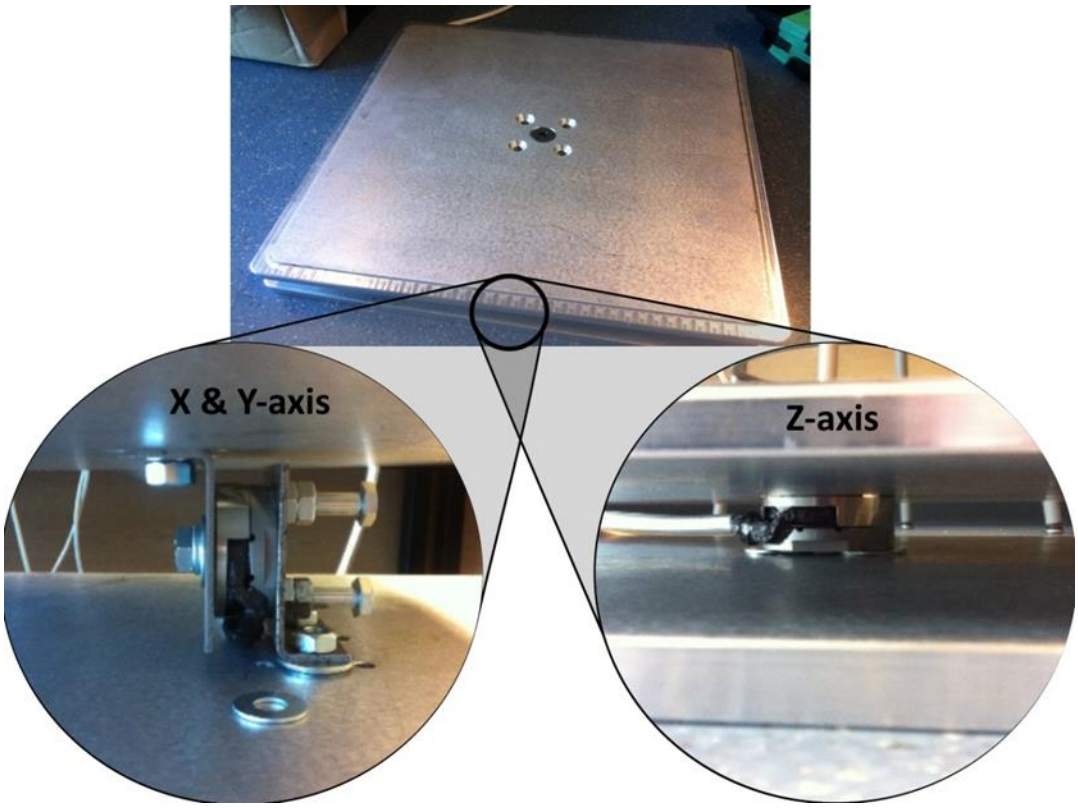

Figure 3.6: The configuration of the load cell when the *x*, *y* and *z*-axis are scaled using the load scaling method, the bottom circular images show the orientation of the load cells during scaling

The software was designed to combine all the data that was being processed and extract them in a user-friendly interface shown in Figure 3.7. The interface was designed to display incremental force values of every axis separately and cumulatively. The software was able to obtain incremental force values by offsetting/resetting the output to zero. The offset/reset function can be seen in the top centre of the screen in Figure 3.7.

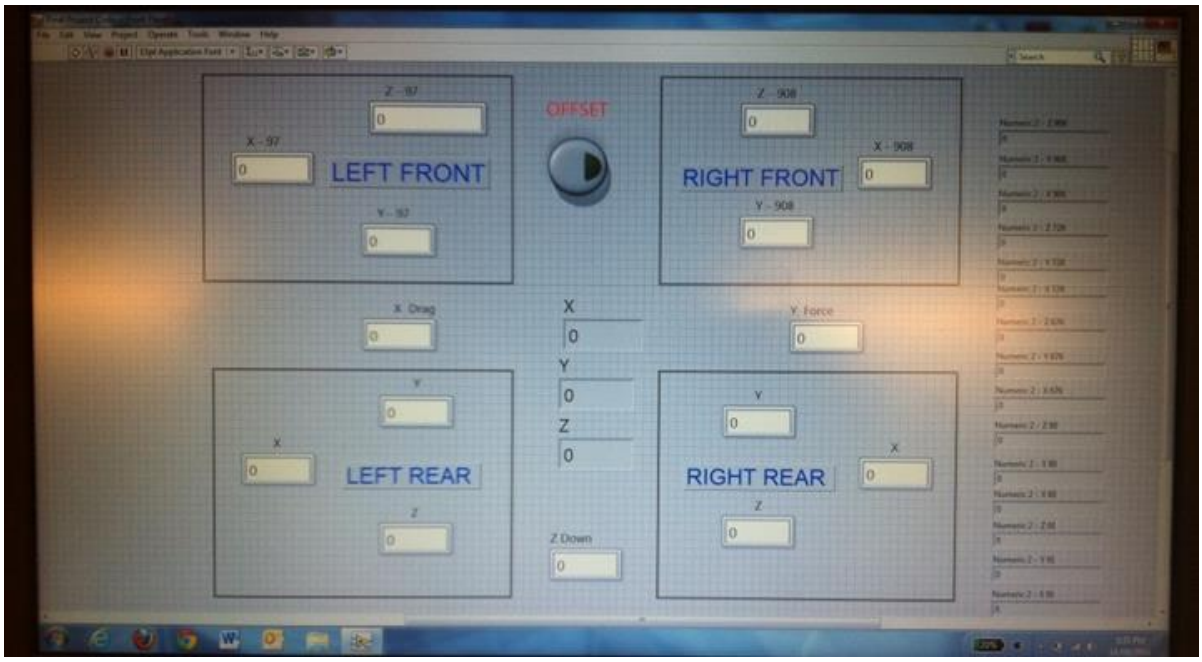

Figure 3.7: The data acquisition software user interface

The real-time values displayed on the interface were typical average values at a selected sampling rate and frequency. These rates were chosen to provide stable values with minimal fluctuation that are easy to read on the screen. The raw values however were recorded in a folder for post-processing. These raw values were later analyzed in great detail.

3.3: Test Cars and Instrumentation

Different types of information were required including local flow direction, and temperature. Cameras were used to record tufts' behaviour for underbody and upperbody locations for flow visualization. The temperatures were measured by thermocouples. Figure 3.8 and Figure 3.12 show a completely instrumented test car displaying the tufts, and thermocouples.

3.3.1: Test Cars

Four test cars were used for the wind tunnel testing. They consist of two Porsche 944 models; a 1990 S2 SP3 and a 1988 SP2, hereafter labelled as 944 Case 1, and 944 Case 2. In addition, two Porsche 2010 Cayman models; a World Challenge GTS, and a Cayman S, hereafter known as Cayman Case 1 and Cayman Case 2. These cars (Figure 3.8 to Figure 3.11) were provided by Mantis Racing. Figure 3.8 shows 944 Case 1 situated on the dynamometer with the driver seated securely ready to start thermodynamic testing. The figure also shows white tufts attached to the car for flow visualization. In addition, Figure 3.12 shows the underbody diffuser used in the test. It should be noted that the underbody diffuser was designed and fabricated in-house to test its effect on the car's aerodynamic performance, but due to testing complications its effect on only the car's thermodynamic performance

was investigated. Furthermore, tufts were attached to the rear and exhaust proximity area underbody of the car in Figure 3.12.

3.3.2: Tufts

The tufts were only placed in locations of interest to visualize the flow. To minimize the number of the tufts used, areas that are known to have a laminar flow have tufts placed farther away from each other, and areas that are known to have a turbulent flow have tufts placed closer to each other. The distances between tufts range between 10 cm and 30 cm. The tufts are secured to the surface of the car with heavy duty reflective tape and epoxy depending on the surface condition. The tufts were cut in small lengths ranging between 3.5 cm to 6.0 cm.

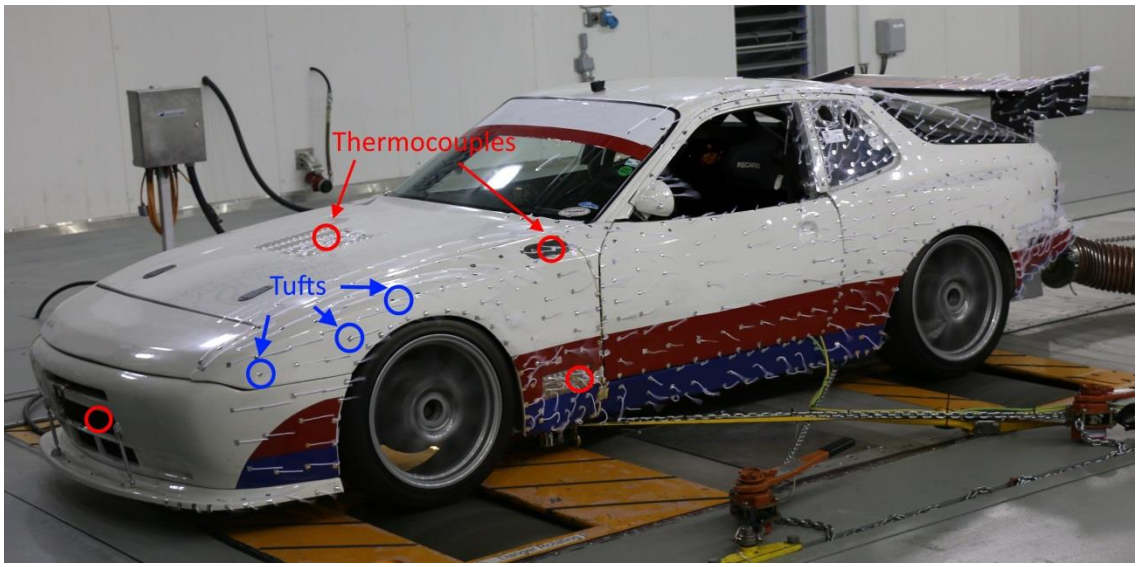

Figure 3.8: Porsche 944 Case 1 strapped down on the turntable of the CWT showing the thermocouple and tuft locations.

Figure 3.9: Porsche 944 Case 2 positioned on the FMS in the CWT

Figure 3.10: Cayman Case 1 positioned on the FMS of the CWT

Figure 3.11: Cayman Case 2 positioned on the FMS of the CWT

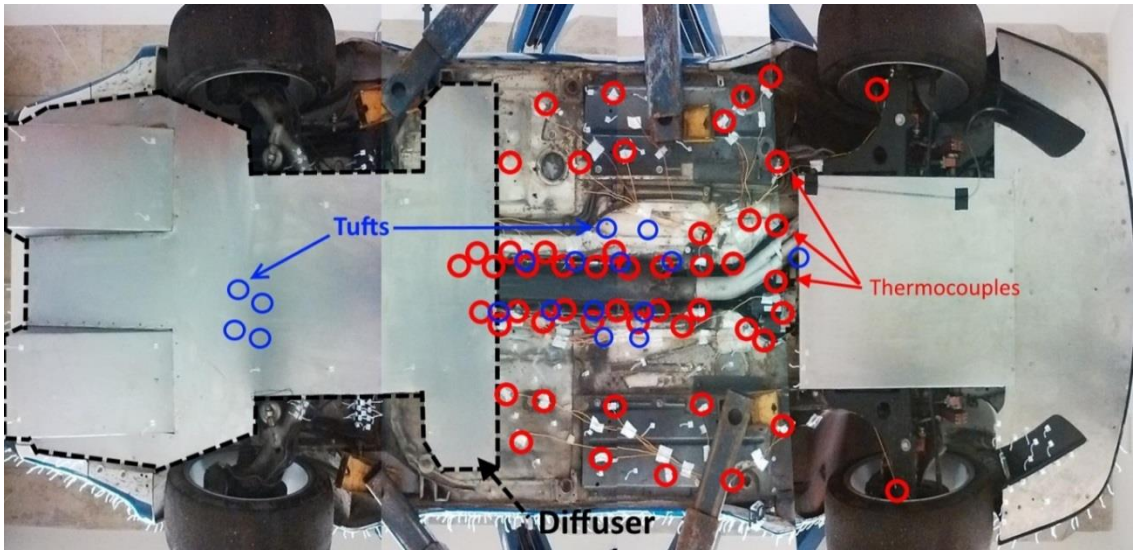

Figure 3.12: The 944 Case 1 underbody showing the locations of the tufts and thermocouples.

3.3.3: Thermocouples

The thermocouples used were K-type thermocouples which are composed of positive and negative alloy leads. The positive lead is a Nickel and Chromium alloy, while the negative lead is a Nickel and Aluminum alloy. The thermocouples' temperature range is from 0˚C to 200˚C and their accuracy is ±0.75%. Figure 3.12 shows the underbody locations of the thermocouples. Evidently the thermocouples were placed in a staggered manner as to effectively record temperature distribution on the car's underbody. The distance between underbody thermocouples is kept constant at 15 cm and at a distance of at least 10 mm from the surface to avoid surface temperature measurements. In addition, thermocouples were placed above the diffuser, behind the brakes, on the lower louvers, the upper grills, the hood louver, the inlet and outlet of the radiator, the rear tire pressure duct and differential cooling duct situated behind the passenger door.

Sixty-one thermocouples were connected to four 16-Channel K-type Ipetronik modules. These modules were later connected to a data acquisition system called TALENT Test Automation System from the company ReACT Technologies. Before testing, the thermocouples were checked and tested using a digital thermometer.

3.3.4: Cameras

Three GoPro Hero 3 cameras were strategically situated in different positions to record the behaviour of the tufts at various speeds. Two GoPro cameras were mounted on a movable floor belt to record the behaviour of underbody tufts. Another GoPro camera was used to record the upperbody side view tuft behaviour. The GoPro's resolution was 5 megapixels. A hand held Canon 70D DSLR digital camera was also used to record upperbody tufts from the front and rear view of the car. The Canon's resolution was 20.2 megapixels.

3.4: Testing Protocol

A testing protocol was developed as a reference for integrated aerodynamic and thermodynamic testing of cars. This was established through several testing attempts by first testing the car aerodynamically then thermodynamically. It was estimated that the transition between aerodynamic and thermodynamic testing is about 30 minutes. Figure 3.13 shows a flowchart depicting the protocol for the integrated aero-thermal testing.

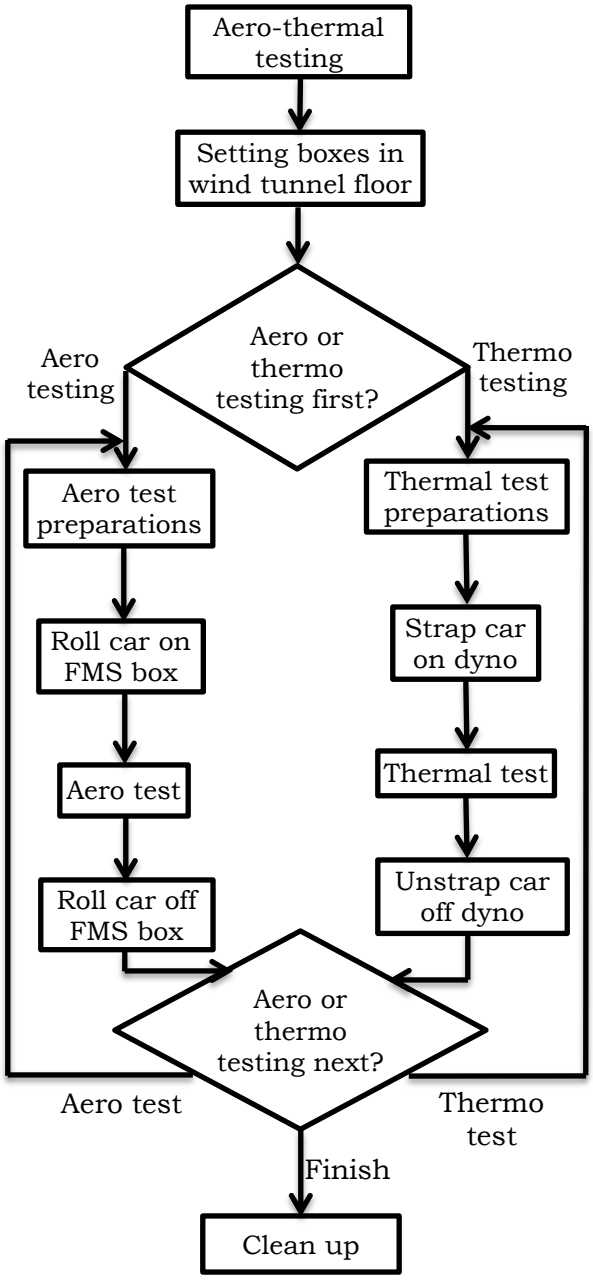

Figure 3.13: Flowchart showing the integrated aero-thermal testing protocol.

Detailed explanations of the boxes in the flowchart are mentioned below. The order is such that an aerodynamic test is conducted before a thermal test.

3.4.1: Aero-thermal Test Preparations

1. Bring in calibrated FMS on a trolley to the CWT.

3.4.2: Setting Up FMS Boxes in the Wind Tunnel Floor

1. Location of the FMS boxes in the CWT floor are pre-determined by the wheelbase of the car
2. Typically the front FMS boxes are located 2-3 slats behind front dynamometer wheels. Avoid the curved slats.
3. Remove four slats where the FMS will be installed. Set the flat head screws aside. They will not be used for the FMS.
4. Throw away the screws with damaged hex heads and use new screws when putting slats back in.
5. Use pry bars to remove the slats. Set slats aside for now.
6. Ideally three people are required to lift the FMS boxes into the floor opening. Two people will lift the FMS box with large tee handles, and one person will direct the wires into the catwalk area. Ensure the wires do not get pinched or damaged!
7. Install the flat head screws from the bag marked "sensor box mounting screws". Do not tighten screws until they are all installed. Only four screws are needed on each side of the FMS box. Note: You may have to pry the box a bit in order to get the screws to line up. Tighten the screw once all eight of

them are installed. Note: Do not over tighten the screws, it will damage the hex head.

8. Repeat the operations above for the remaining three FMS boxes. All plates are marked with location and wind direction.

9. Stack the removed floor slats onto the four wooden cradles. They can be stacked four high and moved out of tunnel.

10. In the basement, extend the clamps on the sides of the FMS boxes. These prevent the FMS boxes from moving sideways during testing.

11. Bring the jack posts and clamps up onto the catwalk.

12. Sit a jack post onto the "U" channel below the FMS box.

13. The top of the jack post has a threaded shaft that is raised into the hole of the plate on the bottom of the FMS box. Note: Do not over tighten the shaft, it will lift the FMS box. Just make contact in order to keep the FMS box from sinking down.

14. Place a clamp plate around the base of the jack post and clamp to the side of the "U" channel.

15. FMS boxes are now ready for wiring.

3.4.3: Aero test preparations

1. Cover dynamometer wheels with aluminum sheet cover.

3.4.4: Rolling Test Car onto the FMS

1. Mark the FMS plate with markings to show where the car tires should be located.
2. Before rolling the car onto the FMS assure that the corner screws on each FMS box is tight to avoid sensor damage.
3. Once the car is in place over the FMS, apply both foot and hand brakes to keep the car in place.
4. Untighten the corner screws on the FMS plates.

3.4.5: Aerodynamic Testing

Testing is conducted according to the desired test plan.

3.4.6: Rolling Test Car off the FMS

1. Release the test car's hand and foot brakes.
2. Tighten the corner screws on the FMS before rolling the car off.

3.4.7: Thermodynamic Testing Preparation

1. Remove the dynamometer cover plates from the dynamometer wheels.
2. Roll car onto the dynamometer wheels.
3. Strap car down.
4. Attach exhaust hose outlet to the exhaust.
5. Install the CO_2 fire-suppression hose into the engine compartment from below.

6. Ensure the presence of a toxic gas indicator in the car.

3.4.9: Thermodynamic Testing

Testing is conducted according to the desired test plan.

3.4.10: Unstrap Test Car off the Dynamometer

1. Unstrap the car, remove the exhaust hose.
2. Roll car off dynamometer.

3.4.11: Cleaning Up

1. Reverse the “Setting up FMS boxes” steps to remove FMS.
2. Make sure there are no screws lying around.

3.5: Test Matrix

Two main sets of tests were conducted. The aerodynamic test and thermodynamic test were conducted to obtain a comprehensive understanding of the effects of aerodynamic modifications and the heat distribution around the car.

3.5.1: Aerodynamic Test

The purpose of the aerodynamic tests was to provide the differential force of multiple cars’ downforce, drag, and side force effects. The aerodynamic test was made up of 22 tests. Each test consisted of 4 wind speeds; 100, 140, 180 and 220 km/hr. Four speeds were chosen for the test as to accommodate the limited allocated wind tunnel test time. The speed range was chosen based on the maneuvering speed

range of the cars in a race track. A yaw angle of 0˚ was used for all the tests. On top of that there were different aerodynamic devices such as wedged hatch, wedged rear, the high wing, the low wing and other modifications were applied to the test cars. This was necessary for the aerodynamic improvement of the performance of the cars. The test matrices for the aerodynamic tests are shown in Table 3.2a, **Error! Reference source not found.**b, and **Error! Reference source not found.**c.

Table 3.2a: The test matrix of the aerodynamic test

Test	Wind speed (km/hr)	Comments
1	100 140 180 220	Baseline of 944 Case 2 (with extended front splitter)
2	100 140 180 220	Repeated baseline of 944 Case 2
3	100 140 180 220	Baseline of 944 Case 2 with 3 cm offset of original baseline
4	100 140 180 220	944 Case 2 baseline with wedged rear hatch
5	100 140 180 220	944 Case 2: Attached tape on the hood, placed rear wedge, installed front canards & secured rear window to Test 4

Table 3.3b: The test matrix of the aerodynamic test

Test	Wind speed (km/hr)	Comments
6	100 140 180 220	944 Case 2: Same as Test 5 but without front canards
7	100 140 180 220	Baseline of 944 Case 1 with full width chin splitter and side skirts
8	100 140 180 220	944 Case 1: Removal of chin splitter, installation of rear wedge, front canards, and small wing of Test 7
9	100 140 180 220	944 Case 1: Same as Test 8 but with closed vents
10	100 140 180 220	944 Case 1: Placement of rear wedge, high wing and vents open of Test 9
11	100 140 180 220	944 Case 1: One bolt hole lower for the rear wing of Test 10
12	100 140 180 220	944 Case 1: Lower radiator of Test 11 taped
13	100 140 180 220	944 Case 1: Full width chin splitter installed to Test 12
14	100 140 180 220	Baseline of Cayman Case 2 (with extended front splitter and low rear wing)

Table 3.4c: The test matrix of the aerodynamic test

Test	Wind speed (km/hr)	Comments
15	100 140 180 220	Cayman Case 2: 1.5 cm rear wedge placed to Test 14
16	100 140 180 220	Cayman Case 2: 2 cm gurney flap on rear wing to Test 15
17	100 140 180 220	Cayman Case 2: A 3 cm rear wedge instead of 1.5 cm rear wedge of Test 16
18	100 140 180 220	Baseline of Cayman Case 1 (with high rear wing)
19	100 140 180 220	Cayman Case 1: Extended front splitter and one bolt size higher rear wing to Test 18
20	100 140 180 220	Cayman Case 1: Placement of 1.5 cm rear wedge to Test 19
21	100 140 180 220	Cayman Case 1: Installed 2 cm gurney flap to Test 20
22	100 140 180 220	944 Case 1: Modified front splitter, and modified nose added to Test 12

3.5.2: Thermodynamic Test

For the thermodynamic test there were 9 tests performed in total at a speed of 160 km/hr. The tests were conducted while the car was operating by a sit-in driver on the dynamometer to capture real-time temperature data. A speed of 160 km/hr was chosen for the testing because it was estimated to be the average driven speed around a race track. A yaw angle of 7.5˚ was also experimented with. The test matrix of the thermodynamic test is shown in Table 3.5.

Table 3.5: Test matrix of the thermodynamic test

Test	Wind Speed (km/hr)	Yaw Angle	Comments
1	160	0	With Diffuser
2	160	0	With Diffuser
3	160	0	With Diffuser
4	160	0	With Diffuser
5	160	7.5	With Diffuser
6	160	7.5	With Diffuser
7	160	7.5	With Diffuser
8	160	7.5	With Diffuser
9	160	0	Without Diffuser

Chapter 4 : Results and Discussion

4.1: Aerodynamic Tests and Results

Four car cases were aerodynamically tested using the FMS (944 Case 1, 944 Case 2, Cayman Case 1, and Cayman Case 2). Details of these test cars are shown in Section 3.3.1. The FMS was used to measure the incremental aerodynamic forces acting on the cars and the test results were then used to improve the cars aerodynamically. In this thesis aerodynamic improvement implies the use of aerodynamic devices to modify the aerodynamic forces on the car to achieve various goals such as improving stability, manoeuverability, efficiency and increasing speed in cornering. The aerodynamic devices used for these improvement tests are shown in Appendix II. However, before the utilization of the FMS, error analyses were conducted to ensure the validity of the improvement results.

4.1.1: Error Analysis

The FMS' load cell specifications in Section 3.2.1 include nonlinearity, repeatability, hysteresis, temperature effect on zero, and zero balance errors. The zero balance error exists when the signal of the load cell in the no load condition is not zero. The FMS contains a reset function, thus the FMS is minimally affected by the temperature effect on zero and zero balance errors. Therefore only nonlinearity,

repeatability, and hysteresis errors are considered. The measurement accuracy of the load cell is the combination of all the three errors. However for aerodynamic improvement of a car, repeatability is the main concern. This is because the improvement of a car is determined by the incremental effect of every modification. Therefore, the incremental change of the aerodynamic forces is more important than their absolute values. To determine the incremental change of the forces, the repeatability of the system is the major concern. Nonlinearity and hysteresis errors (Appendix V) do not contribute as significantly in the system's capability of determining the incremental forces. Therefore only the FMS's repeatability is tested. There are other sources of error affecting the FMS's readability such as electronic noise. This however is assumed to be included in the repeatability error range.

4.1.1.1: Repeatability Test

The repeatability study was conducted on 944 Case 2 as it was the first test car to be tested. A test was performed to record the car's baseline, and this was repeated two more times. The test conditions are shown in Table 4.1.

Table 4.1: Repeatability test conducted on 944 Case 2

Test	Wind speed (km/hr)	Description
1	100 140 180 220	Baseline (No aerodynamic components)
2	100 140 180 220	Repeated baseline
3	100 140 180 220	Baseline with 3 cm offset of baseline

The first test in Table 4.1 was conducted by rolling the car on the recommended tire patch position on the FMS to measure the incremental forces. For the second test the car was rolled off the FMS and then rolled back onto the same recommended tire patch position and the incremental forces were measured again. The third test was conducted by rolling the car off and then back onto the FMS with a 3 cm offset from the recommended tire patch position. For each test, four speeds were studied. The incremental drag force, downforce, and side force results are discussed separately.

4.1.1.1.1: Incremental Drag Force Results

The drag force results obtained for the repeatability tests are shown in Figure 4.1. The figure shows that the drag force results of the tests for all the speeds almost collapsed on one another.

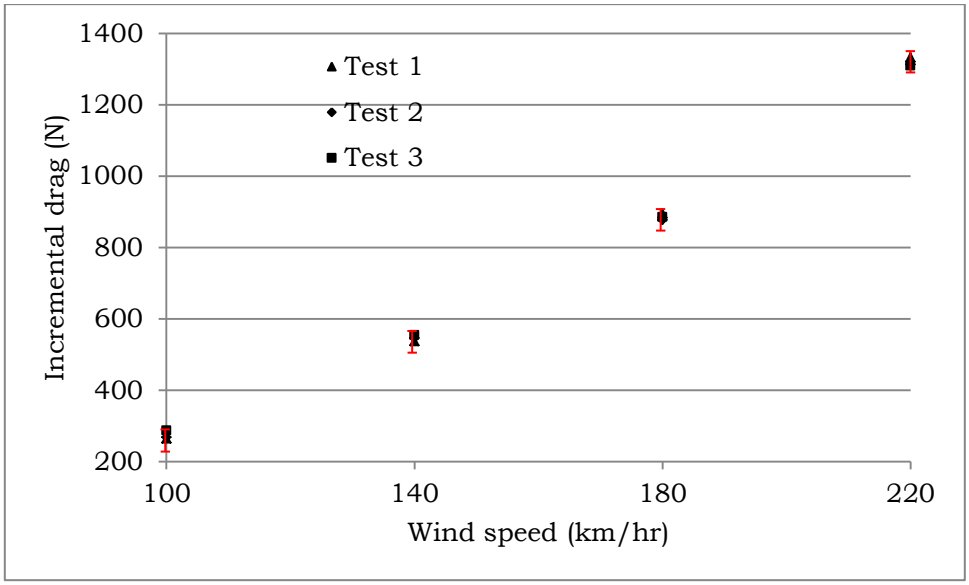

Figure 4.1: Drag force repeatability results for 944 Case 2

The repeatability of the incremental drag results had a standard deviation of ±9.9 N. The FMS is therefore considered repeatable for incremental drag in this range.

4.1.1.1.2: Incremental Downforce Results

The incremental front and rear downforce repeatability test results are shown in Figure 4.2. The standard deviation of the incremental front downforce results is ±9.6 N. In addition, the standard

deviation of the incremental rear downforce results is ±9.2 N. The FMS is therefore considered repeatable for incremental downforce in this range.

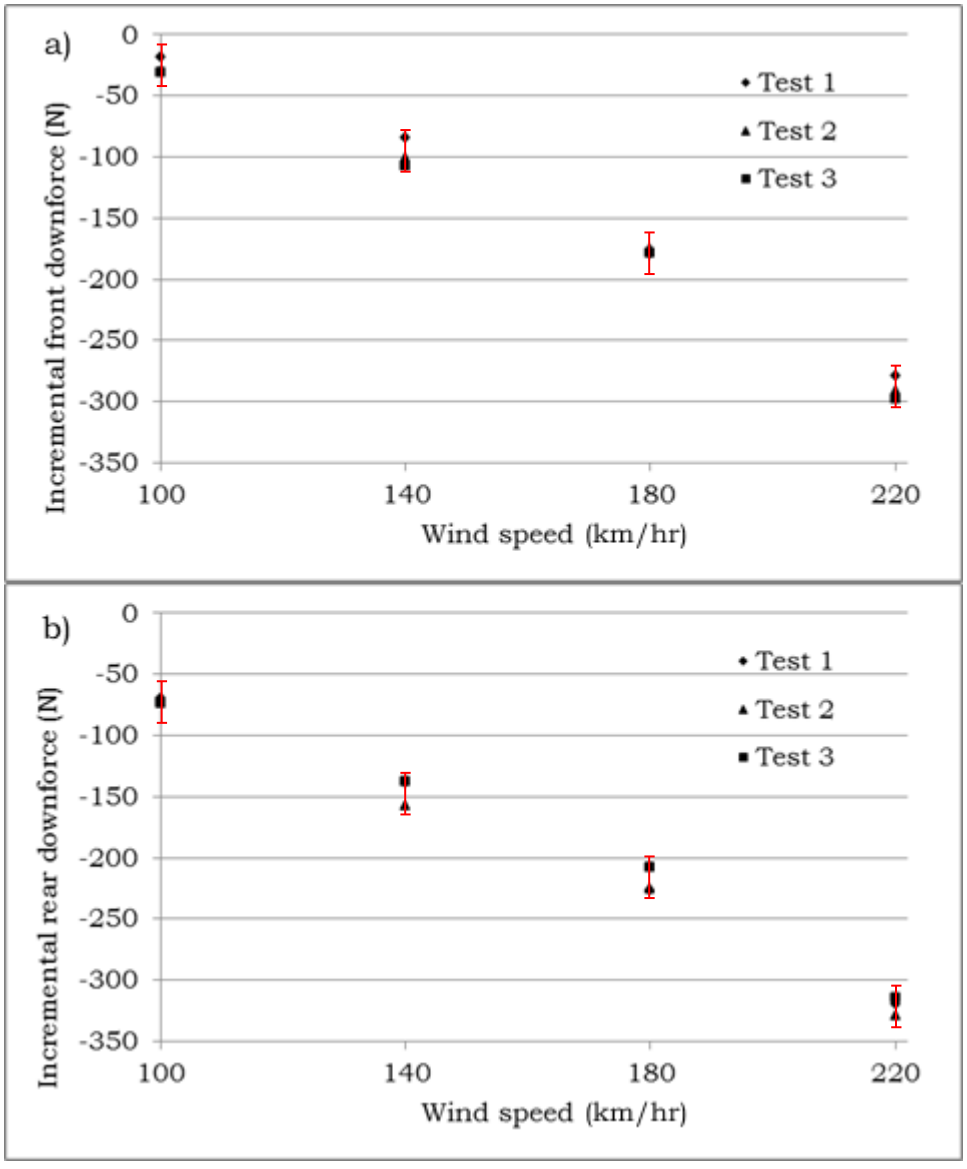

Figure 4.2: Repeatability results for 944 Case 2 for a) front downforce and b) rear downforce

4.1.1.1.3: Side Force Results

The side force results obtained for the repeatability test are shown in Figure 4.3. In ideal conditions, a car in 0˚ yaw does not have any side forces.

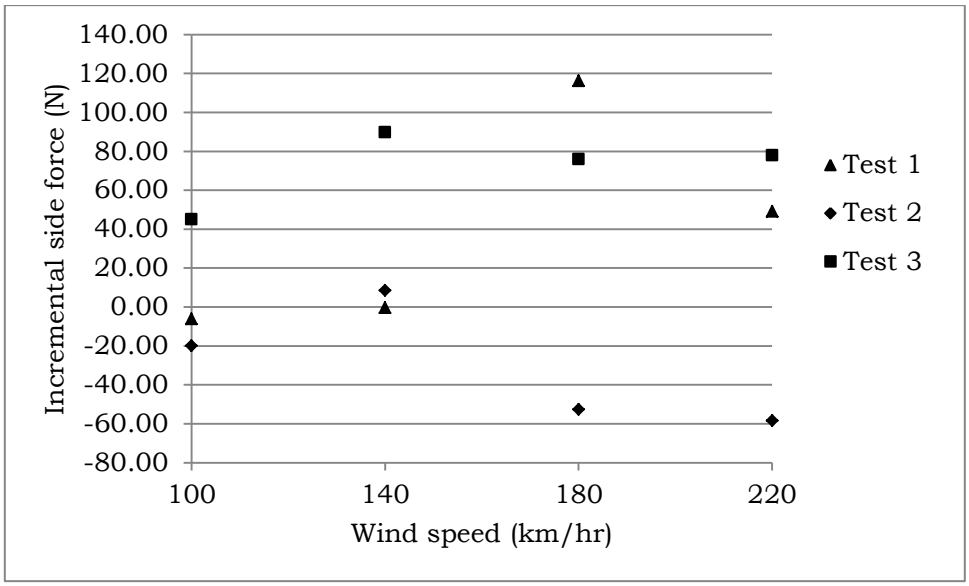

Figure 4.3: Incremental side force repeatability test results for 944 Case 2

Test 1 and 2 of the repeatability test are considered to be placed in the exact same position, in the figure the two tests show similar results for speeds 100 and 140 km/hr however different results for 180 and 220 km/hr. This was attributed to the shaking and swaying of the test car at high speeds due to turbulence. Test 3 however shows consistently positive test results. This is attributed to the wind tunnel's non-uniform pressure distribution. As the figure shows, the test results are scattered

thus not repeatable. Based on these results it was decided that side forces were not repeatable and they were therefore not analyzed in this thesis.

4.1.2: Aerodynamic Force Improvement of 944 Case 1

The aerodynamic force improvement tests for 944 Case 1 are shown in Table 4.2. The objective of the test was to modify the front and rear downforces and reduce the drag force for better car stability, efficiency and cornering speed. This was achieved by using selected aerodynamic devices including front canards, rear wings, chin splitters, and rear wedges (to simulate a change in the car's angle of attack). Pictures of these devices are shown in Appendix II. The initial baseline of 944 Case 1 had a full width chin splitter and side skirts installed.

Table 4.2: Improvement tests for 944 Case 1

Test	Car modification
1	Baseline (full width chin splitter and side skirts)
2	Placement of 1.5 cm rear wedge, front canards, and small wing to Test 1 but without full width chin splitter
3	Same as Test 2 but with closed vents
4	High wing and open vents to Test 3
5	One bolt hole lower for the rear wing of Test 4
6	Lower radiator of Test 5 taped
7	Full width chin splitter installed to Test 6
8	Modified full width chin splitter extension to Test 6

Four speeds were used for each test, 100, 140, 180, 220 km/hr. This speed range was performed to accommodate the cars' manoeuvering speed range on a real track. The improvement results for

all tests were plotted separately for incremental rear downforce, front downforce and drag force.

4.1.2.1: Incremental Downforce Improvement Results

The incremental front and rear downforce improvement test results are shown in Figure 4.4 (a) and (b) respectively. From the figures, the baseline incremental results (Test 1 from Table 4.2) showed very high negative rear downforce compared to the front. The first goal was to increase the rear downforce.

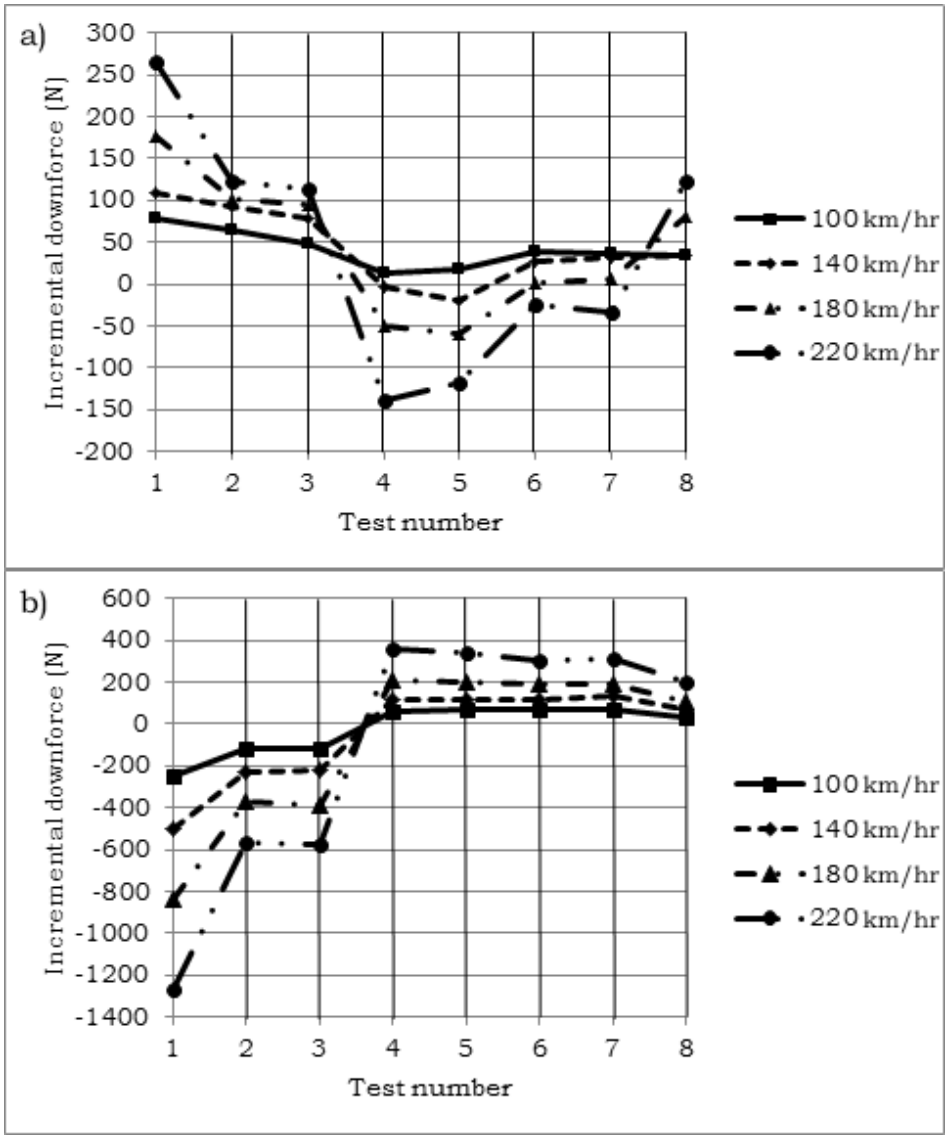

Figure 4.4: Incremental downforce improvement test results for 944 Case 1 at 100, 140, 180 and 220 km/hr for (a) front downforce and (b) rear downforce

For Test 2 (Table 4.2), two side front canards, a small rear wing and a rear wedge were installed. The purpose of the front canards is discussed in the incremental drag improvement section (Section 4.1.2.2). The small rear wing and the rear wedge were installed to increase the

rear downforce. The rear wedge was positioned to simulate an increase in the test car's angle of attack. Figure 4.4 shows that these devices used in Test 2 increased rear downforce but decreased front downforce. The rear downforce increased because the small rear wing created asymmetric flow around it which created pressure differential. The rear wedge increased rear downforce by increasing the angle of attack of the car. The front downforce decreased due to the increase in the rear downforce resulting from the rigidity of the car's chassis. In Test 3 the rear vents were covered to examine their aerodynamic effect. The results in Figure 4.4 showed that covering the rear vents slightly decreased the front downforce but did not significantly affect the rear downforce. The decrease was due to a high underbody pressure region that was formed. This was because the rear vents allowed underbody air to escape which reduced the underbody pressure. The vent coverings were removed in Test 4. Also in Test 4 the small rear wing was replaced with a high rear wing to further increase rear downforce. The results showed the highest rear downforce results. This is because the higher the rear wing (closer to free stream) the more asymmetrical the flow around the wing which would increase the pressure differential resulting in increased downforce. This significant increase in the rear downforce also caused the front downforce to decrease due to the chassis rigidity. In Test 5 the high rear wing's angle of attack was decreased to reduce the rear downforce. The smaller angle of attack resulted in a decrease in the rear

downforce as expected. This is because with a decrease in the angle of attack of the wing, the pressure differential decreases. This resulted in an increase in the front downforce. The lower radiator was then covered in Test 6 to investigate its aerodynamic effect. The results indicate that it increased the front downforce and decreased the rear downforce. The front downforce increased because more air is constricted under the car than flow through the radiator. Although the front downforce increased slightly in Test 6 by covering the lower radiator, more front downforce was required to produce a positive front incremental downforce. Thus a full width chin splitter was attached in Test 7. The full width chin splitter had no effect on the downforces. This is because the chin splitter was not streamlined. For Test 8, the car's front end was modified by installing a streamlined full width chin splitter extension to increase front downforce. This increased the front downforce and decreased the rear downforce as shown in Figure 4.4. This was because of the low pressure region created under the extension and the high pressure region created over it. The low pressure region under the extension was created by more aggressive air constriction which increased air speed and created a low pressure region under the extension. The high pressure region above the extension was created by stagnated air on the extension.

4.1.2.2: Incremental Drag Force Improvement Test Results

The incremental drag force improvement results are shown in Figure 4.5. Front canards were installed on the sides of the car in Test 2 (Table 4.2) to compensate for the increased drag produced by the rear wing. The rear wings increased drag because they are obstructions to the air flow.

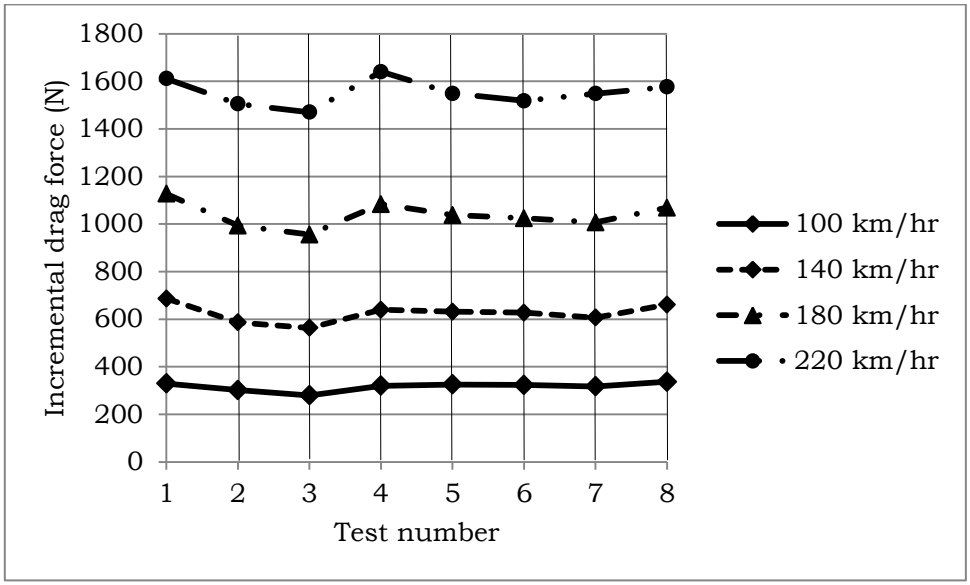

Figure 4.5: Incremental drag force improvement test results for 944 Case 1 for speeds 100, 140, 180 and 220 km/hr

As shown from Figure 4.5 the incremental drag force decreased in Test 2. This was because the side front canards generated strong vortices which prevented flow separation and reduced the drag force, similar to vortex-generating devices in previous studies (Froling et al., 2005; Gerhardt et al., 1986; Wang et al., 2008). The rear vents of the car

were closed for Test 3 which decreased the drag force in comparison to the previous test. This was because a high pressure region was formed under the car's front. A high pressure region under the front of the car will reduce air flow under the car which would decrease the underbody drag. With the installation of a higher rear wing and the removal of the front canards in Test 4, drag increased remarkably from the previous test as indicated in Figure 4.5. This was because a larger rear wing would produce more drag due to greater air resistance. Also the installation of the front canards reduced drag force so their removal would consequentially increase drag force. The lower angle of attack used in Test 5 decreased the drag force as the lower angle of attack reduced the frontal area of the wing. The taping of the lower radiator in Test 6 slightly decreased the drag force. This was attributed to taping which made the lower radiator more streamlined. The full width chin splitter installed in Test 7 caused a slight increase in drag force. This was because the full width chin splitter was not streamlined. The modified full width chin splitter extension attached in Test 8 also increased the drag force. This was due to the high pressure created at the front of the car by air stagnation on the extension.

In Chapter 1 the drag equation was introduced (Equation 1.1). The drag equation relates the drag coefficient of a body moving through fluid to the ratio of the drag force produced on the body to the force produced by the dynamic pressure multiplied by the projected area. Plots of

incremental drag force against the force produced by the dynamic pressure for all the 944 Case 1 tests are shown in Figure 4.6. The force produced by the dynamic pressure of the air was obtained by multiplying the dynamic pressure of the air by the projected area of the car. The projected area of the car was obtained from the manufacturer. A theoretical relationship obtained by using the advertised drag coefficient of the Porsche 944 series was also plotted on the figure for comparison.

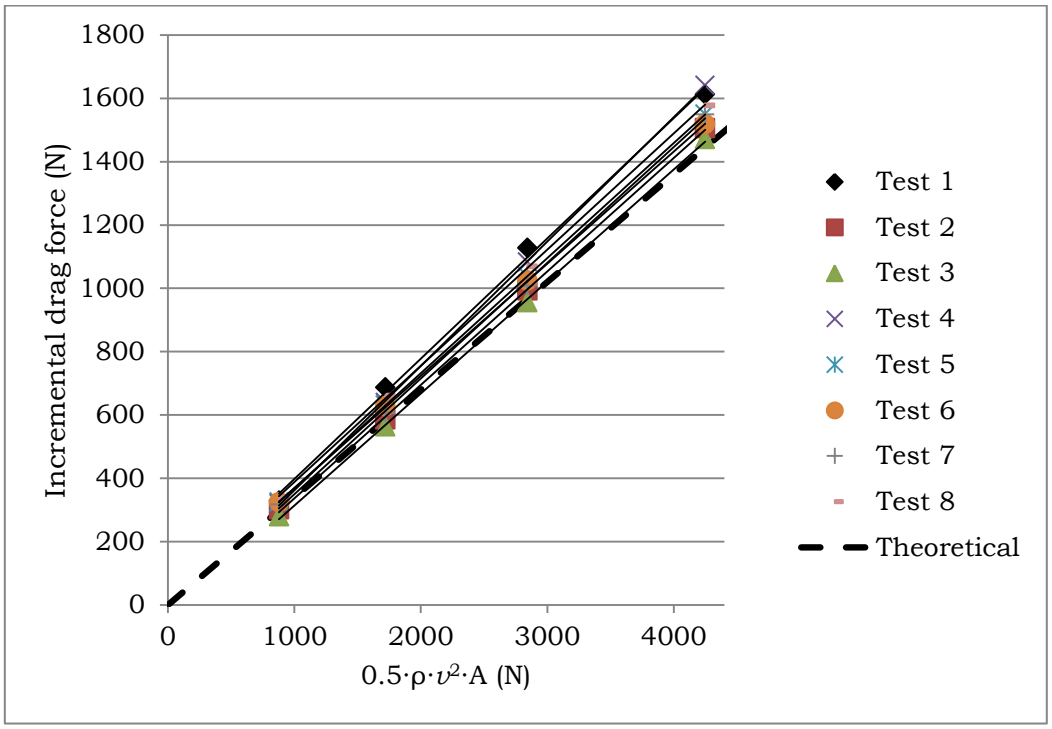

Figure 4.6: Plots of incremental drag force versus dynamic pressure ($0.5 \cdot \rho \cdot v^2$) and project area (A) of 944 Case 1

Linear regression lines were fitted to the obtained test results. An average coefficient of determination (R^2) of all the regression

lines in Figure 4.6 was found to be 1.0. The differences in linear regression lines of the tests are attributed to the test modifications. The theoretical result representing the drag coefficient of Porsche 944 series car was plotted to gauge the reliability of the FMS. The drag coefficients of the linear regression lines had a standard deviation of ±9% to the theoretical drag coefficient. The slight differences however between the test results and the theoretical values are attributed to car modifications, different car trims, testing conditions, and measurement errors.

4.1.2.3: Summary

Aerodynamic improvement was applied to 944 Case 1 which initially had a high front downforce and a low rear downforce. Through the application of a series of aerodynamic devices, positive incremental downforce was obtained to increase stability, efficiency and cornering speed. Figure 4.7 shows a summary of the incremental front and rear downforces, and the drag force for 944 Case 1 at 220 km/hr. The highest speed of 220 km/hr is shown to clearly display the effect of the aerodynamic devices on the forces. Note that the drag force is on the vertical axis on the right hand side of the plot.

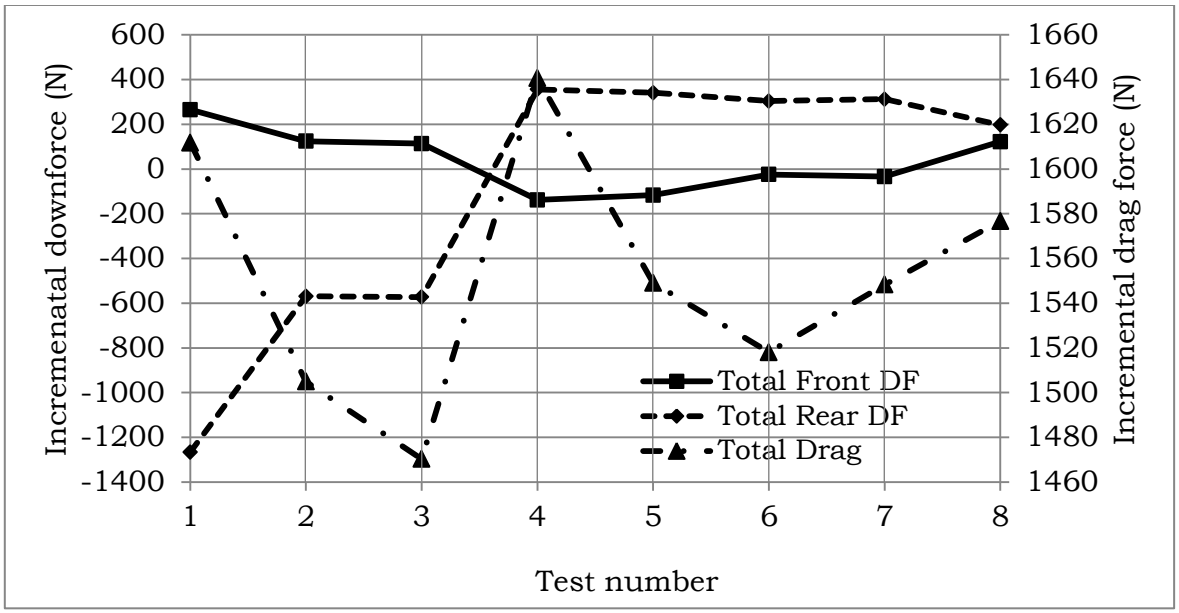

Figure 4.7: Improvement test incremental results for 944 Case 1 at 220 km/hr

The rear wings proved excellent components to increase rear downforce as demonstrated by Tests 2 and 4 in Figure 4.7. Tests 2 and 4 also showed that when front canards were placed perpendicular to the flow they decreased the drag force. The modified full width chin splitter extension in Test 8 increased the front downforce. It is also evident from the figure that by modifying the front or the rear downforce the other force (rear or front downforce) has the opposite effect. However, a relationship was not extracted between the drag force and the downforce. This is because each modification has a unique effect on the aerodynamic forces.

4.1.3: Aerodynamic Force Improvement of 944 Case 2

The aerodynamic force improvement test conditions of 944 Case 2 are shown in Table 4.3. The objective of this improvement was to maximize the incremental front and rear downforce and minimize the incremental drag force to enhance the car's manoeuverability, efficiency and cornering speed. Aerodynamic devices such as front canards, and rear wedges were used (see Appendix II). The baseline for 944 Case 2 was the Porsche 944 without any aerodynamic devices. However, it is noteworthy to mention that the car has a built-in rear wing.

Table 4.3: Improvement tests for 944 Case 2

Test	Car modification
1	Baseline (with extended front splitter)
2	Wedged rear hatch to Test 1
3	Attached front tape on the hood, placed 1.5 cm rear wedge, installed front canards & secured rear window to Test 2
4	Same as Test 3 but without front canards

Each modification was run at four speeds; 100, 140, 180, and 220 km/hr for the reasons stated earlier. The incremental front and rear downforce, and drag force results of 944 Case 2 were investigated separately.

4.1.3.1: Incremental Downforce Improvement Results

The improvement results for the incremental front and rear downforce were measured and plotted in Figure 4.8. From the figure the baseline condition (Test 1 of Table 4.3) does not provide any downforce.

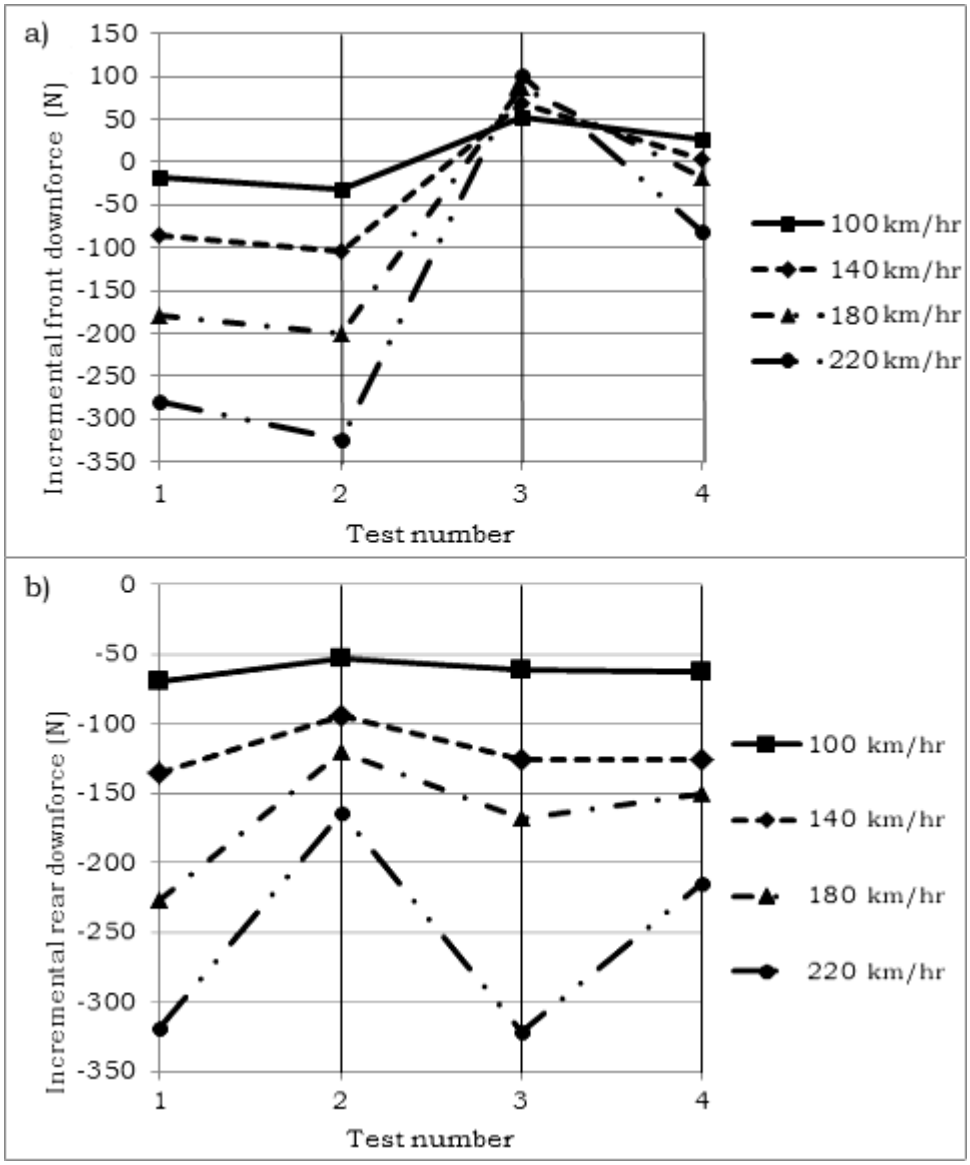

Figure 4.8: Incremental downforce improvement test results for 944 Case 2 at 100, 140, 180 and 220 km/hr for (a) front downforce and (b) rear downforce

For Test 2 (Table 4.3) the rear hatch of the car was wedged to investigate its effect on aerodynamics. The rear hatch is shown in Figure II.6 of Appendix II. The results in Figure 4.8 show that the rear downforce increased because the wedged hatch of the car constricted the air flow over the car. This flow created pressure on the built-in rear wing which generated rear downforce. The front downforce decreased because of the chassis' rigidity. In Test 3, tape was used to cover the slots around the hood, two side front canards were installed, a rear wedge was placed, and the rear window was secured. The tape and the front canards were used to decrease the drag force, the rear wedge was placed to increase the rear downforce, and the rear window was only secured for safety. These changes significantly increased front downforce but decreased rear downforce as shown in Figure 4.8. The front downforce increased because the front canards were unintentionally placed at an angle to the flow. This deflected the air flow upwards and produced front downforce. The effect of the rear wedge was not noticeable due to the effect of the front canards. The effect of the attached components on the drag force will be discussed in Section 4.1.3.2. In Test 4 the front canards were removed which decreased the front downforce and increased the rear downforce as shown in Figure 4.8. When Test 4 is compared to Test 2 (both are without front canards), Test 4 shows a greater front downforce and a lower rear downforce, this was due to the rear wedge. Although the rear wedge had been installed to increase rear downforce, the angle

of attack increase created a high pressure region on the already-installed front splitter which produced a front downforce.

4.1.3.2: Incremental Drag Force Improvement Results

The improvement results for the incremental drag force was measured and plotted in Figure 4.9. The test results of Test 2 (Table 4.3) increased the drag force. This was because the car's wedged rear hatch caused the constricted air to increase the pressure on the built-in rear wing which increased the drag force.

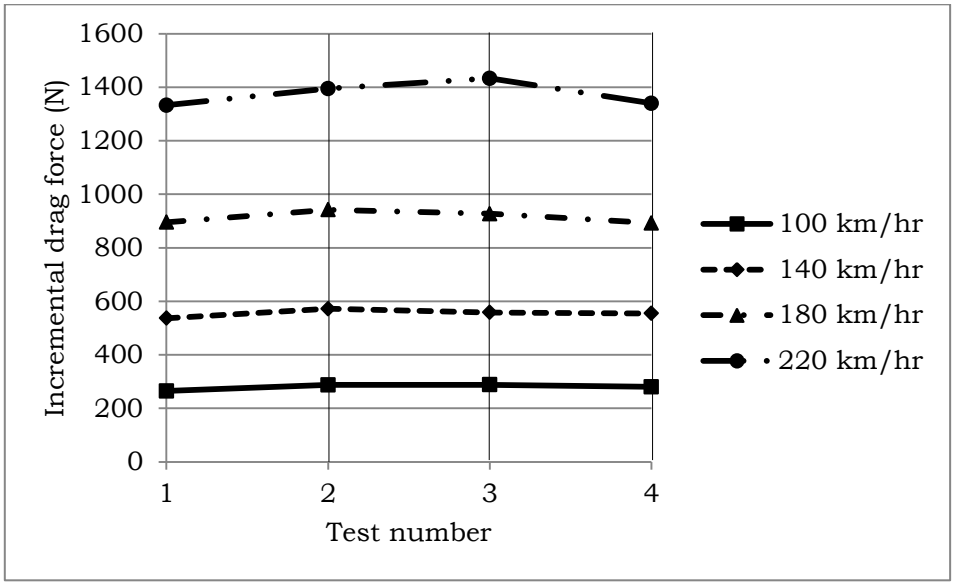

Figure 4.9: Incremental drag force improvement test results for 944 Case 2 for speeds 100, 140, 180 and 220 km/hr

The drag force in Test 3 increased as shown in Figure 4.9. This was attributed to the rear wedge and the angled placement of the front canards. The rear wedge increased the car's angle of attack which

increased the asymmetric flow over the car. This increased the pressure on the car's built-in rear wing which elevated the values of the drag force. The angled placement of the front canards raised the drag force as well because they were placed at an angle to the flow. This did not create strong enough vortices to prevent separation and to decrease the drag force. In Test 3 the hood slots were covered by tape to decrease the drag force however their effects were not noticeable compared to the effects of the rear wedge and the front canards. The canards were removed in Test 4 to confirm that they increase drag. Drag decreased in Figure 4.9 which confirmed that angled canards increased the drag force. When Test 4 is compared to Test 2 (both without front canards), Test 4 has a lower drag, this was due to the tape that streamlined and sealed-off the hood edges. Figure 4.10 shows the relationship between the incremental drag force and the force produced by the dynamic pressure times the projected area of 944 Case 2. The projected area of 944 Case 2 was obtained from the manufacturer. A theoretical relationship of a Porsche 944 series is also shown in Figure 4.10 for comparison.

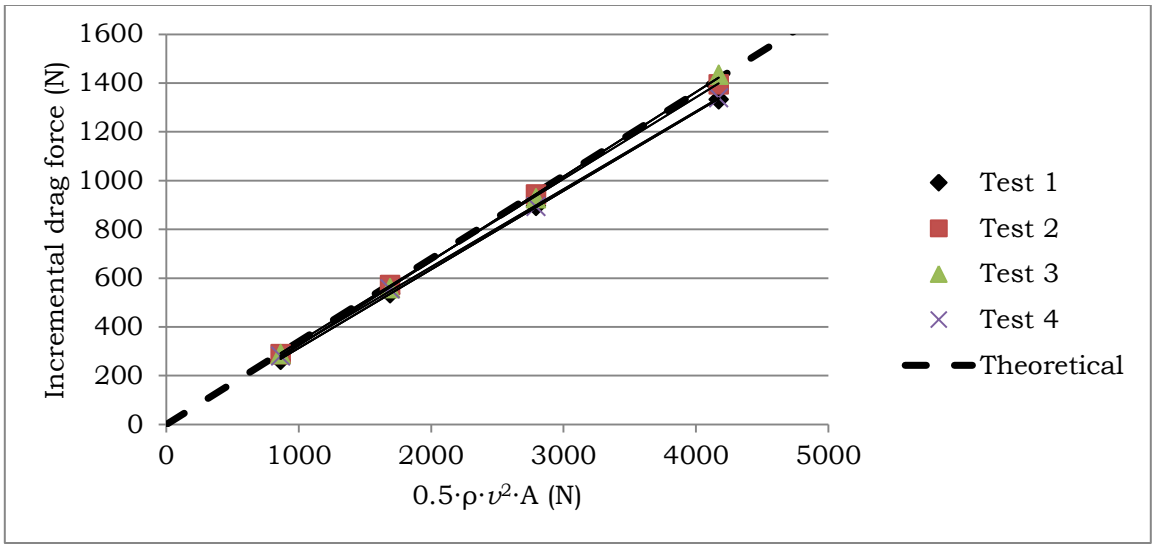

Figure 4.10: Plots of incremental drag force versus dynamic pressure ($0.5 \cdot \rho \cdot v^2$) and project area (A) of 944 Case 2

The average R^2 of the linear regression lines of the tests was found to be 1.0. The drag coefficients of the linear regression lines had a standard deviation of ±4% to the theoretical drag coefficient.

4.1.3.3: Summary

Aerodynamic improvement tests for 944 Case 2 initially measured low front and rear downforce. Through the installation of various aerodynamic devices the front and rear downforces increased and the drag force was maintained in only four tests. This will enhance the car's manoeuverability, efficiency and cornering speed. Figure 4.11 shows the summary of results of 944 Case 2 for 220 km/hr.

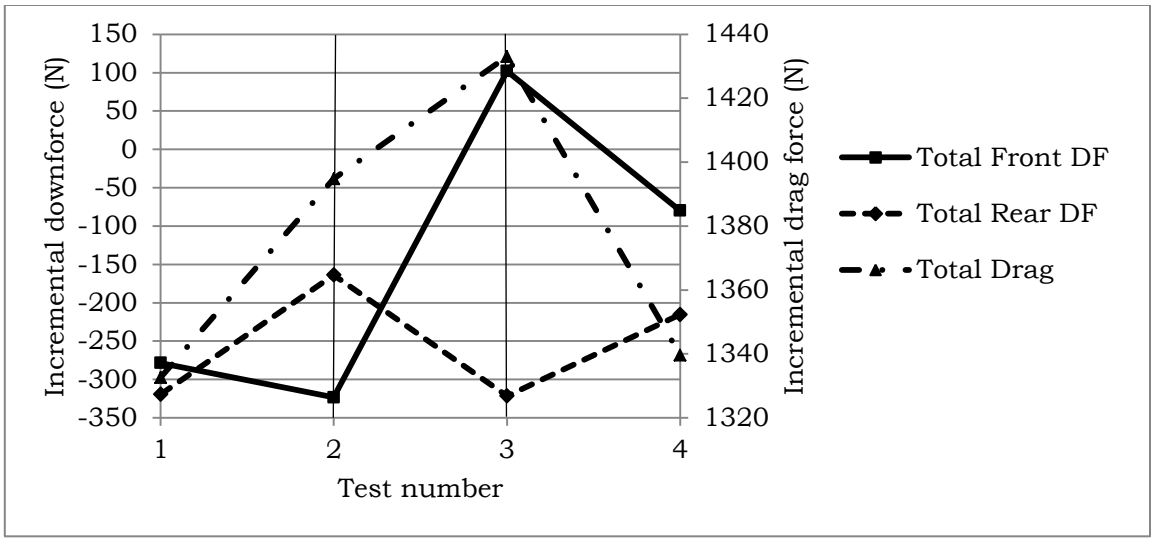

Figure 4.11: Improvement test incremental results for 944 Case 2 at 220 km/hr

The rear hatch wedge installation in Test 2 proved to increase rear downforce and drag force as shown in Figure 4.11. The front canards were attached in Test 3 but removed in Test 4. The front canards increased the drag force and increased the front downforce as shown in Figure 4.11. The rear and front downforces demonstrated opposite effects to one another.

4.1.4: Aerodynamic Force Improvement of Cayman Case 1

The aerodynamic force improvement tests for Cayman Case 1 are shown in Table 4.4. The objective of the test was to increase the incremental front and rear downforces for better manoeuverability and cornering speed. This was achieved using a front splitter extension, a gurney flap and a rear wedge. Pictures of some these devices are shown

in Appendix II. The baseline condition of the car had an attached high rear wing.

Table 4.4: Improvement tests for Cayman Case 1

Test	Car modification
1	Baseline (high rear wing)
2	Extended front splitter and one bolt size higher rear wing to Test 1
3	Placement of 1.5 cm rear wedge to Test 2
4	Installed 2 cm gurney flap to Test 3

Similar to the previous tests, speeds of 100, 140, 180, and 220 km/hr were used for each test. The improvement results for incremental front and rear downforce, and drag force are plotted separately.

4.1.4.1: Incremental Downforce Improvement Results

Figure 4.12 show the incremental front and rear downforce results of Cayman Case 1. The baseline results (Test 1 of Table 4.4) show a lower front downforce than the rear downforce. The high rear downforce was due to the high rear wing in the baseline setting.

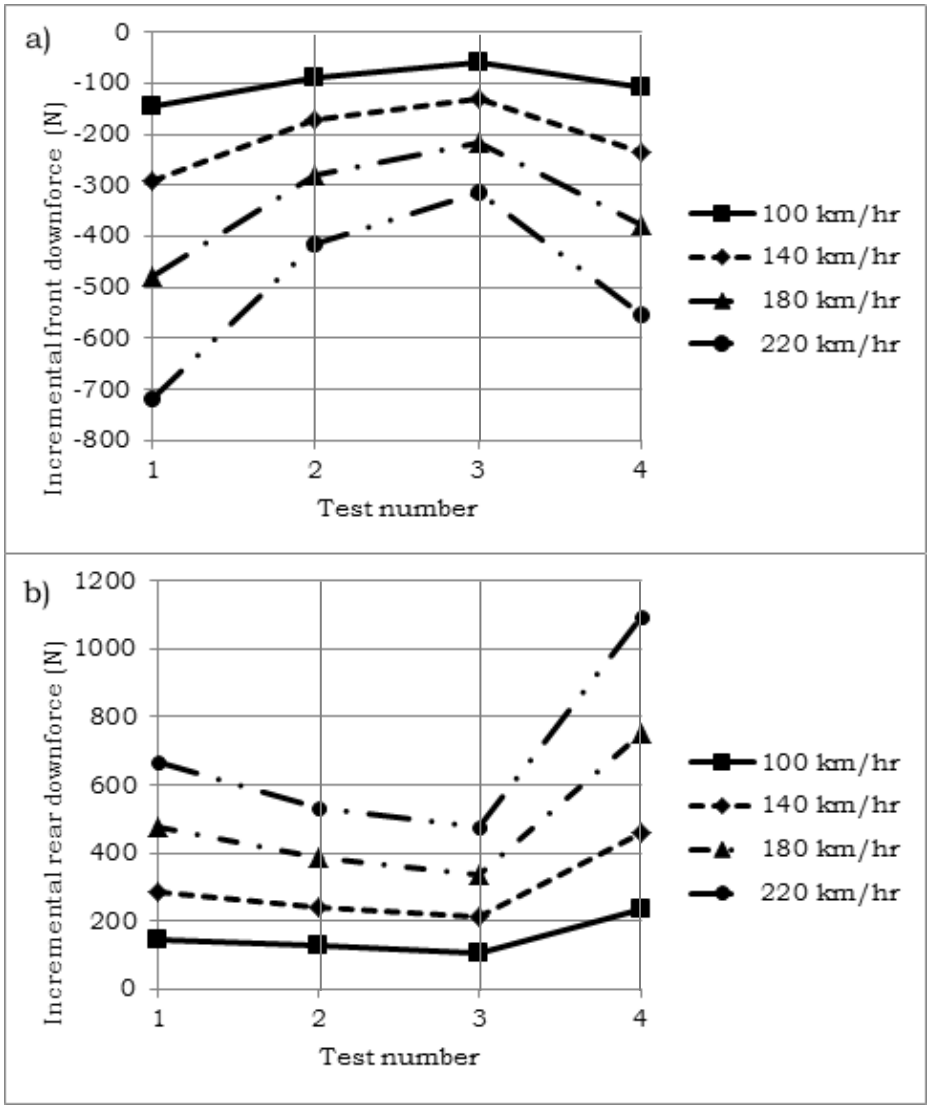

Figure 4.12: Incremental downforce improvement test results for Cayman Case 1 at 100, 140, 180 and 220 km/hr for (a) front downforce and (b) rear downforce

In Test 2 (Table 4.4) a front splitter extension was attached to increase the front downforce, also a higher rear wing angle of one bolt size was made to reduce the rear downforce decrease effect caused by the front splitter extension. These modifications managed to increase front downforce and reduce rear downforce as shown in Figure 4.12. The front downforce increase was due to the extension of the front splitter.

This produced a high pressure region over the extension and a low pressure region under the extension which increased the front downforce. The rear downforce decreased because the effect of the front canards was more significant than the effect of the higher rear wing angle on the rear downforce. A higher rear wing's angle of attack will modify the asymmetric flow around it which increases the pressure differential and produces rear downforce. A rear wedge was placed under the rear tires in Test 3. This was done to increase rear downforce without jeopardizing a lot of front downforce. The results instead showed an increase in the front downforce and a decrease in the rear downforce as shown in Figure 4.12. The increase of the front downforce was attributed to the extended front splitter being closer to the floor now that the rear is lifted (by the rear wedge). The closer the extended front splitter is to the floor the more constricted the air will be, which would increase the front downforce. The rear downforce decreased due to the chassis' rigidity. To increase the rear downforce, a gurney flap was attached to the rear wing's trialing edge on the high pressure side in Test 4. This dramatically increased the rear downforce and decreased the front downforce as shown in Figure 4.12. The increase in rear downforce was due to the gurney flap which produced an abrupt decrease in the flow's velocity. This increased the pressure on the rear wing which increased the rear downforce and in turn decreased the front downforce.

4.1.4.2: Incremental Drag Force Improvement Results

The drag improvement results obtained for Cayman Case 1 are shown in Figure 4.13. From the figure the drag force increased in Test 2. This was due to the front splitter extension which created a higher pressure region at the front of the car.

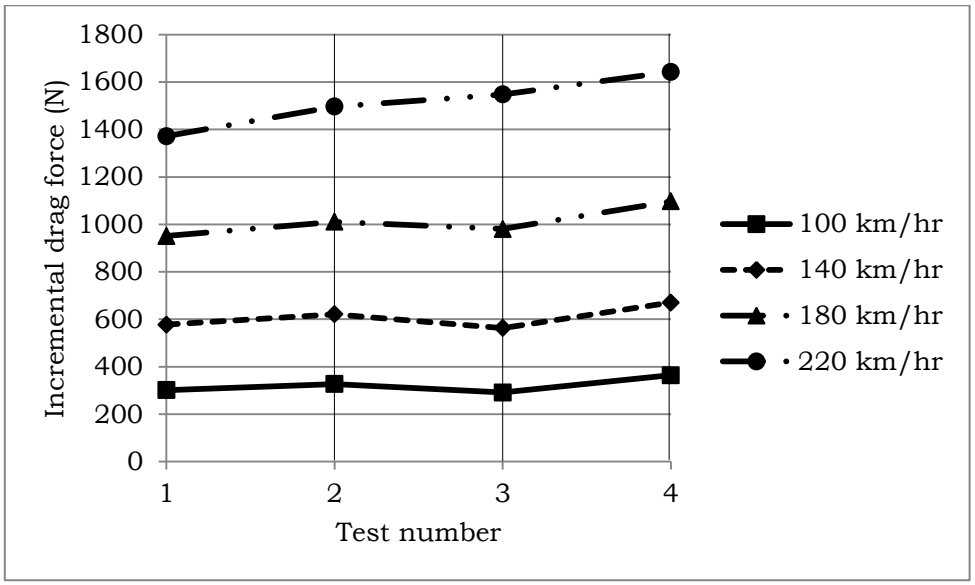

Figure 4.13: Incremental drag force improvement test results for Cayman Case 1 for speeds 100, 140, 180 and 220 km/hr

The placement of the rear wedge in Test 3 (Table 4.4) reduced drag for speeds 100, 140, and 180 km/hr and increased drag at 220 km/hr. This was due to the rear wedge creating a car angle susceptible to breakaway separation which is sensitive to speed. The attachment of the gurney flap in Test 4 increased the drag force. This was attributed to the gurney flap which produced a high pressure region and increased drag.

A plot showing the incremental drag force against the force produced by the dynamic pressure for all Cayman Case 1 tests are shown in Figure 4.14. A theoretical relationship for a Porsche Cayman series car is also plotted for comparison.

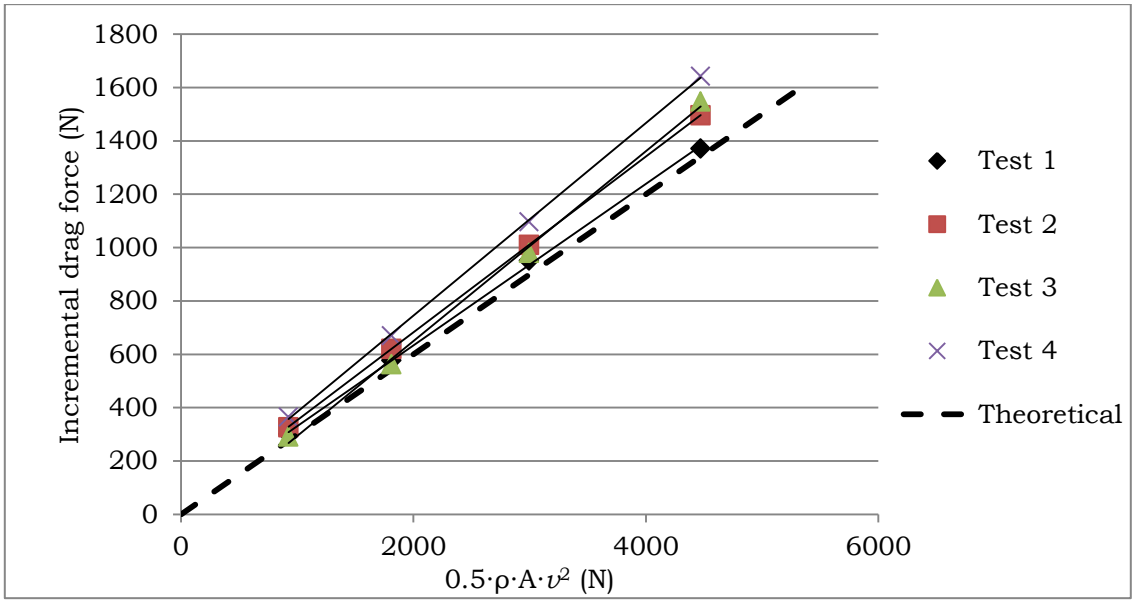

Figure 4.14: Plots of incremental drag force versus dynamic pressure ($0.5 \cdot \rho \cdot v^2$) and project area (A) of Cayman Case 1

The linear regression lines of the tests have an average R^2 of 1.0. The drag coefficients of the linear regression lines had a standard deviation of ±15% to the theoretical drag coefficient.

4.1.4.3: Summary

The aerodynamic improvement test of Cayman Case 1 increased front and rear downforce from the baseline condition as shown in Figure 4.15. This would improve the car's manoeuverability and cornering

speed. The improvement test proved that the front splitter extension increased front downforce and drag force. The improvement test also showed that the gurney flap was an effective device to increase rear downforce and drag force. The effect of the rear wedge on the drag force was shown to be speed dependant therefore caution should be taken when placing it.

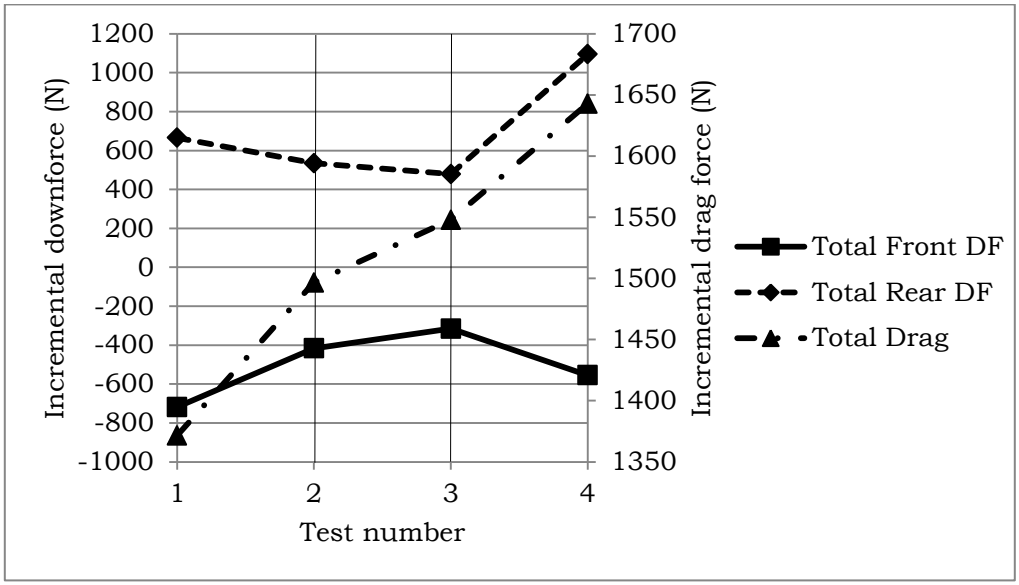

Figure 4.15: Improvement test incremental results for Cayman Case 1 at 220 km/hr

4.1.5: Aerodynamic Force Improvement of Cayman Case 2

Table 4.5 shows the aerodynamic force improvement tests for Cayman Case 2. The objective of the test was to increase the rear downforce for faster cornering speed without jeopardizing front downforce. Rear wedges, a gurney flap, and a rear wing were the

aerodynamic devices used. Pictures of some these devices are shown in Appendix II. The baseline configuration of the car had an extended front splitter and a low rear wing.

Table 4.5: Improvement tests for Cayman Case 2

Test	Car modification
1	Baseline (extended front splitter and low rear wing)
2	Placement of 1.5 cm rear wedge to Test 1
3	Installed 2 cm gurney flap to Test 2
4	Another 1.5 cm rear wedge (3 cm) was placed to Test 3

Speeds of 100, 140, 180, and 220 km/hr were used for each test. Incremental rear downforce, front downforce and drag force were plotted separately.

4.1.5.1: Incremental Downforce Improvement Results

The incremental front and rear downforce improvement test results of Cayman Case 2 are shown in Figure 4.16 (a) and (b) respectively. The baseline results (Test 1 of Table 4.5) show a lower front downforce than the rear downforce.

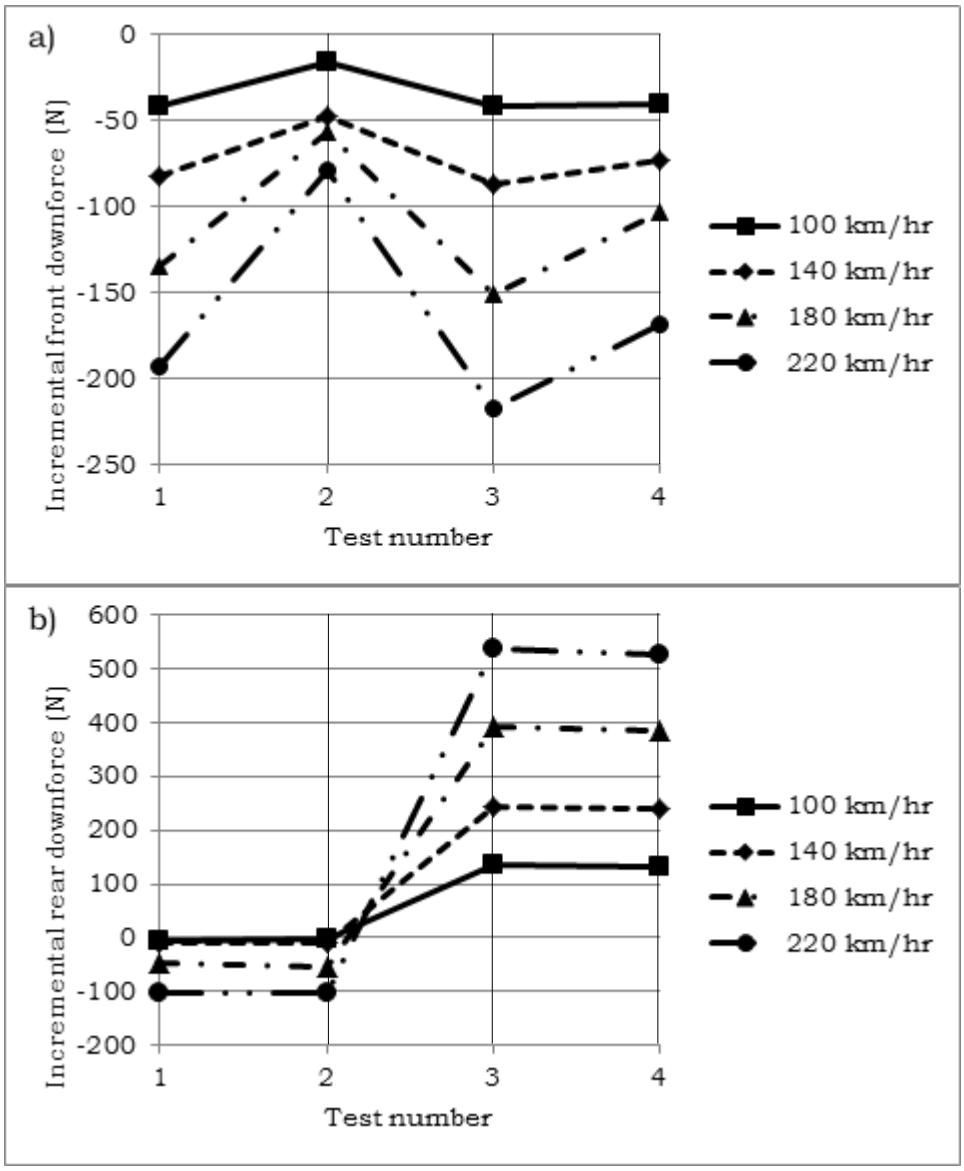

Figure 4.16: Incremental downforce improvement test results for Cayman Case 2 at 100, 140, 180 and 220 km/hr for (a) front downforce and (b) rear downforce

In attempt to increase the front downforce a rear wedge was placed under the rear tires in Test 2 (Table 4.5). The results show that the front downforce increased with unchanged rear downforce as shown in Figure 4.16. The increase in front downforce was expected from the insight of the improvement of Cayman Case 1. There was no effect at the rear downforce because the rear downforce produced by the increase in the angle of attack of the car was compensated by the rear downforce decrease caused by the rear wedge. To increase the rear downforce in Test 3 a gurney flap was attached to the low rear wing. This dramatically increased the rear downforce and decreased the front downforce as shown in Figure 4.16. The increase in rear downforce from the gurney flap installation was expected from Cayman Case 1. To increase the front downforce and maintain the rear downforce another rear wedge was placed under the rear tires for Test 4. This increased the front downforce and slightly decreased rear downforce as shown in Figure 4.16. The increase in front downforce was due to the sharper constriction of the air under the car. This produced a lower pressure region which increased the front downforce.

4.1.5.2: Incremental Drag Force Improvement Results

Figure 4.17 shows the drag improvement results obtained for Cayman Case 2. In Test 2 (Table 4.5) a rear wedge was placed under the rear tires. This produced insignificant effects in the drag force for speeds

100, 140, and 180 km/hr, however it increased the drag force at 220 km/hr as explained earlier.

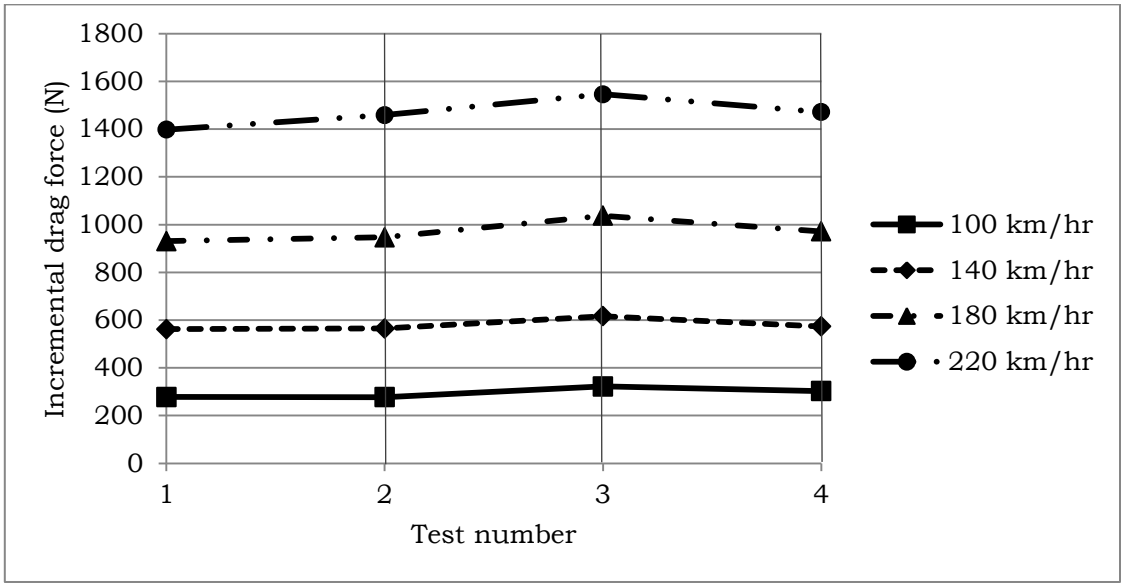

Figure 4.17: Incremental drag force improvement test results for Cayman Case 2 for speeds 100, 140, 180 and 220 km/hr

In Test 3 a gurney flap was attached which increased the drag as shown in Figure 4.17 for the reasons explain in Cayman Case 1. Another rear wedge was placed in Test 4 which decreased the drag force as shown in Figure 4.17. A plot showing the incremental drag force against the force produced by the dynamic pressure for all Cayman Case 2 tests are shown in Figure 4.18. A theoretical relationship for a Porsche Cayman series is also plotted for comparison.

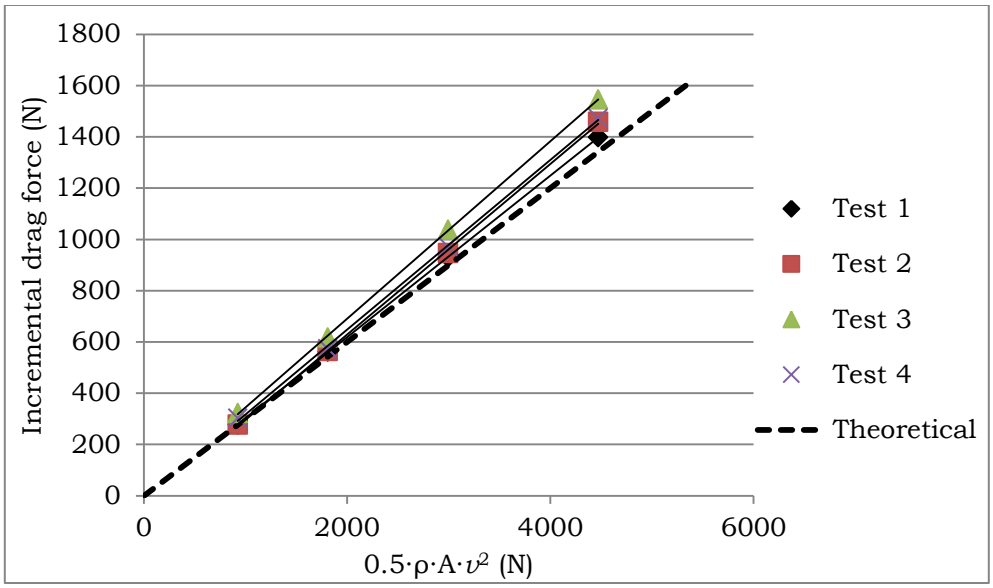

Figure 4.18: Plots of incremental drag force versus dynamic pressure ($0.5 \cdot \rho \cdot v^2$) and project area (A) of Cayman Case 2

The linear regression lines of the tests have an average R^2 of 1.0. The drag coefficients of the linear regression lines had a standard deviation of ±11% to the theoretical drag coefficient.

4.1.5.3: Summary

The aerodynamic improvement test of Cayman Case 2 managed to increase the rear downforce, without jeopardizing front downforce, from the baseline condition as shown in Figure 4.19. This will improve the car's cornering speed. The improvement test proved that placing a rear wedge to a front splitter extension modification increased the front downforce. In addition the rear wedge's effect on the drag force was shown to be speed dependent therefore caution should be taken when

placing it. The tests also showed that the gurney flap increased rear downforce.

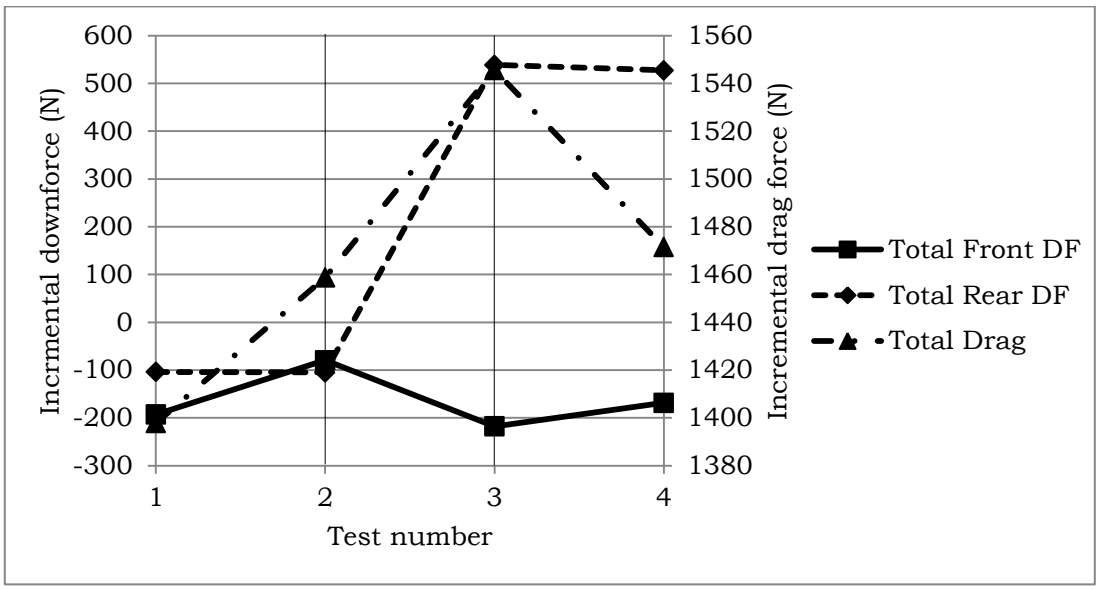

Figure 4.19: Improvement test incremental results for Cayman Case 2 at 220 km/hr

4.2: Flow Visualization

Tufts were used for the flow visualization study. The purpose of the flow visualization was to investigate the underbody air flow and the effect of yaw on the upperbody flow. Figure 4.20 shows a video snapshot of the tufts on the underbody of the car. During the tests the wind speed was 160 km/hr at 0˚ and 7.5˚ yaw.

Figure 4.20: Tufts on the underbody of 944 Case 1 at 160 km/hr and 0˚ yaw

From the video it was observed that the tufts tended to flutter a lot. For that reason the videos were observed for a period of 4 to 10 seconds, and the direction estimates of the tufts were obtained as shown in Figure 4.22 to Figure 4.26, Figure 4.28 to Figure 4.29, and Figure 4.31. All the tufts attached on the car body were observed, each arrow represents 1 to 4 tufts depending on their direction uniformity. This process aids to visualize the average representation of the air flow. It was assumed that for 0˚ yaw the upperbody flow of the car was symmetrical therefore tufts were only attached on the left-half side of the car. In some areas however it was observed that the tuft flutter was excessive, as shown in Figure 4.21. When the flutter of the tufts is considerably high such that the direction could not be determined then the area is considered turbulent. Turbulence is formed by the disruption of smooth,

laminar air flow by a sudden change of pressure, velocity or geometry of the surface. Turbulence directly affects aerodynamics therefore this will aid in determining the possible enhancement areas to improve the car aerodynamically. The turbulent areas are identified in green from Figure 4.22 to Figure 4.25.

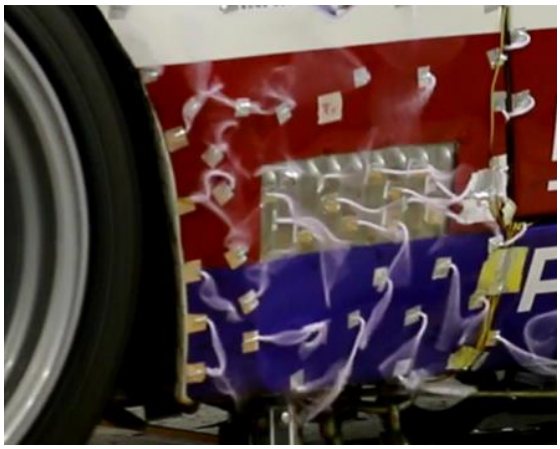

Figure 4.21: Tufts on the downwind of the front left tire of 944 Case 1 at 160 km/hr and 0˚ yaw.

4.2.1: Upperbody Analysis

The recorded front, side, and rear camera angles for 0˚ yaw are shown in Figure 4.22, Figure 4.23 and Figure 4.24 respectively. Figure 4.25 shows the side angle of the car in the 7.5˚ yaw position.

Figure 4.22: Flow visualization of the left side of 944 Case 1 in 160 km/hr wind and 0˚ yaw. Green regions indicate turbulent areas.

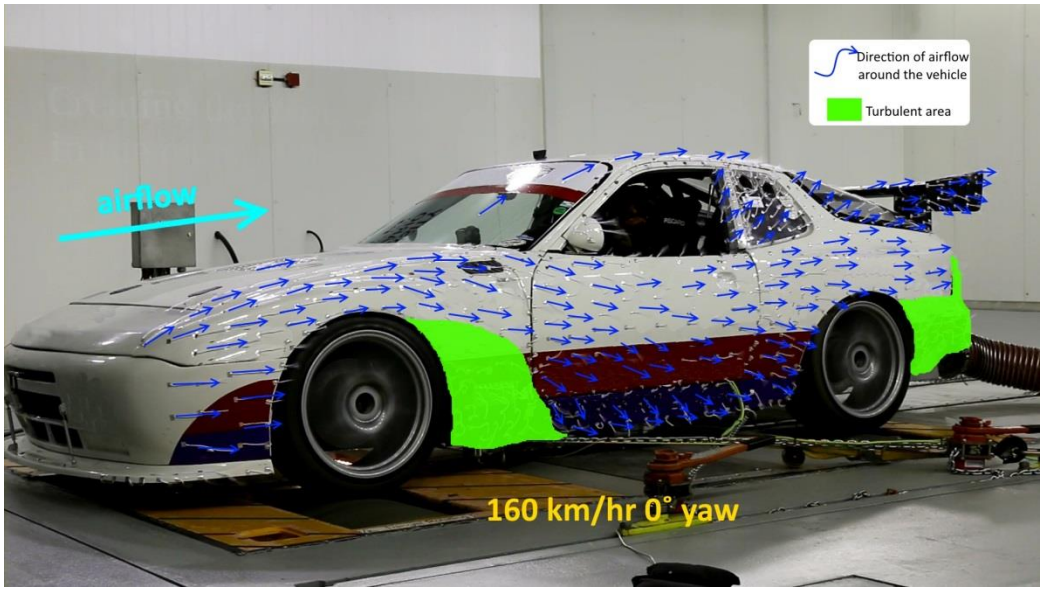

Figure 4.23: Flow visualization of the front left side of 944 Case 1 in 160 km/hr wind and 0˚ yaw. Green regions indicate turbulent areas.

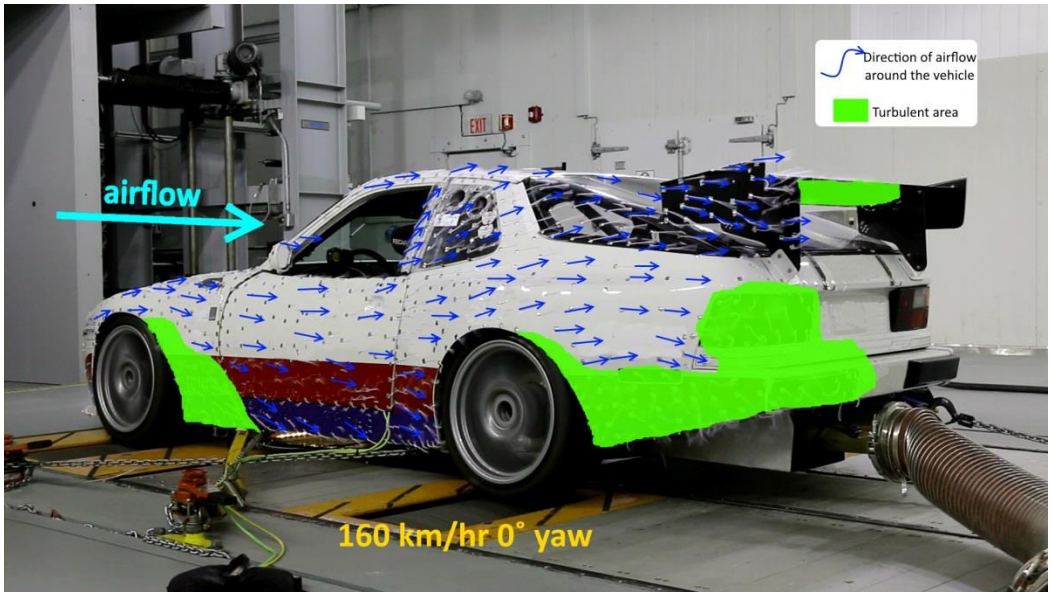

Figure 4.24: Flow visualization of the rear left side of 944 Case 1 in 160 km/hr wind and 0˚ yaw. Green regions indicate turbulent areas.

Figure 4.25: Flow visualization of the left side of 944 Case 1 in 160 km/hr wind and 7.5˚ yaw. Green regions indicate turbulent areas.

The side view of 944 Case 1 is shown in Figure 4.22 at 160 km/hr and 0˚ yaw. It can be stated that the tuft directions are consistent with the car's local geometry. Protruding surfaces like the tire wells force air around them. Figure 4.23 displays the front left side of the car at 160 km/hr and 0˚ yaw. The turbulent region downwind of the front tire well is independent of the attached chains. Although the chains do distort the air flow they do not affect the turbulent region in this case because they were attached behind the turbulent region. Figure 4.24 displays a hidden turbulent region which is below the rear wing. When a surface is curved the air flow has to bend and manoeuver quickly to follow the surface. For sharp curves, the flow cannot follow the bend resulting in flow separation from the surface, which creates recirculation and turbulent regions. This is the case with the rear bumper area in Figure 4.24. It is also observed from Figure 4.24 that the ends of the tufts placed on the rear wing of the car have become separated.

The tufts on the roof of the car show a flow separation close to the middle of the roof and an immediate reattachment, this is clearly shown in Figure 4.26. The immediate reattachment is attributed to the smooth and gradual hood surface slope.

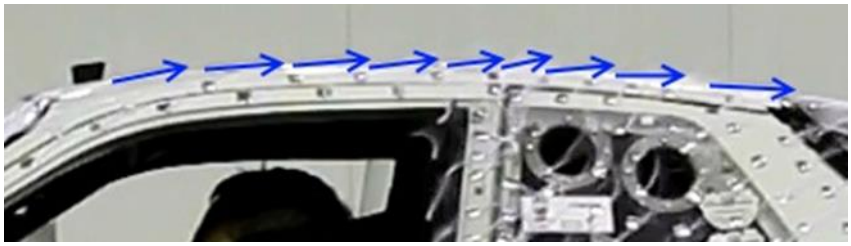

Figure 4.26: The tuft pattern on the roof of 944 Case 1 at 160 km/hr and 0˚ yaw

It was also observed that the tufts on the edge of the left car door on the lower portion of car (yellow window in Figure 4.27) are all sucked in the car. This indicates a low pressure region in the lower portion of the car. The direction of air flow around the rear tire pressure and differential cooling ducts (red window in Figure 4.27) was required. It was observed that the tufts were pointing out of the ducts indicating that the air is flowing out of them. This means that the air at the underside and around the rear tire and differential is at a high pressure. Allowing the build-up of air from the underside of the car to escape through the ducts reduces the pressure build-up under the car and may improve downforce.

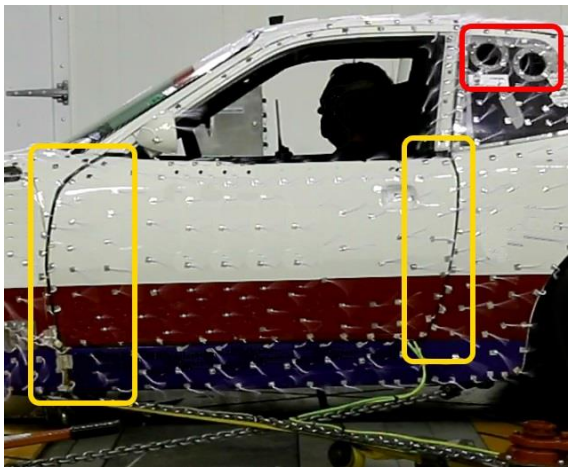

Figure 4.27: A close up of the side of 944 Case 1. Yellow windows show the tufts on the edges of the side door that are sucked in. Red window shows the tuft patterns around the rear tire pressure and differential cooling ducts.

Figure 4.25 shows the tuft behaviour of 944 Case 1 in a 7.5˚ yaw. When comparing the tuft flow directions of the 0˚ yaw condition (Figure 4.23) to the 7.5˚ yaw (Figure 4.25) it is evident that the car yaw has straightened out the side flow. It is also evident from both figures that although local geometry plays a role on the flow direction, in the yaw condition, it is not as influencing as the 0˚ yaw condition. This is attributed to the increased left surface exposure of the car to the wind, which excites the tufts and makes them more consistent with the air flow direction. Also, clear differences in turbulent regions can be observed between the 0˚ yaw (Figure 4.23) and the 7.5˚ yaw (Figure 4.25). In the 7.5˚ yaw condition the turbulent regions are much smaller

than in the 0˚ yaw condition. This is attributed to the left side exposure of the car to the wind due to the yaw.

The upperbody flow visualization revealed that when the car is in yaw, the exposed surface is less influenced by local geometry and more by the air flow direction. It also showed that flow separation points are recoverable for smooth gradual slope surfaces like the car hood. It was demonstrated that hidden surfaces of the car cause flow separation and turbulent regions.

4.2.2: Underbody Analysis

Figure 4.28 shows the direction estimates of the tufts placed on the underbody of 944 Case 1. The dashed rectangular box in the figure shows the position of the tufts that were attached on the differential and air disperser plate under the diffuser.

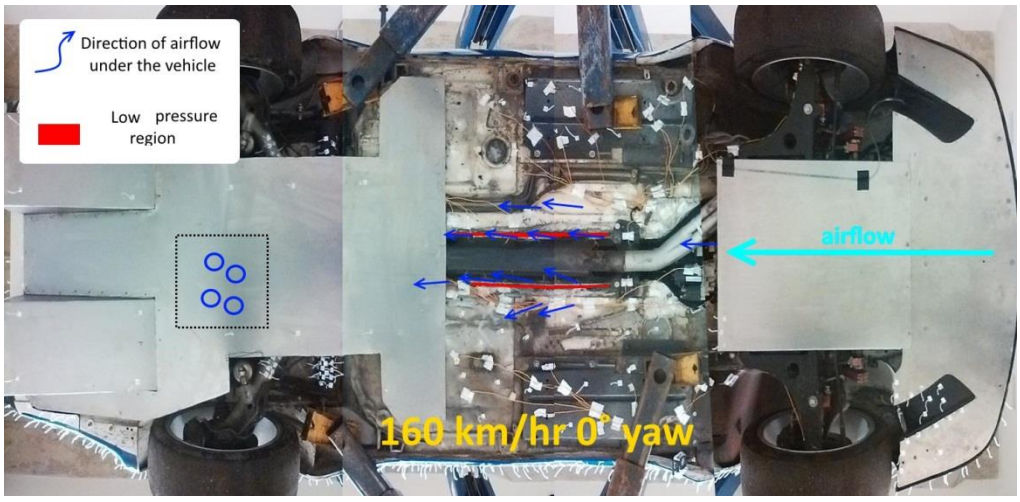

Figure 4.28: Underbody of the car showing the airflow direction of the tufts at 160 km/hr and 0˚ yaw

The underbody of the car was captured only for 0˚ yaw. The directions of the underbody tufts are depicted by blue arrows in Figure 4.28. The results show that there is no turbulent region because the tufts were not flailing. Occasionally, however, the tufts were drawn into the narrow region indicated by the red line in Figure 4.28. This region is the space the exhaust cover (right above the exhaust pipe) makes with the chassis. This region is considered a low pressure region as it was observed that the tufts tend to get sucked into it. This is attributed to its narrow width which constricts the air through it to increase its velocity.

In addition, tufts were placed at the edge of the front plate to determine if there is a low pressure region above the front plate. Note that a low pressure region above the front plate should suck the tufts at the edge. It was observed from Figure 4.28 however that the pattern shown by the tufts on the edge of the plate was consistent with the airflow. This means that a low pressure region does not exist above the front diffuser plate. A close up of the underbody exhaust pipe region tufts is shown in Figure 4.29 for a better visualization.

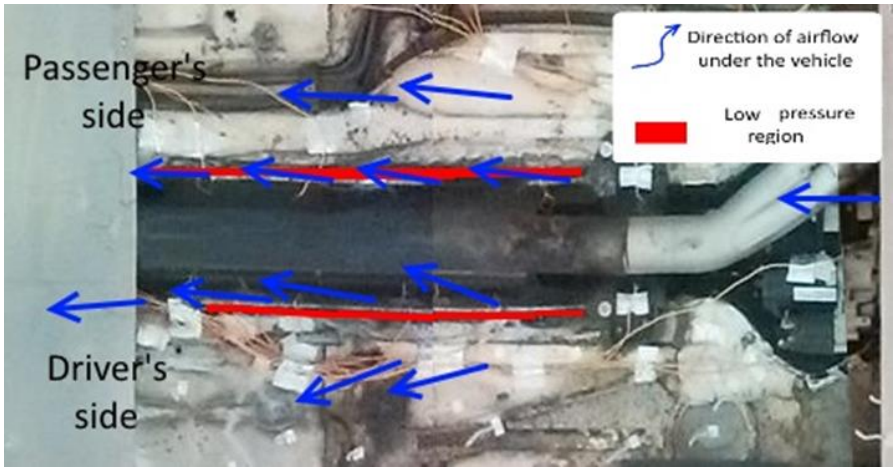

Figure 4.29: A close up of the exhaust pipe region in Figure 4.28

From Figure 4.29 it can be observed that the direction of the tufts on the passenger side of the car follow a fairly consistent pattern with the direction of the air flow. However there is a slight drift of a few tufts towards the passenger side which can be attributed to underbody local geometry effects. On the contrary the directions of the tufts on the driver's side are relatively different from the airflow direction. Tufts on the driver's side that are closer to the exhaust pipe tend to point towards the passenger's side and then gradually change direction along the downwind of the exhaust until the tufts point towards the driver's side.

From the tuft patterns shown in Figure 4.29 it can be assumed that there exists a spiral flow effect around the exhaust pipe shown in Figure 4.30. Furthermore, the two tufts further away from the exhaust pipe on the driver's side in Figure 4.29 show air flow towards the driver's side. This effect can be attributed to the underbody local geometry.

Figure 4.30: Spiral flow effect assumed around the underbody exhaust pipe

The air flow direction on the differential was investigated. This was done to understand if the half shaft boot (shown in Figure 4.31) was getting blown off from deflected air from the differential. The air flow direction on the air disperser plate was also investigated. This was done to understand how it stopped the half shaft boot from getting blown off and where it was deflecting air to. Figure 4.31 shows the underbody differential and air disperser plate with their estimated tuft directions.

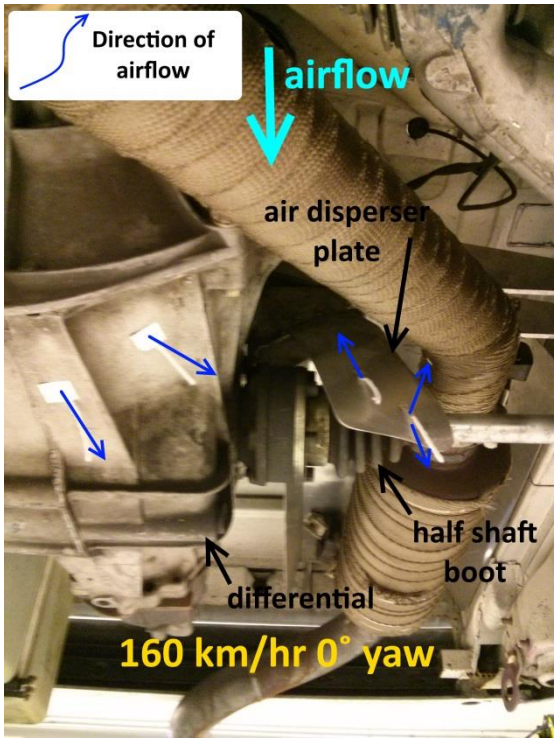

Figure 4.31: Tuft directions on the car's differential and air disperser plate showing the flow direction

As shown in Figure 4.31 the direction of air flow on the differential follows the conical geometry of the component. The tuft directions on the differential show the air being deflected onto the half shaft boot. This explains why the half shaft boot was being blown off. The tufts on the air disperser plate show air flow away from the leading edge of the plate. The plate therefore deflects incoming air away from the half boot shaft to the insulated exhaust pipe. Although the air disperser plate does not deflect air from the differential, the plate's position disrupts the deflected air from the differential which keeps the half shaft boot in place.

Underbody flow visualization shows that local geometry has a significant contribution to the flow direction. This is consistent with Khasow et al. (2015) who observed that the underbody aerodynamics is dominated by local underbody geometry. The underbody flow visualization also showed that there is a spiral flow effect generated around the underbody exhaust pipe. The visualization test also showed that the underbody differential was deflecting air onto the half shaft boot which explained why it was blowing off. By installing an air disperser plate it avoided the half shaft boot from blowing off.

4.3: Temperature Analysis

Temperature data was obtained for upperbody, underbody, and brake proximity locations while the car was operating on the facility's dynamometer. During testing the ambient air temperature of the wind tunnel was kept at 26˚C but fluctuated between 25˚C and 29˚C.

4.3.1: Upperbody Analysis

The temperatures of selected upper body locations were measured to study the effect of yaw on the radiator performance, lower louver, upper grill, and hood louver temperatures. In addition the effect of yaw and the rear underbody diffuser on the rear tire pressure duct and the differential cooling duct temperatures were investigated. The locations of the upperbody thermocouples are shown in Figure 4.32 and Figure 4.33.

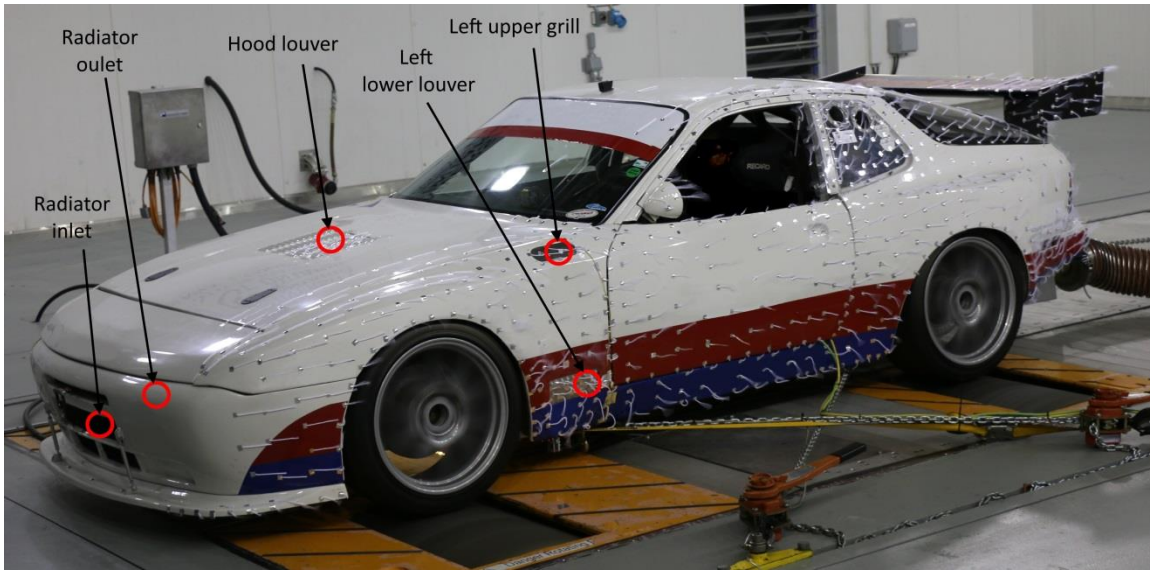

Figure 4.32: Thermocouple locations on 944 Case 1 (left side)

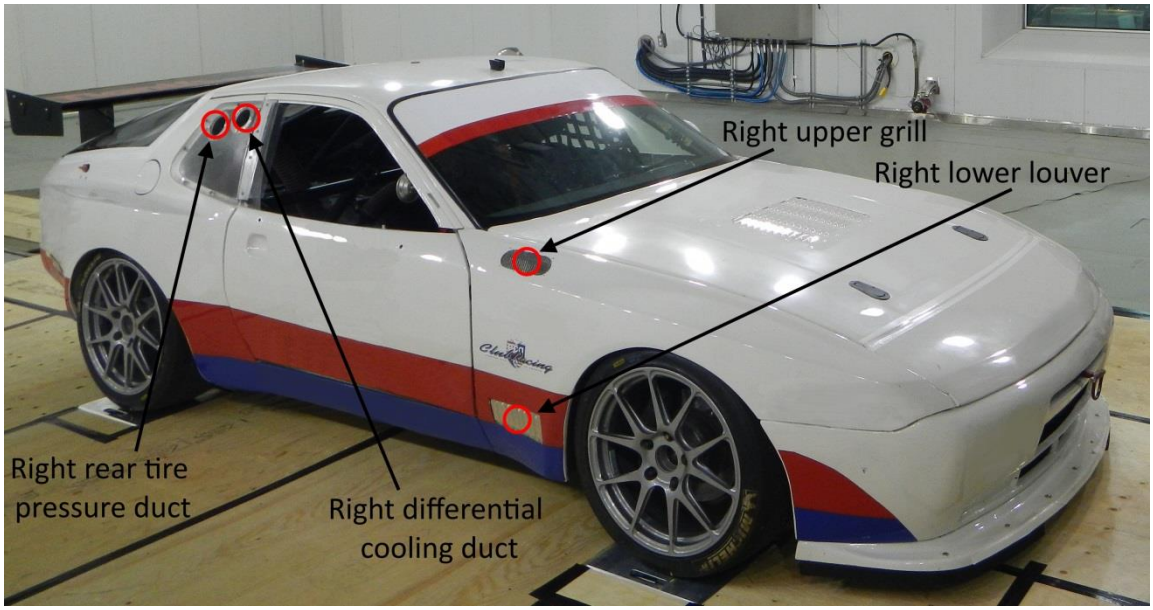

Figure 4.33: Thermocouple locations on 944 Case 1 (right side)

Figure 4.34 shows the temperature profiles for the left upper grill (see Figure 4.32) for Test 1 to Test 9 (Table 3.5). The left upper grill thermocouple was chosen to compare the temperature profiles because it showed the slowest progression toward a steady state. This was because the thermocouple's position was the farthest away from a heat source (tires). The left upper grill was particularly chosen because its temperature readings had less fluctuations than the right upper grill.

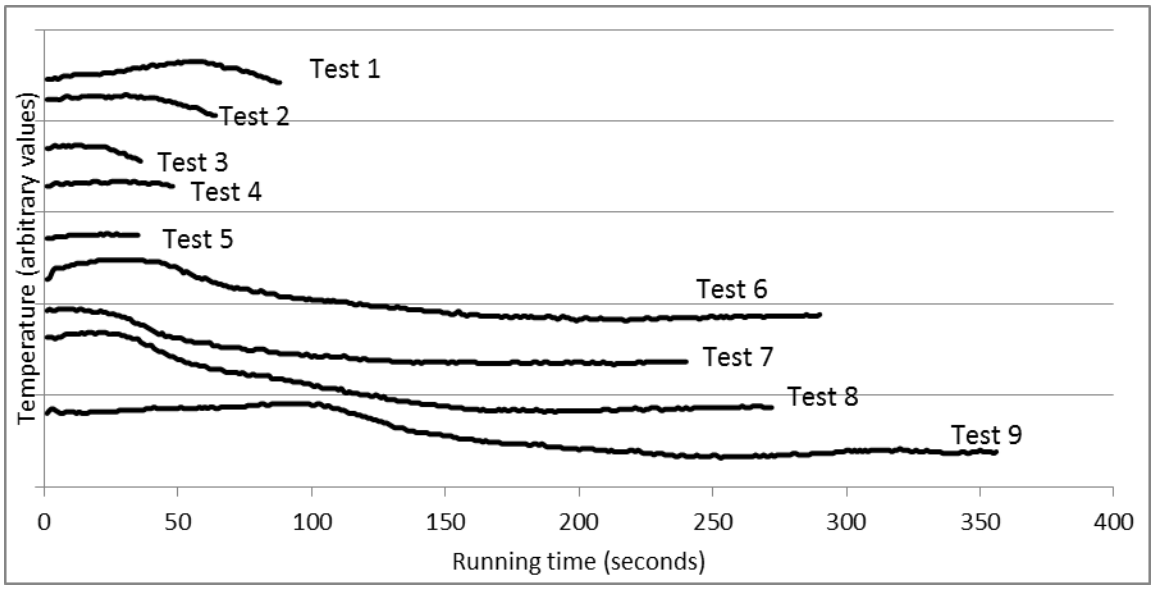

Figure 4.34: Temperature profiles of the left upper grill for Test 1 to 9 on the 944 Case 1

The temperature profiles in Figure 4.34 show that not all the thermocouples reached a steady state. This was attributed to the different test durations. The longer the test duration the more likely steady state conditions will be reached. Test 1 to Test 5 did not have

sufficient time to reach steady state, however, Test 6 to Test 9 did. Therefore, only Tests 6 to 9 are reported in the upperbody analysis. Table 4.6 shows the temperature ranges for Tests 6 to 9. The bold temperature ranges show the different measurements of the thermocouples. The different thermocouple measurements were put in bold to distinguish them from the remaining results.

Table 4.6: Upperbody temperature ranges measured for Tests 6 to 9

				Radiator		Left side		Right side	
	Rear tire pressure duct (˚C)	Differential cooling duct (˚C)	Hood louver (˚C)	Inlet (˚C)	Outlet (˚C)	Lower louver (˚C)	Upper grill (˚C)	Lower louver (˚C)	Upper grill (˚C)
Test 6	30-40	40-50	30-40	20-30	60-70	20-30	20-30	20-30	20-30
Test 7	30-40	40-50	30-40	20-30	60-70	20-30	20-30	20-30	20-30
Test 8	30-40	**60-70**	30-40	20-30	60-70	**30-40**	20-30	**30-40**	20-30
Test 9	30-40	40-50	30-40	20-30	**40-50**	20-30	20-30	20-30	20-30

Tests 6 and 7 are identical because they have the same testing conditions and were conducted sequentially. The rear tire pressure duct temperatures were the same for all the tests and measured a temperature higher than the ambient temperature. The higher

temperature measurement was attributed to the heat generated by the rear tire's friction with the dynamometer roller. The higher temperature measured in the differential cooling duct of Test 8 was attributed to the insufficient cooling of the differential. As Tests 6, 7 and 8 are conducted while the rear underbody diffuser was attached, this prevented adequate cooling from taking place at the rear underbody, which was where the differential was placed. This therefore increased the temperature around the differential and translated into an increase in temperature at the differential cooling duct. The differential cooling duct temperatures are shown in Figure 4.35.

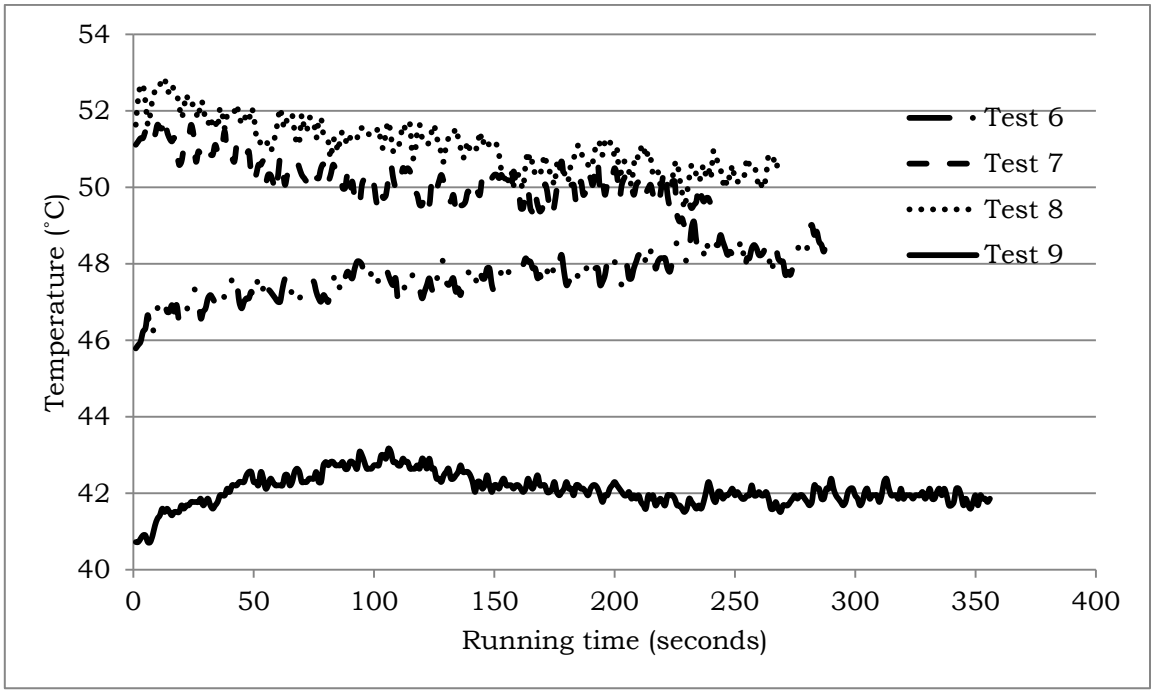

Figure 4.35: Differential cooling duct temperature of 944 Case 1 at 160 km/hr for Tests 6 (7.5˚ yaw with diffuser), 7 (7.5˚ yaw with diffuser), 8 (7.5˚ yaw with diffuser) and 9 (7.5˚ yaw without diffuser)

The differential cooling duct temperature of Test 9 in Figure 4.35 is much lower than Tests 6 to 8, this was attributed to the removal of the rear underbody diffuser. Removing the rear underbody diffuser increased the cooling effect around the differential, hence reduced the temperature at the differential cooling duct.

The hood louver temperature ranges from Table 4.6 for all the tests are the same. The temperatures are the same because yaw does not have an effect on the convection rate on the hood louver. This is because there are no obstructions upwind of the hood louver which would distort the air flow. The radiator inlet temperatures are the same for all the tests because the wind tunnel temperature was kept between 25˚C and 29 ˚C. Test 9 measured the lowest radiator outlet temperature. This was attributed to the increased air flow that entered the front car grill for cooling in 0˚ yaw. When the car was in yaw less air enters the car's front grill because of its reduced frontal area. It is evident from Table 4.6 that for all the tests, the lower louver and the upper grill on both sides of the car measured the same temperature range. As these openings vent air from downwind of the front tires of the car, it can be stated that there is symmetrical frontal underbody heat distribution regardless of yaw. Test 8 measured a higher lower louver temperature than Test 9 because it was conducted in 7.5˚ yaw where the tires are rolling on the dynamometer wheels at an angle to the air flow which would generate more heat from friction than at 0˚ yaw. Test 8 measured

a higher lower louver temperature than Tests 6 and 7 because the underbody convection rate in yaw is nonlinear. This was because the flow in this region is turbulent.

The upperbody temperature analysis shows that the lower louver and radiator outlet temperatures are dependent on yaw. The hood louver and upper grill temperatures however were consistent throughout the tests. It was also found that placing an underbody rear diffuser increased the differential cooling duct's temperature.

4.3.2: Underbody Analysis

Underbody temperatures were measured to study the effect of yaw on the heat distribution under the car. In addition the effect of the rear diffuser on the underbody surface temperatures was examined. Similar to the upperbody analysis, there was inadequate running time for some of the tests to reach steady state, therefore the temperature profile of Thermocouple 2-6 was plotted. Thermocouple 2-6 (Figure 4.36) was chosen because it showed the slowest temperature reading. This was done to distinguish the tests that have reached steady state from those that have not. The plot of the temperature profiles of Test 1 to 9 (Table 3.5) is shown in Figure 4.37. Thermocouple 2-6 showed the slowest temperature readings because it was both close to a heat source (exhaust header) and was the most affected by the air flow.

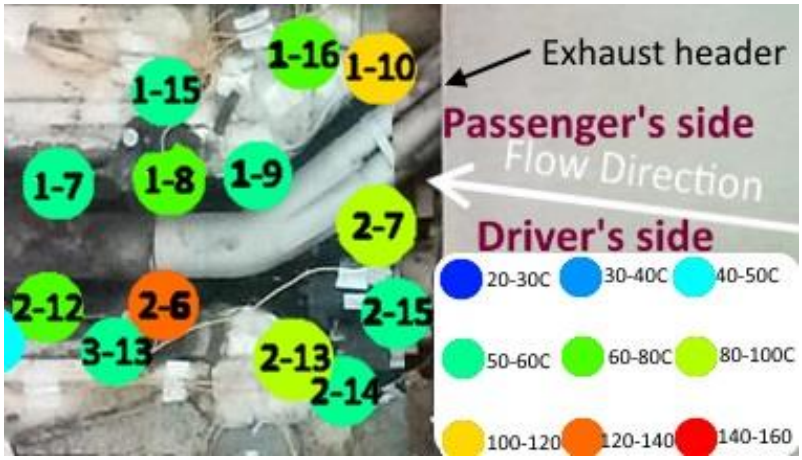

Figure 4.36: Temperature map of the underbody exhaust header in Test 6 (160 km/hr and 7.5˚ yaw)

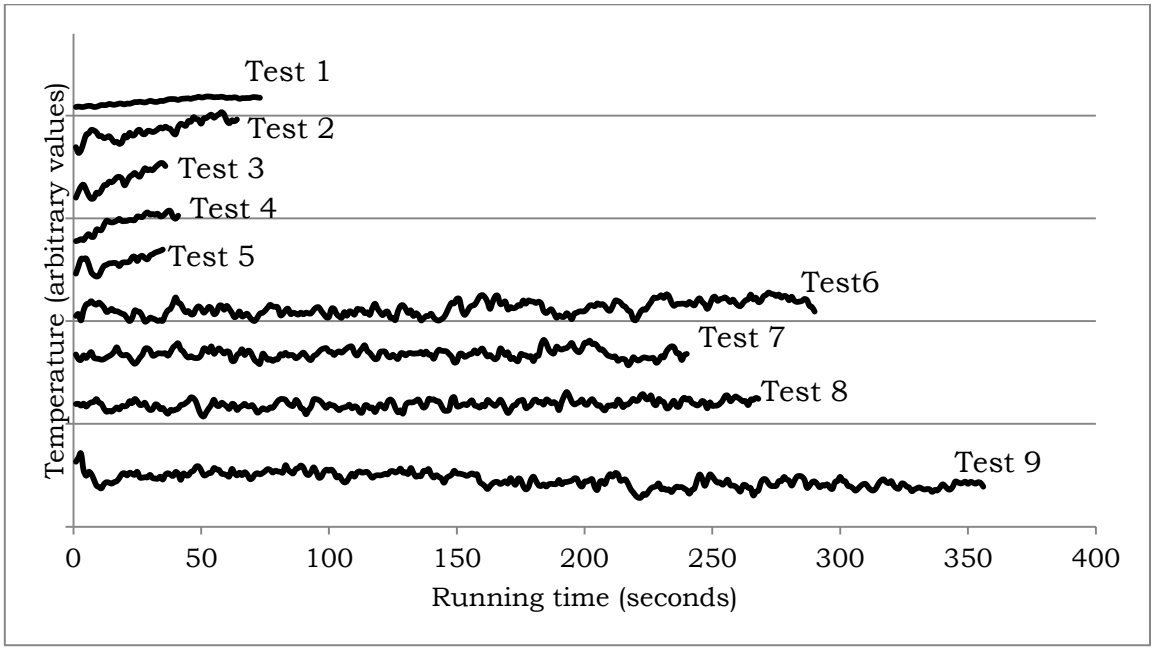

Figure 4.37: Temperature profiles of Thermocouple 2-6 of Tests 1-9 for 944 Case 1

Figure 4.37 shows that the temperature profiles in Tests 1 to 5 have not reached steady state as they were still increasing. Tests 6 to 9, however, reached steady state as their profiles have plateaued. Therefore, only Tests 6 to 9 are analysed for the underbody analysis as they show steady state conditions. Figure 4.38 shows the underbody temperature map of Test 9. Test 9 is the reference as it was the only test in 0˚ yaw to have reached steady state.

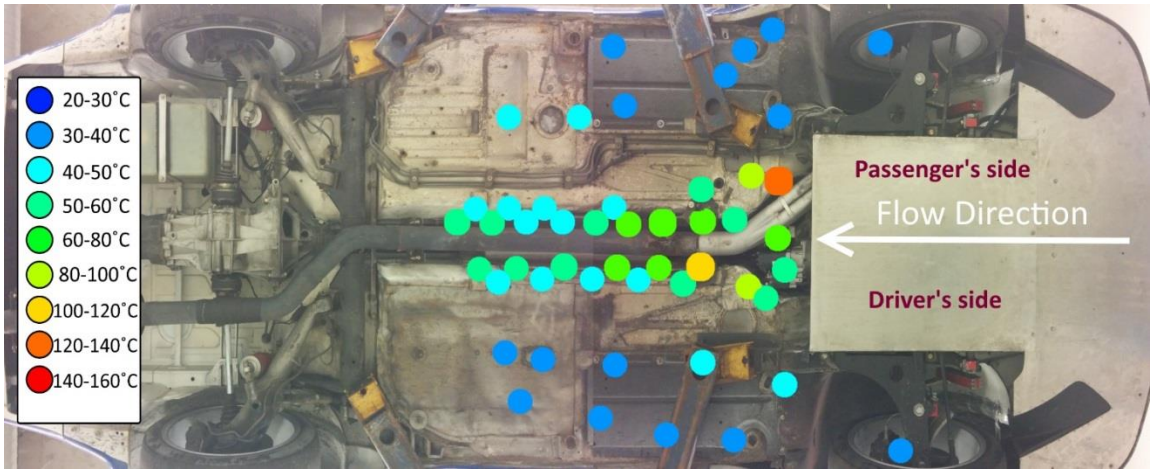

Figure 4.38: Underbody temperature map of Test 9 (0˚ yaw, without diffuser) for 944 Case 1

The thermocouples placed in the vicinity of the underbody exhaust pipe measured a higher temperature reading than those placed farther away from it. This was expected as the exhaust pipe directs combusted exhaust gas which is very hot. There are some thermocouples, in the proximity closest to the exhaust pipe, that do not have uniform temperatures. This was because the thermocouples are not equidistant

from the exhaust pipe. The thermocouples on the far driver's and passenger's side show similar temperature distribution. This was attributed to equally distributed underbody cooling in a 0˚ yaw condition. Although Test 9 was the only test at 0˚ yaw that reached steady state it was also the only test conducted without a diffuser. The temperature map for Test 6 (7.5˚ yaw, with diffuser) is shown in Figure 4.39.

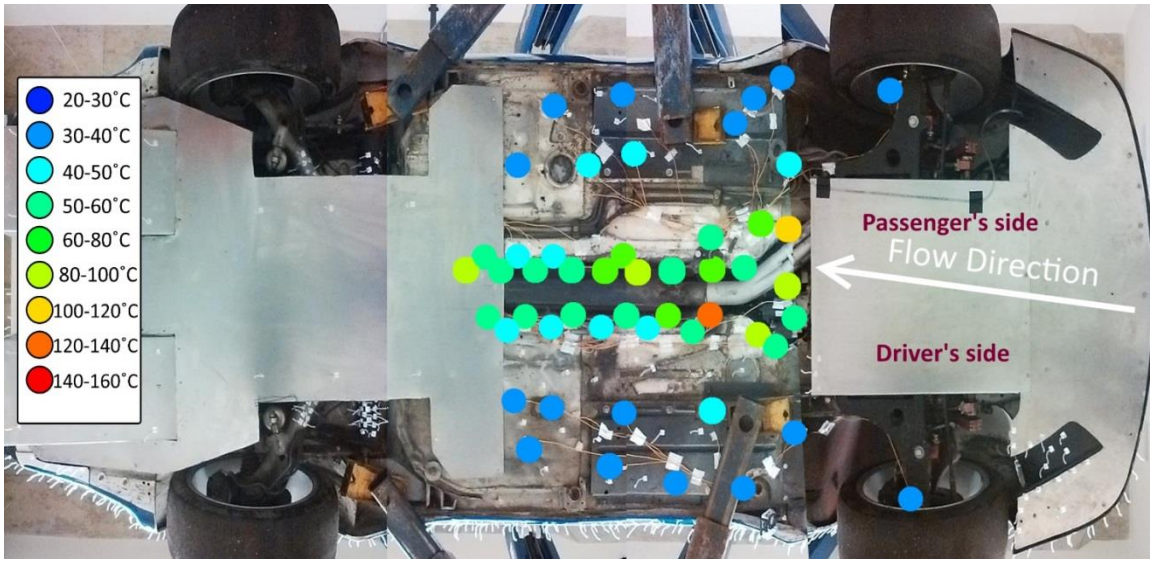

Figure 4.39: Underbody temperature map of Test 6 (7.5˚ yaw, with diffuser) for 944 Case 1

The thermocouples in Test 6 (Figure 4.39) that are placed on the far passenger's side measured higher temperature than those on the far driver's side. This was attributed to the air flow direction blowing hot air (by convection) towards the passenger side of the car. It is also evident from Test 6 (Figure 4.39) that 2 out of the 3 thermocouples covered by

the rear diffuser show higher temperature readings than in Test 9 (Figure 4.38). This was attributed to the rear diffuser reducing heat exchange due to reduced surface exposure. Underbody temperature map for Test 7 is shown in Figure 4.40.

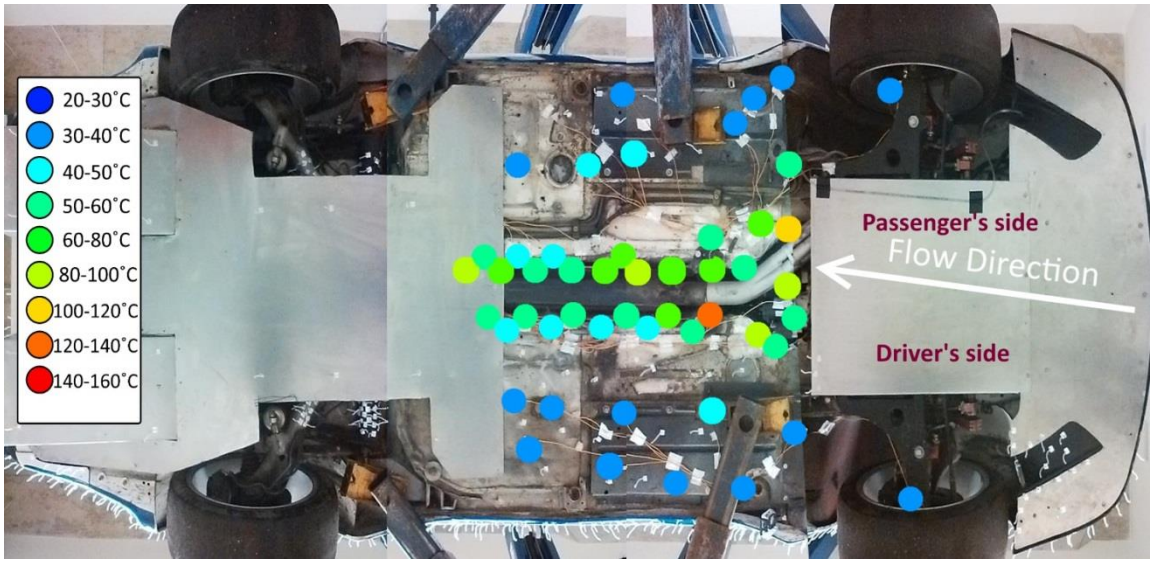

Figure 4.40: Underbody temperature map of Test 7 (7.5˚ yaw, with diffuser) for 944 Case 1

Test 7 (Figure 4.40) shows a very similar temperature map to Test 6 (Figure 4.39). This was because both tests were consecutive and have the same testing conditions. As Tests 6 and 7 are very similar to each other, only Tests 9, 6 and 8 will be compared to each other. The underbody temperature map for Test 8 is shown in Figure 4.41.

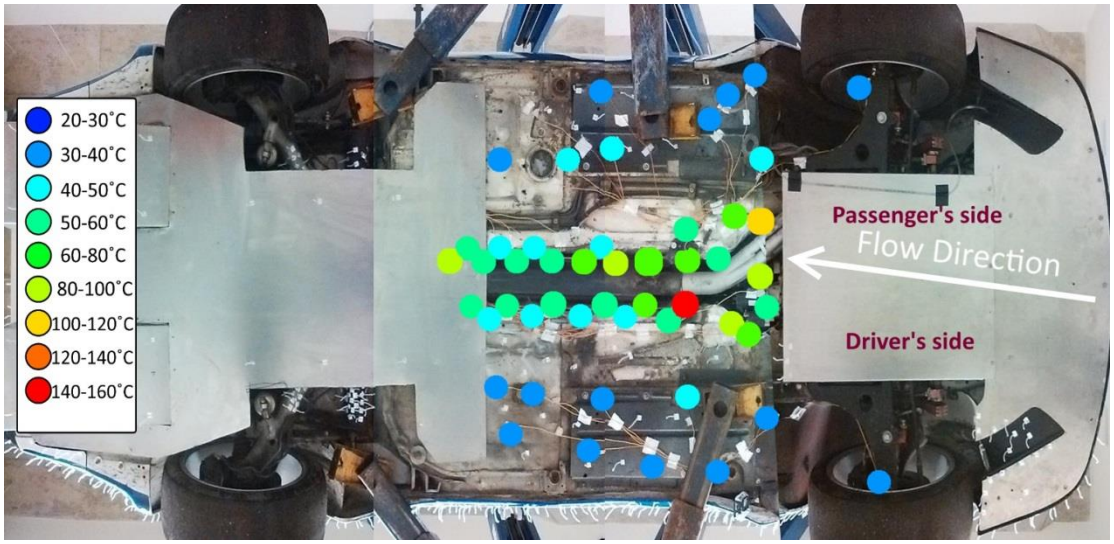

Figure 4.41: Underbody temperature map of Test 8 (7.5˚ yaw, with diffuser) for 944 Case 1

The most significant change between Tests 9, 6 and 8 is the red temperature range reading (Thermocouple 2-6) on the driver's side close to the exhaust pipe in Test 8 (Figure 4.41). Although the high temperature readings of some of the thermocouples in the proximity of the exhaust pipe were previously attributed to human (placement) error, car yaw might have an additional role in Thermocouple 2-6's reading in Test 8 (Figure 4.41). When the car was in yaw, the underbody flow was disturbed as the tires' position and rotation disperse air around it, this was assumed to have a negative effect on underbody cooling. In the aligned position (0˚ yaw) of Test 9 (Figure 4.38) Thermocouple 2-6 has a lower temperature reading than Tests 6 and 8. This was attributed to the aligned position of the car. When the car was aligned with the air flow

direction more effective cooling takes place which in turn decreased the temperature of underbody parts. More effective cooling takes place in an aligned position because cool fast air can flow undisturbed.

The underbody analysis shows that yaw did have an effect on the underbody heat distribution. It also shows that the rear diffuser had significant impact on the underbody cooling rate.

4.3.3: Brake Proximity Analysis

The effect of yaw on the brake performance was studied. Braking generates heat in the brake pads, and the amount of heat generated by either brake pads (left or right) is dependent on its brake load contribution. The data collected provides information on the temperature in the vicinity of the brakes. The thermocouples associated with measuring the temperature of the brakes were placed ahead of the brake pads as shown in Figure 4.42. The thermocouple was placed ahead of the brake pads because of placement convenience. Braking was deployed by the sit-in driver during the tests.

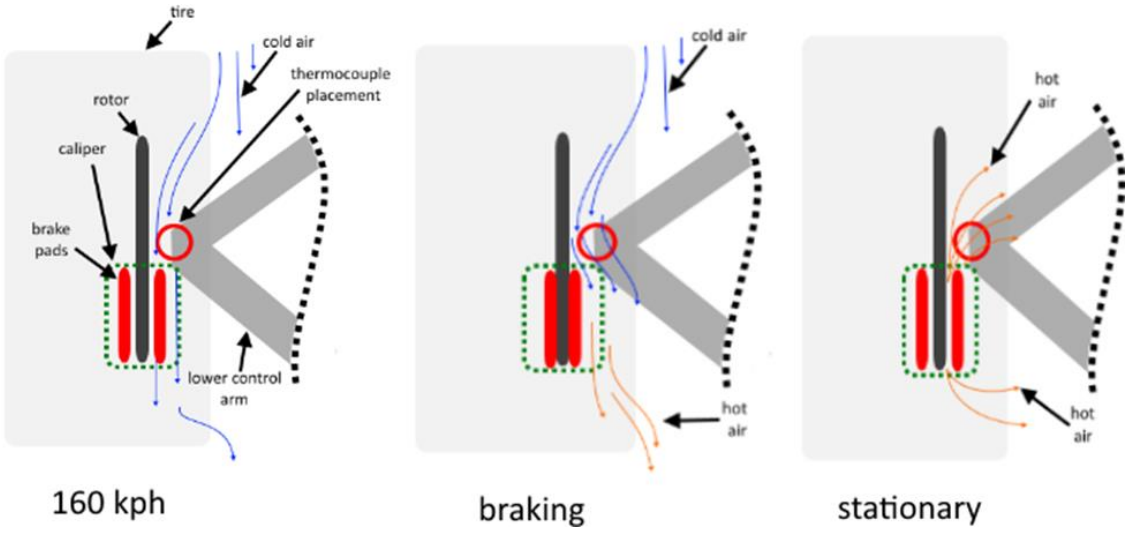

Figure 4.42: Presumed air flow of cold and hot air before, during and after braking

The brake temperature data obtained for Test 1 is displayed in Figure 4.43 and Figure 4.44. Figure 4.43 illustrates the temperature profile recorded by the thermocouple during braking, while Figure 4.44 displays the temperature profile after braking.

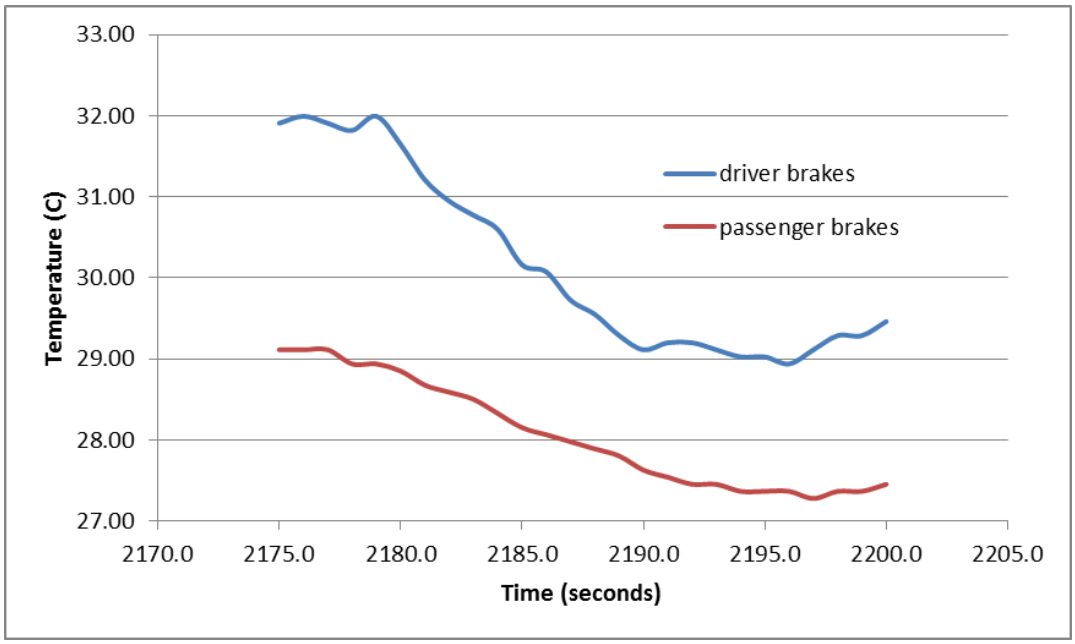

Figure 4.43: Temperature profile of the thermocouple in the vicinity of the brake pads during braking in Test 1 (160 km/hr and 0˚ yaw)

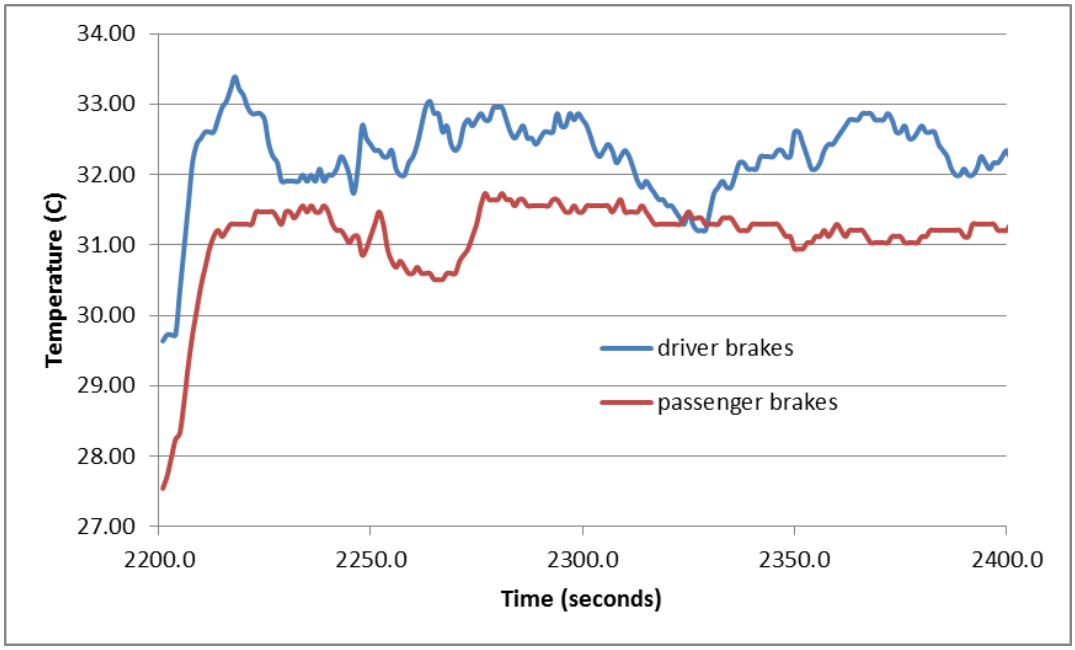

Figure 4.44: Temperature profile of the thermocouple in the vicinity of the brake pads after braking in Test 1 (160 km/hr and 0˚ yaw)

It is evident from Figure 4.43 that while the brakes are deployed the temperature measured decreased until the car reached a complete stop. This is because the cold air flow reached the thermocouple before the brake pads as illustrated in Figure 4.42. After braking, the temperature increased sharply and plateaued as shown in Figure 4.44. This was because after braking was complete and the car came to a stop the air flow from the wind tunnel was stopped. Furthermore the heat from the brake pads was then convected in all directions. Consequentially this made the thermocouple measure higher temperature. For that reason, only the "after braking" temperature profiles were covered as they present more information on brake pad heat generation than the temperature profile during braking.

In addition to Test 1, the brake proximity data of Tests 5 and 9 was analysed. The reason Tests 1, 5, and 9 were chosen to help in the brake analysis was because Test 1 was the reference at 0˚ yaw, Test 5 represented the most distinct representation of tests conducted in 7.5˚ yaw and Test 9 was the only test conducted in 0˚ yaw after the yaw configuration. Figure 4.45 and Figure 4.46 show the temperature captured by the thermocouple after braking in Tests 5 and 9 respectively.

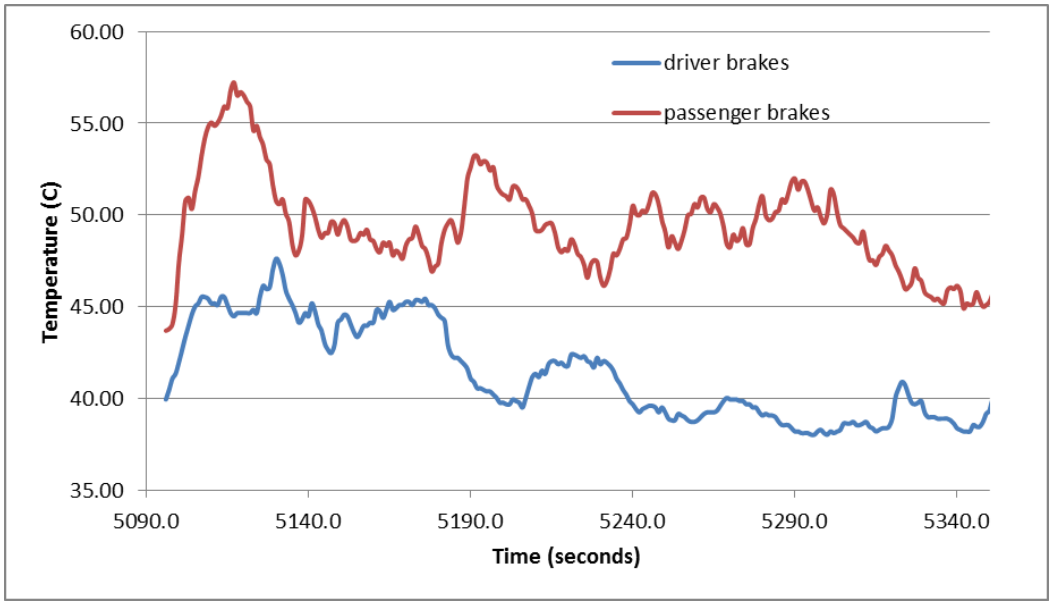

Figure 4.45: Temperature profile of the thermocouple in the vicinity of the brake pads after braking in Test 5 (160 km/hr and 7.5˚ yaw)

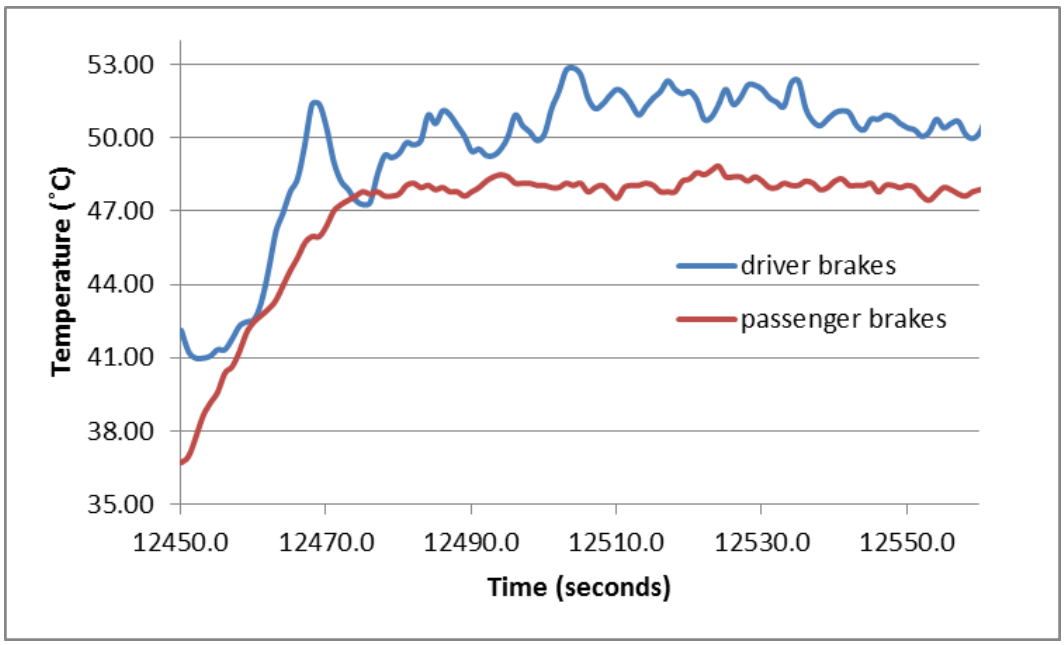

Figure 4.46: Temperature profile of the thermocouple in the vicinity of the brake pads after braking in Test 9 (160 km/hr and 0˚ yaw)

A clear difference is observed in Figure 4.45 (Test 5) when compared to Figure 4.44 (Test 1) and Figure 4.46 (Test 9). The passenger brakes temperature profile in Figure 4.45 is higher than the driver brakes temperature profile which is not the case in Figure 4.44 and Figure 4.46. This was attributed to the orientation of the car with the wind in Test 5 (Figure 4.45). Figure 4.47 shows a representation of the car's position with respect to the air flow direction.

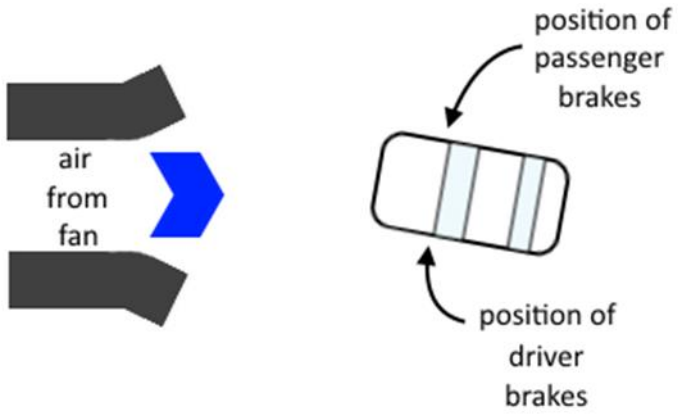

Figure 4.47: The test car's orientation in the CWT in a yawed orientation such as in Test 5

From Figure 4.47 when air was blown at an angle to the car, the right side of the car carried more load than the left. This made the right brakes apply more power to slow down the car.

However in Figure 4.44 and Figure 4.46 the brakes at the driver's side are higher in temperature than the passenger brakes. This was attributed to the unbalanced weight distribution due to the driver's weight. When comparing Figure 4.44 (Test 1) to Figure 4.46 (Test 9), it is

evident that the temperature range for the brake vicinity in Figure 4.46 is much higher than in Figure 4.44. This was attributed to the cold start and short running time of Test 1.

From the brake proximity temperature results that were obtained the driver brakes generated more heat than the passenger brakes in a 0˚ yaw configuration due to the driver's weight. When the car was yawed to 7.5˚ the passenger brakes generated more heat than the driver brakes due to the changed weight distribution. The lesson learned from this experiment is that there should have been a way to place the thermocouple downwind of the brakes as well in order to measure the temperature rise instantly during braking.

4.3.4: Summary

The upperbody analysis showed that when the car is in yaw the radiator performance is jeopardized, and that the tires generate more heat due to friction. It was also concluded that rear underbody diffusers reduce underbody cooling. The insight of the results obtained can help to develop devices that will enhance cooling capabilities in yaw to ensure that the car's components are working within their applicable temperature range. There were a number of lessons learned from the thermodynamic test. Adequate time should be given to stabilize the car's temperatures before a thermodynamic test is conducted. When studying

the brake performance of a car, the thermocouple should be placed downwind of the brake pads to measure instantaneous temperature rise.

Chapter 5 : Conclusion and Recommendations

This study filled a crucial void in automotive testing. This was achieved by developing, and testing an integrated aerodynamic and thermodynamic evaluation testing system. This thesis had three main objectives. The first was to design and assemble a force measuring system (FMS) for measuring incremental aerodynamic forces on cars as part of an integrated aerodynamic and thermodynamic testing system. This was achieved by using load cells, circuit boards, a data acquisition system, a voltage excitation source and an interface. The second objective was to develop a testing protocol for the integrated aerodynamic and thermodynamic testing in the CWT at UOIT. This was achieved by various test trials to obtain the most efficient testing protocol. The third objective was to calibrate the FMS and use it to measure incremental aerodynamic forces and apply the results to improve the aerodynamics of race cars. This was achieved experimentally and the effect of a number of aerodynamic devices on the aerodynamic forces were studied and analyzed. Later flow visualization and thermodynamic tests were conducted and analysed to demonstrate an integrated aerodynamic and thermodynamic test. Section 5.1 below summarizes the conclusions drawn from this study.

5.1: Summary of Results

5.1.1: The FMS

The design and assembly of the integrated FMS accomplished the following:

- Displayed repeatable as well as reliable results that compared favourably with theoretical results.
- Four cars were aerodynamically improved to attain the predetermined objectives.
- An integrated aerodynamic and thermodynamic testing protocol was developed for future testing utility.

5.1.2: Aerodynamic Force Improvement Tests

From the aerodynamic force improvement tests a number of noteworthy points were observed:

- Front and rear downforce have opposite effects on one another due to the chassis rigidity.
- The attachment of side front canards perpendicular to the flow decreased drag force, however when they are placed at a small positive angle to the flow they instead increased drag but significantly inflated front downforce.
- The rear wings increased drag force and rear downforce. Higher rear wings produced more drag force and rear downforce.

- The extended full width chin splitter significantly increased the front downforce and the drag force.
- It was also observed that a rear wedge (simulating an increases in a car's angle of attack) can have different effects depending on whether the car has an extended front splitter or not. With an extended front splitter a rear wedge elevated the front downforce however without an extended front splitter the rear downforce was elevated instead.
- The attachment of a gurney flap on the trailing edge of the high pressure rear wing side was found to increase both rear downforce and drag force.

5.1.3: Flow Visualization Test

The flow visualization test produced the following conclusions:

- Underbody flow visualization showed that local geometry had significant contribution to the flow direction, which was consistent with previous results (Khasow et al., 2015)
- The underbody flow visualization also showed that there was a spiral flow effect generated around the underbody exhaust pipe.
- The upperbody flow visualization revealed that when the car is in yaw, the exposed surface is less influenced by local geometry and more by the air flow direction

- It was demonstrated that hidden surfaces of the car caused flow separation and turbulent regions.

5.1.4: Temperature Analysis Test

The temperature analysis shows that:

- When the car was in yaw the radiator performance was jeopardized due the smaller inlet area of air through the grill.
- The tires generated more heat due to friction at yaw due to the projected side force.
- The underbody analysis showed uneven cooling rates in yaw.
- The rear underbody diffuser reduced underbody cooling. This was because it concealed surfaces which did not allow for adequate convection.
- The brake analysis showed that the brake performance is directly associated with static and dynamic weight distribution of the car.

5.2: Contribution

This thesis has developed a unique integrated aerodynamic and thermodynamic testing system as well as a testing protocol. This system has significantly increased the capabilities of the UOIT's CWT. It is the first of its kind that is capable of aerodynamic and thermodynamic testing on the same wind tunnel floor and turntable. The race car enthusiasts, especially amateur racers in Ontario, are excited about the facility. The recent YouTube posting of aerodynamic testing received

significantly more views than any UOIT video. The FMS designed in this study can be employed in other wind tunnels to achieve integrated testing.

In addition, the thesis is a demonstration of the combined effect of sets of common aerodynamic devices on cars. The results clearly show that the specific placement of any particular set of device on same car models has a significant effect on the aerodynamic forces. The implication is that aerodynamic improvement can only be reliably performed in a wind tunnel with the necessary force balances.

5.3: Recommendations for Future Work

The efficacy of the FMS developed in this thesis is satisfactory for the present tests, but a number of improvements can be made. The robustness of the cable wires connecting the load cells to the data acquisition system needs to be upgraded. Cable sizes and materials should be investigated to achieve robust characteristics without hampering signal quality. Robustness is imperative to avoid loose connections during high speed tests.

For absolute aerodynamic force values a revamp to UOIT's CWT is suggested to provide necessary testing conditions. As boundary layer growth is the biggest problem with AWTs, a boundary layer removal system such as a moving floor system is required. Also, a new FMS needs to be designed to be installed in a moving floor wind tunnel.

The frequency and sampling rate of the system needs to be adjusted to allow for more precise and steady readings. This should be done by studying the vibrations caused by the cars on the FMS and extracting the cars' vibration frequencies. The frequency and sampling rate of the system must then be manipulated to avoid detecting unwanted signal amplitudes.

In addition to car testing, rigs can be constructed to allow for a variety of different vehicles and vessels to be tested. Buses, trailer trucks, bicycles, boats, trains, yachts, and other transports have the potential to be tested and improved aerodynamically.

The aerodynamic effect of angled front canards on the aerodynamic forces needs to be investigated in detail. This is due to the sensitivity of the front canards' angle on the aerodynamic front downforce and drag force contribution. Experimental tests should be conducted to assess the performance of the front canards in different angle increments. The effect of geometry on the device's performance should also be studied.

Due to benefits of covering the lower portion of the radiator on the aerodynamics, a detailed radiator performance test must be conducted. This is to ensure that there is minimal thermodynamic downgrade effect when the car is aerodynamically enhanced. Inlet and outlet temperatures of covered and uncovered radiator situations should be

assessed and compared. Temperatures of engine components should also be determined to establish that there are no negative consequences from covering the lower radiator.

References

Barnard, R. H. (2009). *Road Vehicle Aerodynamic Design* (3rd ed.). MechAero Publishing.

Bucheim, R., Wilsden, D. J., Nishimura, Y., Schenkel, F. K., Mercker, E., Jousserandot, P., & Unger. (1983). Comparison tests between major European and North Amercian automotive wind tunnels. *SAE International*, *830301*, 17.

Carr, G. W. (1982). Correlation of Aerodynamic Force Measurements in MIRA and Other Automotive Wind Tunnels. *SAE International*, *820374*.

Chue, S. H. (1975). Pressure probes for fluid measurement. *Progress in Aerospace Sciences*, *16*(2), 147–223. doi:10.1016/0376-0421(75)90014-7

Duell, E., Kharazi, A., & Muller, S. (2010). The BMW AVZ Wind Tunnel Center. *SAE International*, (Paper#2010-01-0118).

Froling, T., & Juechter, T. (2005). 2006 Chevrolet Corvette C6 Z06 Aerodynamic Development. *SAE International*, *2005-01-19*, 6.

Gerhardt, H. J., Kramer, C., Zakowski, E., & Barth, H. (1986). The aerodynamic optimization of the ZAKSPEED formula 1 racing car. *Journal of Wind Engineering and Industrial Aerodynamics*, *22*(2-3), 291–297. doi:10.1016/0167-6105(86)90092-9

Guarro, M. D. (2010). *Wing Efficiency of Race Cars*. University of California, Santa Cruz.

Howell, J. (1981). Catastrophic Lift Forces of Racing Cars. *Journal of Wind Engineering and Industrial Aerodynamics*, *9*, 145–154.

Huber, S., Indinger, T., Adams, N., & Schuetz, T. (2014). Experimental and Numerical Study of Heat Transfer at the Underbody of a Production Car. *SAE International Journal of Commercial Vehicles*, *7*(1), 89–101. doi:10.4271/2014-01-0582

Hucho, I. (1993). Aerodynamics of Road Vehicles. *Annual Review of Fluid Mechanics*, *25*, 485–537. doi:10.1146/annurev.fluid.25.1.485

Hucho, W.-H. (1998). *Aerodynamics of Road Vehicles* (Fourth Edition). United States of America: Society of Automotive Engineers, Inc.

Katz, J. (2006). Aerodynamics of Race Cars. *Annual Review of Fluid Mechanics*, *38*, 27–63. doi:10.1146/annurev.fluid.38.050304.092016

Katz, J., & Garcia, D. (2002). Aerodynamic Effects of Indy Car Components. *SAE International*, *2002-01-33*, 9.

Khaled, M., Habchi, C., Harambat, F., Elmarakbi, A., & Peerhossaini, H. (2014). Leakage effects in car underhood aerothermal management: temperature and heat flux analysis. *Heat and Mass Transfer*, *50*(10), 1455–1464. doi:10.1007/s00231-014-1347-8

Khaled, M., Harambat, F., & Peerhossaini, H. (2009). A Quantitative Method for Assessment of Car Inclination Effects on Thermal Management of the Underhood Compartment. *Journal of Thermal Science and Engineering Applications*, *1*(1), 014501. doi:10.1115/1.3159477

Khasow, R., Best, S., Agelin-Chaab, M., Komar, J., & Elfstrom, G. (2015). Experimental investigation of underbody thermal and aerodynamic flow-field features. In *SAE World Congress and Exhibition*. Detroit, Michigan.

Kim, M., Lee, J., Kee, J., & Chang, J. (2001). Hyundai Full Scale Aero-acoustic Wind Tunnel. *SAE*.

Koitrand, S., & Rehnberg, S. (2013). *A Computational Investigation of Wheel and Underbody Flow Interaction*. Chalmers University of Technology.

Lien, M. S. (2010). *Aerodynamic Development and Construction of a Car for Participation in the Eco-Marathon Competition*. Norwegian University of Science and Technology.

Macmillan, F. A. (1957). *Experiments on pitot tubes in shear flow*. London.

Olson, M. E. (1976). *Aerodynamic Effects of Front End Design on Automobile Engine Cooling Systems*. doi:10.4271/760188

Potter, M. C., & Wiggert, D. C. (1997). *Mechanics of Fluids* (2nd ed.). New Jersey, US: Prentice-Hall, Inc.

Rathakrishnan, E. (2007). *Instrumentation, measurements and experiments in fluids*. Boca Raton: CRC Press.

Rehnberg, S., Börjesson, L., Svensson, R., & Rice, J. (2013). Race car aerodynamics - The design process of an aerodynamic package for the 2012 chalmers formula SAE car. In *SAE World Congress and Exhibition*. Detroit, Michigan.

Tavoularis, S. (2005). *Measurement in Fluid Mechanics*. New York: Cambridge University Press.

Tropea, C., Yarin, A. L., & Foss, J. F. (2007a). Aerodynamics. In *Springer Handbook of Experimental Fluid Mechanics* (pp. 1043–1080). doi:10.1007/978-3-540-30299-5

Tropea, C., Yarin, A. L., & Foss, J. F. (2007b). Flow Visualization. In *Springer Handbook of Experimental Fluid Mechanics* (pp. 857–870). doi:10.1016/0301-9322(82)90044-1

Van de Wijdeven, T., & Katz, J. (2013). Automotive Application of Vortex Generators in Ground Effect. *Journal of Fluids Engineering*, *136*(February 2014), 021102. doi:10.1115/1.4025917

Von Funck, W., Weinkauf, T., Theisel, H., & Seidel, H. P. (2008). Smoke surfaces: An interactive flow visualization technique inspired by real-world flow experiments. *IEEE Transactions on Visualization and Computer Graphics*, *14*(6), 1396–1403. doi:10.1109/TVCG.2008.163

Wang, J. J., Li, Y. C., & Choi, K. S. (2008). Gurney Flap-Lift Enhancement, Mechanisms and Applications. *Progress in Aerospace Sciences*, *44*, 22–47. doi:10.1016/j.paerosci.2007.10.001

Appendix I: Velocity and Pressure Measurements

I.1: Velocity Measurements

Velocity is a main parameter in fluid calculations and analysis. A number of direct and indirect methods exist for measuring velocity. Due to its importance modern velocity measurement devices are relatively sophisticated to produce accurate and precise measurements. A classical simple direct technique used to measure velocity directly is using vane anemometers. Vane anemometers are composed of a vane (propeller) attached on a rotating axis with a revolution counter installed on the edge of the device to count the number of revolutions the vane makes when a gaseous fluid is blown onto it. Finally, with proper calibration the revolutionary speed obtained is then converted to a velocity measurement unit. Some vane anemometers can be accurate up to ±1%. The source of error associated with vane anemometer is mostly friction between the vane and the rotating axis. Much more advanced technology exists in measuring velocity such as hot-wire anemometers, by measuring the heat transfer from a heated wire.

Velocity measurement in automotive applications is mostly associated with the cooling performance of the engine compartment. It is imperative to know the volume flow rate of air entering the compartment to avoid overheating at any road speed. The volume flow rate of air through a vane anemometer is simply calculated by multiplying the velocity of the air with the vane's cross-section area. Olson (1976)

measured the volumetric flow rate and its distribution through a 1974 Pinto and Mustang to determine the effect of the grill, bumper and air dam on the engine cooling performance in a wind tunnel. In order to find this out the flow rate of the total air entering the engine compartment and the radiator had to be determined with the grill, bumper and air dam on and off. The flow rate of the air entering the radiator was measured by a rake of vane anemometers. Multiple vane anemometers were installed on the rake each capable of measuring the magnitude and direction of the flow. The total flow rate through the engine compartment was estimated by means of smoke. Smoke from a wand was used to visualize the flow path into the cars' compartment. With cameras installed beside and above the front end of the car and a grid pattern on the floor and the wall of the test section, the cross-sectional area of the smoke entering the engine's compartment was estimated. Considering the velocity of the air from the tunnel, the total flow rate through the car was then calculated. The Mustang was tested at 0˚ yaw while the Pinto was tested at 0˚ and 20˚ yaw. The results revealed that the bumper and the grill hinder the flow of air through the radiator compartment. However, 50% - 65% of the air flow losses were recovered by installing the air dam. The difference of the air flow entering the engine compartment and the radiator were compensated by the addition of a fan and a shroud.

A commonly used indirect method of measuring velocity is by pressure measurement. There exists a relationship between velocity and pressure called the Bernoulli equation. The Bernoulli equation is by far the most used equation in fluid mechanics, however, its derivation is based on several simplifying assumptions (Potter et al., 1997). The equation was formulated under the assumption that the fluid is incompressible, and that there are no viscous effects caused by shear stresses and the velocity gradient of the boundary layer. The incompressibility assumption can be considered for operations below Mach 0.3, and although not considering the stresses caused by the viscous effects are justified they should be considered for flows over long distances or regions of high velocity gradients (Potter et al., 1997).

$$\frac{V^2}{2g} + \frac{p}{\gamma} = \text{constant} \tag{I.1}$$

The Bernoulli equation (shown above) is expressed along a fluid's streamline. Where V is the fluid's velocity at that point, p is pressure, h is elevation, ρ is the fluid's density, g is the gravity and $\gamma = \rho g$. When both sides of the equation are multiplied by γ the equation becomes:

$$p + \rho\frac{V^2}{2} = p_T \tag{I.2}$$

Where p_T is the total pressure (stagnation pressure), and p is the static pressure of the fluid. By measuring the static and total pressures,

the velocity is easily calculated from Equation (I.2). When pressure and velocity can be measured separately, the Bernoulli equation becomes helpful in calculating the percent variance in the velocity measured from both devices. As an example, in Olson's experiment after the vane anemometers were individually calibrated the velocity variation between that measured by the vane anemometer and a local dynamic pressure probe was ±1.5% (Olson, 1976). Pressure measurement however has a number of downsides and limitations some of which are explained in Section I.2.

The velocity was measured by vain anemometers supplied by Emprise model ANEM-300. Three vain anemometers were used in this test: one to measure the velocity of the air through the brake cooling duct, and the other two for the air velocity out of the two transmission cooling ducts. The anemometers were connected to a 4-channel universal counter capable of reading data in different modes; frequency, period duration, and event counting. A calibration data is available for converting the data to speed. The rated uncertainty for the anemometers is ±0.5%.

The velocities of three locations were obtained. The velocity of the air entering the airbox was not measured because in automotive applications only the differential pressure in the airbox characterises its performance. The velocity results measured are shown in Table I.1.

Table I.1: Velocities of different duct positions at different yaw angles at 160 km/hr

	Velocity m/s	
Location	0˚ yaw	7.5˚ yaw
Brake cooling duct	0.42	0.80
Differential cooling duct	1.27	0.64
Rear tire pressure duct	1.06	0.90

It is evident from Table I.1 that the velocities measured at 0˚ yaw are higher than those measured at 7.5˚ yaw except for the brake cooling duct. The brake cooling duct recorded a higher velocity in yaw because it was attached at an angle to the flow, therefore in yaw its orientation was aligned with the flow which resulted in a higher measured velocity.

I.2: Pressure Measurements

In automotive aerodynamic testing, pressure measurement is predominantly used to improve pressure distribution due to pressure drag contributing most of the car's drag (Barnard, 2009). However as previously stated pressure measurement can also be used to determine other parameters such as velocity. In this section an intrusive pressure measurement technique, Pitot tubes, are discussed as they are the most reliable and cost effective method despite their undesirable attributes

(deforms body of attachment and distorts the desirable pressure field) (Tavoularis, 2005). Pitot tubes are the most popular method of measuring total local pressure, however they come with a number of limitations (Rathakrishnan, 2007). Most importantly there is an inaccuracy associated with the Pitot's position misalignment. Tavoularis (2005) mentions that although the sensitivity of Pitot tubes are not as high as Pitot static tubes once the yaw angle exceeds a critical angle the pressure will decrease rapidly. Chue (1975) defined the critical angle as the angle of yaw at which the total pressure difference becomes 1% of the dynamic pressure value. Figure I.1 shows the effect of the yaw angle on the circular cross-sectional Pitot tube. The critical angle for the circular cross-sectional tube is 11˚ (Chue, 1975).

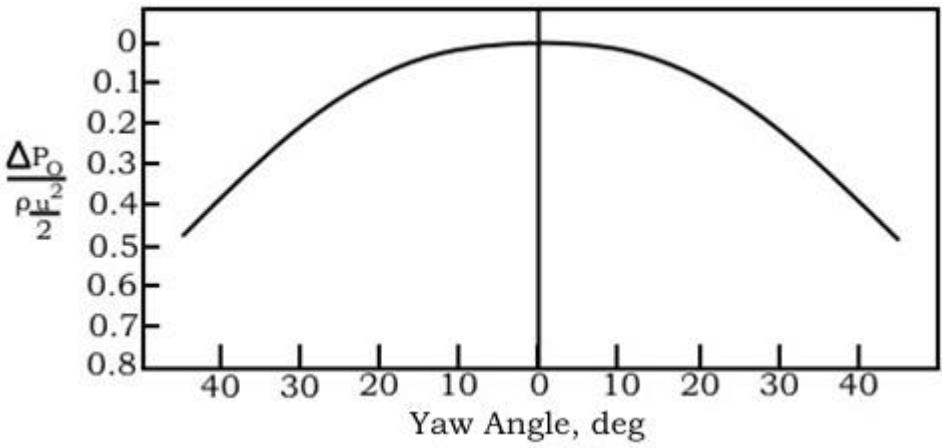

Figure I.1: The effect of the yaw angle on the pressure of a circular Pitot tube (Chue, 1975)

Another limitation of the Pitot tube is the wall proximity effect (Tavoularis, 2005). Both Tavoularis and Chue agree that the presence of the Pitot close to the wall, where a fluid boundary layer exists, blocks the flow in its vicinity which in return deflects the streamlines away from the wall. Therefore this deflection causes the probe to indicate a greater total pressure than that existing at the same location in the absence of the probe. Macmillan (1957) stated that particularly for circular tubes the wall proximity effect would be prevented if kept at a $2D_o$ distance from the wall where D_o is the outer diameter of the tube. Tavoularis (2005) mentioned that the velocity correction of a circular tube in contact with the wall is only about 1.5%.

As Pitot tubes are essentially used to measure pressure they are most commonly used to measure velocity by Bernoulli's equation. Guarro (2010) utilized a Pitot tube to measure the speed of the air in a small-scale wind tunnel to aerodynamically improve a racing car's rear wing. Guarro connected the Pitot tube to a flow meter to compare the total pressure and the static pressure and display the differential pressure head. The velocity of the air in the wind tunnel is then produced from Bernoulli's equation. Similarly, Lien (2010) measured the velocity of the air flow in a large-size wind tunnel for the aerodynamic development of a hybrid racing car, however the velocity was measured by a computer. Lien placed a single Pitot static tube upstream of the car in the wind tunnel, the Pitot system was connected to a pressure

transducer which detects the differential pressure produced and outputs it as a voltage signal instead. The air velocity is then correlated from the voltage signal by previous calibration.

Howell (1981) on the other hand utilized a Pitot system to obtain a pressure field. The pressure field was measured downstream of a racing car in a small-scale wind tunnel by a rake Pitot system which is composed of Pitot tubes stacked in series. By plotting the pressures obtained from the Pitot tubes with respect to their location, a pressure field was produced.

A digital differential manometer, model HT-1890, was used to measure the pressure in various areas including the inlet and outlet of the airbox, the transmission cooling ducts, and the brake cooling ducts. The manometer has two orifices for measuring differential pressure therefore for the airbox measurement the differential was measured instead of the inlet and outlet separately by long hoses. When measuring the transmission cooling ducts and the brake cooling ducts, only one hose was used while the other was blocked to measure absolute pressure instead. As the pressure is displayed real-time a GoPro camera was situated facing the manometer in the car cabin. The camera's display was being observed from inside the control room of the CWT. The error associated with the differential manometer is ±1%.

Pressure was measured at four locations. The measured pressure results are shown in Table I.2.

Table I.2: Pressure results at selected locations for 0˚ and 7.5˚ yaw at 160 km/hr

		Pressure (kPa)	
Test	Measurements	0˚ yaw	7.5˚ yaw
1	Brake cooling duct	0.18	0.02
2	Differential cooling duct	0.21	0.28
3	Rear tire pressure duct	0.19	0.30
4	Differential Pressure of airbox	0.43	0.34

From Table I.2 only measurements obtained from the rear tire pressure duct and the differential cooling duct at 7.5˚ yaw show relatively higher pressures than those obtained at 0˚ yaw.

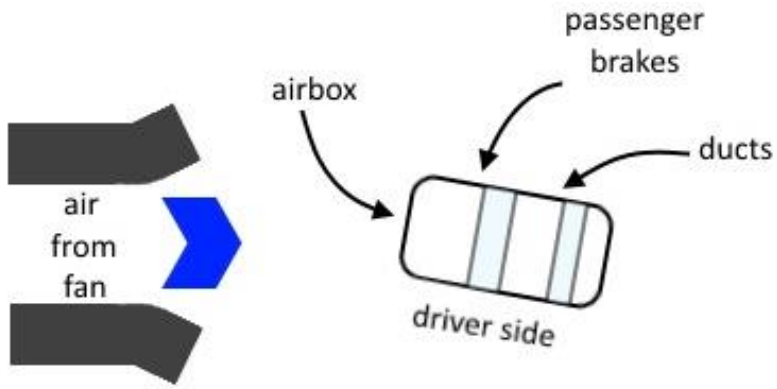

Figure I.2: Diagram illustrating the position of the car with respect to the nozzle in yaw

The remaining measured pressures at 7.5˚ yaw show relatively lower pressures than their corresponding 0˚ yaw values. The low

differential pressure measured in the airbox in yaw was attributed to the reduced air flow through the front grill. This was because in yaw the frontal area of the front grill is reduced. The low pressure measured at the brake cooling duct was attributed to alignment error. This is because the pressure hose was located very close to the front of the car where air is more unidirectional. At that position a very small alignment error of the pressure hose will produce a significant change. The reason the measured low pressure was attributed to alignment error is because from Figure I.3 it is evident that a yaw of 7.5˚ should not have such a significant effect on the pressure.

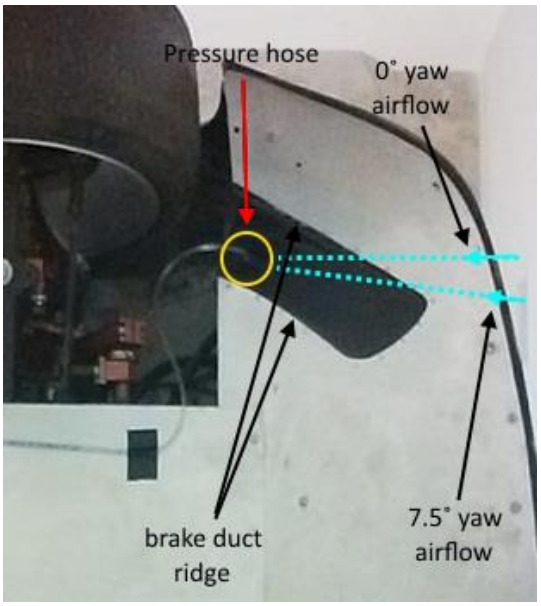

Figure I.3: Close-up of the pressure hose on the brake cooling duct with respect to the different airflow directions

Appendix II: Aerodynamic Devices

Figure II.1: The front canards used for 944 Case 1 (left) and 944 Case 2 (right)

Figure II.2: The small rear wing used for 944 Case 1

Figure II.3: The high rear wing used for 944 Case 1

Figure II.4: 944 Case 1 with a full width front splitter, a lower radiator cover, and tape covering the hood slots

Figure II.5: 944 Case 1 with modified full width front splitter extension

Figure II.6: 944 Case 2 showing the built-in rear wing extending out from the rear hatch

Figure II.7: A 1.5 cm rear wedge on 944 Case 2

Figure II.8: The high rear wing on Cayman Case 1

Figure II.9: The front of Cayman Case 1 showing the front splitter

Figure II.10: The rear of Cayman Case 2 showing the small rear wing

Appendix III: Radiator Performance Study

Test 10 was conducted to study the effect of covering the lower portion of the radiator on the radiator's performance. This was done because it was observed that covering the lower portion of the radiator increased front downforce and decreased total drag of the car (discussed in Section 4.1.2). The radiator performance was studied by placing a thermocouple upwind and downwind of the radiator and comparing the results with those when the radiator was not covered. The inlet and outlet temperature results on tests conducted in 0˚ yaw only (Tests 1 to 4, 9 and 10) are shown in Table III.1 below.

Table III.1: Inlet and outlet radiator temperatures for thermodynamic Tests 1-4, 9, and 10 with covered lower radiator

	Radiator inlet (˚C)	Radiator outlet (˚C)	Difference (˚C)
Test 1	26.8	45.2	18.4
Test 2	27.2	45.8	18.6
Test 3	26.9	43.1	16.2
Test 4	28.5	47.3	18.8
Test 9	26.4	50	23.6
Test 10*	25.3	42	16.7

Test 10* the radiator is covered

The temperatures recorded in the table were the final temperatures of every thermodynamic test. This is done to ensure that the test has reached its longest time towards a steady state condition. The radiator inlet temperatures of all the tests were between 25˚C and 29˚C which is consistent with the controlled ambient temperature of the wind tunnel. As mentioned in section 4.3, thermodynamic Tests 1 to 5 did not reach steady state conditions as their duration was short, on the other hand, Test 6 to 9 did reach steady state conditions. Only Tests 1 to 4 and 9 are mentioned as they were the only tests out of the 9 tests conducted in 0˚ yaw. When comparing the temperature change of the radiators for the short tests (Tests 1 to 4), Test 3 has the smallest temperature change. This is attributed to Test 3 having the shortest car run time of the first four tests which can be seen from Figure 4.34 and Figure 4.37. A shorter run time prevents the radiator from working effectively, therefore producing a lower temperature change. Comparing the only long test conducted at 0˚ yaw (Test 9) to the short tests, Test 9 recorded the highest temperature change because of the effective radiator performance. Test 10 was conducted on another day. This meant that the condition of the car was similar to that of Test 1. The duration of Test 10 however was not timed, therefore the effect of taping the lower radiator on the radiator performance is inconclusive because the running time of Test 10 was not recorded to determine if steady state was reached or not.

Appendix IV: Load cells placement

Preliminary tests

In the preliminary tests, two types of load cells were used; the TR3D-A-1K and the TR3D-A-5K. The difference between the two models was their loading limits; where the TR3D-A-1K model has a loading limit of 4448 N, while the TR3D-A-5K model has a loading limit of 22241 N. The reason two different types of models were used is because the 5K model was already available prior to purchasing more load cells but the supplier could not fill the purchase order for all the 12 sensors on time. However, in the final test, only the TR3D-A-1K was used. The 5K model is physically identical (Figure 3.2) to the 1K model which facilitated in the testing process until the 1K load cells arrived. The 5K model had the same error range as the 1K model shown in Table 3.1.

Load cell placement

The load cells were experimented in a variety of different placements. This was to investigate the load cell placement with the minimum error. Since three load cells were assigned to each FMS box, a triangular arrangement (a load cell on each corner of the triangle) was chosen as the best layout for the load cells for better balance. The best placement of each load cell and their distances apart were required to be known. Two triangle types were experimented with; equilateral and isosceles triangles. The triangles were experimented with different dimensions as well. Since the dimensions of the load cells were

contingent on the dimension of the tire patch, a tire patch was sketched and sawed out of a 1.5 cm thick wooden plank shown in Figure IV.1.

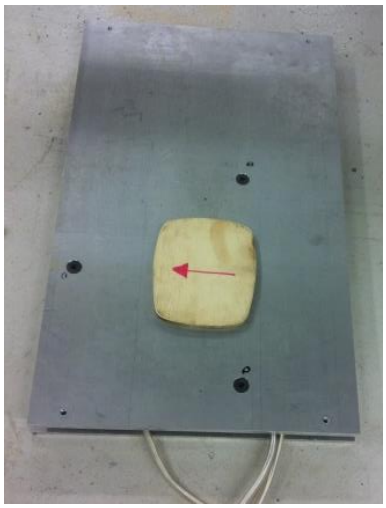

Figure IV.1: A sawed off wooden piece resembling the tire patch of the test car on the FMS box to simulate realistic weight distribution

Loads were applied on the wooden patch to obtain incremental measurements for the *z*-axis. Loads were also suspended from the FMS box to obtain incremental measurement for the *x*-axis and *y*-axis as shown in Figure IV.2. Incremental measurements were obtained by making note of the reading change when loads were applied and removed and not the absolute measurement reading.

Figure IV.2: Loads suspended from the FMS box to obtain measurements on the *x*-axis

The implications from the experiment results showed that although there were insignificant differences between the triangle arrangements, an equilateral triangle was chosen because it distributed the load equally between all the load cells. Various equilateral triangle dimensions were tested as shown in Figure IV.3.

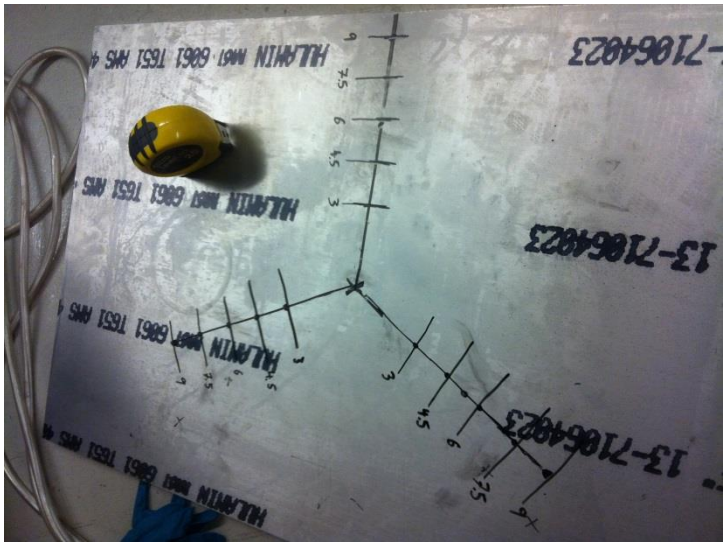

Figure IV.3: Various equilateral triangles experimented with on the FMS box

The experiment results revealed that a triangle with 40 cm sides was ideal because it showed minimal incremental error. This was because the close displacement between the tires and the sides of the triangle prevented any deflection from occurring which is a conduit to discrepancies.

Appendix V: Hysteresis

The hysteresis error shows the effect of load on measurement readings at zero load conditions. After a load was applied on the FMS and removed, the output stabilized value of the FMS (at zero load) is considered the hysteresis value. The percentage of this value to the load applied is the hysteresis error. The hysteresis error has minimal effect on the results obtained in this study as the FMS was always reset to zero before every test run. In the present study, after the aerodynamic test of 944 Case 2 was completed, the output value of the FMS was recorded having ensured that the output was stabilized. The values recorded were found as a percentage of the maximum load reached shown in Table V.1. The durations in brackets next to the errors show the length of time the maximum load was applied. From the results below the range of the hysteresis error is below 1.25%. Although this error does not affect the improvement test readings (because of the zero reset function) it was calculated to add to the FMS' specifications.

Table V.1: Hysteresis errors for 944 Case 2

	Hysteresis error		
	Front downforce	Rear downforce	Total drag
944 Case 2	1.03% (1.7 min)	1.18% (1.7 min)	1.22% (1.7 min)